VILNIUS UNIVERSITY
LITHUANIAN UNIVERSITY OF EDUCATIONAL SCIENCES

PAVEL RYNKUN

DEVELOPMENT OF BIORTHOGONAL ORBITAL METHOD AND ITS APPLICATION IN ATOMIC THEORY

Doctoral dissertation
Physical Sciences, Physics (02 P)

Vilnius, 2014

Doctoral dissertation was completed during 2009–2013 at Lithuanian University of Educational Sciences.

Scientific supervisor:

prof. habil. dr. Gediminas Gaigalas (Vilnius University, Physical sciences, Physics – 02 P).

Consultant:

prof. dr. Per Jönsson (Malmö University, Malmö, Sweden, Physical sciences, Physics – 02 P).

VILNIAUS UNIVERSITETAS
LIETUVOS EDUKOLOGIJOS UNIVERSITETAS

PAVEL RYNKUN

BIORTOGONALIŲ ORBITALIŲ METODO PLĖTOJIMAS IR TAIKYMAS ATOMO TEORIJOJE

Daktaro disertacija
Fiziniai mokslai, fizika (02 P)

Vilnius, 2014

Daktaro disertacija rengta 2009–2013 metais Lietuvos edukologijos universitete.

Mokslinis vadovas:

prof. habil. dr. Gediminas Gaigalas (Vilniaus universitetas, fiziniai mokslai, fizika – 02 P).

Konsultantas:

prof. dr. Per Jönsson (Malmės universitetas, Malmė, Švedija, fiziniai mokslai, fizika – 02 P).

Table of Contents

Approbation

Scientific papers related to the topic of this thesis

A1 **P. Rynkun**, P. Jönsson, G. Gaigalas, and C. Froese Fischer, *Energies and E1, M1, E2, M2 transition rates for states of the* $2s^2 2p$, $2s2p^2$, *and* $2p^3$ *configurations in boron-like ions between N III and Zn XXVI*, At. Data and Nucl. Data Tables **98**, 481 (2012).

A2 P. Jönsson, **P. Rynkun**, and G. Gaigalas, *Energies, E1, M1, and E2 transition rates, hyperfine structures, and Landé* g_J *factors for states of the* $2s^2 2p^2$, $2s2p^3$, *and* $2p^4$ *configurations in carbon-like ions between F IV and Ni XXIII*, At. Data and Nucl. Data Tables **97**, 648 (2011).

A3 **P. Rynkun**, P. Jönsson, G. Gaigalas, and C. Froese Fischer, *Energies and E1, M1, E2, M2 transition rates for states of the* $2s^2 2p^3$, $2s2p^4$, *and* $2p^5$ *configurations in nitrogen-like ions between F III and Kr XXX*, At. Data and Nucl. Data Tables **100**, 315 (2014).

A4 **P. Rynkun**, P. Jönsson, G. Gaigalas, and C. Froese Fischer, *Energies and E1, M1, E2, and M2 transition rates for states of the* $2s^2 2p^4$, $2s2p^5$, *and* $2p^6$ *configurations in oxygen-like ions between F II and Kr XXIX*, A&A **557**, A136 (2013).

A5 G. Gaigalas, Z. Rudzikas, E. Gaidamauskas, **P. Rynkun**, and A. Alkauskas, *Pecularities of spectroscopic properties of* W^{24+}, Phys. Rev. A **82**, 014502 (2010).

A6 S. Verdebout, **P. Rynkun**, P. Jönsson, G. Gaigalas, C. Froese Fischer, and M. Godefroid, *A partitioned correlation function interaction approach for describing electron correlation in atoms*, J. Phys. B: At. Mol. Opt. Phys. **46**, 085003 (2013).

A7 C. Froese Fischer, S. Verdebout, M. Godefroid, **P. Rynkun**, P. Jönsson, and G. Gaigalas, *Doublet-quartet energy separation in boron: A partitioned-correlation-function-interaction method*, Phys. Rev. A **88**, 062506 (2013).

A8 S. Verdebout, **P. Rynkun**, P. Jönsson, G. Gaigalas, C. Froese Fischer, and M. Godefroid, *Interaction of variational localised correlation functions for atomic properties of Be I*, J. Phys.: Conf. Ser. **388**, 152006 (2012).

Other scientific papers

A9 E. Gaidamauskas, C. Nazé, **P. Rynkun**, G. Gaigalas, P. Jönsson, and M. Godefroid, *Tensorial form and matrix elements of the relativistic nuclear recoil operator*, J. Phys. B: At. Mol. Opt. Phys. **44**, 175003 (2011).

A10 G. Gaigalas, Z. Rudzikas, **P. Rynkun**, and A. Alkauskas, *Dependence of the probabilities of the electric-multipole electron transitions in* W^{24+} *on multipolarity*, Phys. Rev. A **83**, 032509 (2011).

A11 G. Gaigalas, **P. Rynkun**, A. Alkauskas, and Z. R. Rudzikas, *The energy levels and radiative transition probabilities for electric quadrupole and magnetic dipole transitions among the levels of the ground configuration,* $[Kr]4d^{10}4f^4$*, of* W^{24+}, At. Data and Nucl. Data Tables **98**, 391 (2012).

Conference presentations

C1 G. Gaigalas, Z. Rudzikas, E. Gaidamauskas, **P. Rynkun**, and A. Alkauskas, *Lowest 977 energy levels, E1 transition probabilities and lifetimes for* W^{24+}, International Conference on Atomic and Molecular Data and Their Applications (ICAMDATA 7), Book of Abstracts, 21 – 24 September 2010, Vilnius, Lithuania. ISBN 9789955335993 p. 99.

C2 S. Verdebout, M. R. Godefroid, **P. Rynkun**, P. Jönsson, G. Gaigalas, and C. Froese Fischer, *Interaction of variational localized correlation functions for atomic properties*, 43rd EGAS (European group for atomic systems) Europhysics conference abstracts, June 28 – July 2, 2011, Fribourg, Switzerland. ISBN 2-914771-67-3 p. 155.

C3 **P. Rynkun**, S. Verdebout, P. Jönsson, G. Gaigalas, C. Froese Fischer, and M. Godefroid, *On the energy difference between* $1s^22s^22p\ ^2P^o$ *and* $1s^22s2p^2\ ^4P$ *terms in Boron*, 44th EGAS (European group on atomic systems) Conference, Europhysics conference abstracts, July 9 – 13, 2012, Gothenburg, Sweden. ISBN 2-914771-75-4 p. 122.

C4 S. Verdebout, **P. Rynkun**, P. Jönsson, G. Gaigalas, C. Froese Fischer, and M. Godefroid, *A Partitioned Correlation Function approach for atomic properties* 44th EGAS (European group on atomic systems) Conference, Europhysics conference abstracts, July 9 – 13, 2012, Gothenburg, Sweden. ISBN 2-914771-75-4 p. 144.

Acknowledgments

I would like to express my special gratitude for my scientific supervisor prof. habil. dr. Gediminas Gaigalas for the excellent guidance, support, valuable comments and discussions during the study.

I would like to express my special thanks for my consultant prof. dr. Per Jönsson for the help, valuable discussions and tips.

I would also like to thank Charlotte Froese Fischer, Michel Godefroid and Simon Verdebout for the useful and interesting exchanges and collaborations that we had all along this PhD study. Thank for them for the common projects in the research.

I would like to thank to my colleagues PhD students Andrius Alkauskas and Laima Radžiūtė for the help, discussions and technical questions.

List of the abbreviations

AS active set
ASF atomic state function
ATSP atomic-structure package
B Breit
BP Breit-Pauli
BPRM Breit-Pauli R-matrix
CAS complete active space
CC core-core
CF correlation function
CI configuration interaction
CITRO configuration interaction on the basis of transformed radial orbitals
CSF configuration state function
CUD closed under de-excitation
CV core-valence
DPCFI deconstrained partitioned correlation functions interaction
E1 electric dipole
E2 electric quadrupole
EBIT electron beam ion trap
EOL extended optimal level
FAC flexible atomic code
GRASP general-purpose relativistic atomic structure package
HF Hartree-Fock
HFR Hartree-Fock-Ralativistic
M1 magnetic dipole
M2 magnetic quadrupole
MBPT many-body perturbation theory
MCDHF multiconfiguration Dirac-Hartree-Fock
MCHF multiconfiguration Hartree-Fock
MCHF-BP multiconfiguration Hartree-Fock Breit-Pauli
MR multireference
MRMP multireference Møller-Plesset perturbation theory

MRRCI multireference relativistic configuration-interaction

NIST National Institute of Standards and Technology

QED quantum electrodynamic

PCF partitioned correlation function

PCFI partitioned correlation functions interaction

PT perturbation theory

RAS restricted active space

RCI relativistic configuration interaction

SCF self-consistent field

SD single double

SDT single double triple

SE semi-empirical

SR single reference

SS superstructure

VV valence-valence

Chapter 1

Introduction

Atomic data are widely used in many diverse fields of science and technology, such as atomic spectroscopy, astrophysics, plasmas physics, fusion energy [1]. Atomic structure calculations not only assist the spectroscopist in the analysis of complex spectra by providing some reliable term positions, level designations, synthesis spectra, helping in the assignment of the observed lines, but also contribute to the understanding of the underlying physical processes [2].

Tungsten (W) is considered as a plasma wall material in the development of future tokamaks. Therefore, the data on spectral properties of its various ions are of great importance. Ions, having simple electronic configurations of open shells, are studied widely both experimentally and theoretically, but this is not the case for ions, having open f-shell, due to the large number of the energy levels.

Accurate description of electron correlation remains a major challenge in atomic structure calculations. To meet this challenge a number of different methods have been developed such as many-body perturbation theory (MBPT) [3, 4], combinations of configuration interaction and many-body perturbation (CI+MBPT) [5, 6, 7], and coupled cluster (CC) [8, 9, 10] theories. Different kinds of variational methods have also been used, and one may specially note Hylleraas-type calculations, that explicitly include the interelectron distance r_{12} in the construction of the wave function [11, 12, 13, 14]. In quantum chemistry, variational complete active space self-consistent field (CASSCF) methods are quite successful for describing small and medium-size molecules, but are not sufficient when dynamical correlation must be included [15]. The latter are treated through second-order perturbation theory using a single or multireference state as the zero-order approximation. Combined variational multireference and second order Möller-Plesset perturbation calculations have also been applied very successfully by Ishikawa and co-workers [16, 17] to obtain accurate transition energies for a number of atomic systems.

Based on a fast transformation technique, originally proposed by Malmqvist and collaborators [18, 19], it is shown that it is possible to relax the orthonormality restriction on the orbital basis and use several mutually non-orthogonal orbital basis sets that are better adapted to the short range nature of the dynamical correlation. The developed Partitioned Correlation Function Interaction (PCFI) method is described and is shown its advantages compared with other methods.

The main goals of the study:

- to develop the biorthogonal orbital method for calculation of energies and other important atomic data;
- to obtain more accurate atomic data (energy levels, transition rates, lifetimes) using *ab initio* method.

The main tasks of the study:

1. to perform large-scale calculations in orthogonal orbitals basis for B-, C-, N-, and O-isoelectronic sequences;
2. to study energy spectra and electricdipole transition rates of W^{24+};
3. to modify the expressions of the matrix elements of the Breit-Pauli hamiltonian for the biorthogonal orbital method;
4. to apply the developed biorthogonal orbital method for the calculation of energy levels, isotope shifts, hyperfine structure constants:
    - to perform calculations of hyperfine structure constants and isotope shift for lithium;
    - to perform calculations for the transition energy between the $^2P^o$ and ^4P terms of neutral boron;
5. to evaluate obtained results comparing with other theoretical calculations and experiment.

Statements presented for defence:

1. Multiconfiguration Dirac-Hartree-Fock and relativistic configuration interaction methods, realized in newest General-purpose Relativistic Atomic

Structure package, allowed us get lifetimes with experimental error bars and energy levels, which differ from the experimental results less than 0.1% for light ions.

2. The results of tungsten W^{24+} ion obtained in the study indicate that using to the spin-angular integration method based on the second quantization in coupled tensorial form we can more efficiently study most complex electronic configurations of atoms and ions, and obtain the more accurate data on energy spectra, transition probabilities, lifetimes of excited levels and the other spectroscopic parameters.

3. To achieve high accuracy results for specific mass shift parameters and hyperfine structure constants using the PCFI approach based on the biorthogonal orbital method it is necessary to use PCFI approach with full deconstraining of the CSFs space.

4. The PCFI approach, developed in this study which is based on the biorthogonal orbital method, has the benefits compared with the traditional multiconfiguration approach: i) it converges faster; ii) it allows us to get the more accurate results for total energies, transition energies, specific mass shift parameters and hyperfine structure constants.

Thesis outline

The doctoral dissertation consists of six chapters. Chapter 1 introduces goals, main tasks of sutdy and statements presented for defence. Chapter 2 is designed to describe theoretical methods that were used in the thesis. There is also an account of the newly developed PCFI method based on biorthogonal transformations and the modifications in spin-angular part that were needed.

The other three chapters are devoted to presenting the results obtained in the dissertation. Each of them has a scientific review of the research and importance. Also the results obtained in this work are compared with other authors' theoretical and experimental data. Chapter 3 chapter presents the calculation of spectroscopic data (such as energy levels, transition probabilities, lifetimes) of boron, carbon, nitrogen and oxygen isoelectronic sequences. Such data are needed in astrophysics, for the examination of the phenomena occurring in the plasma. Chapter 4 presents the results of the W^{24+} calculations: energy spectra

structure, the strongest electric dipole transitions, the lifetimes. Tungsten is used as a wall material for existing and planned constructions of fusion reactors. It is therefore necessary for the tungsten ion energy spectra and other characteristics, in order to control the tungsten ions in fusion plasma. In Chapter 5 applications of PCFI approach are presented for lithium and boron. For neutral boron the $^2P^o$ and ^4P transition energy was calculated using multiconfiguration Hartree-Fock and PCFI methods. Chapter 6 presents the conclusions of the study.

Chapter 2

Methodology

2.1 Multiconfiguration Hartree-Fock approach

In the multiconfiguration Hartree-Fock (MCHF) method, the wave function is approximated by a linear combination of orthonormal configuration state functions so that

$$\Psi(\gamma\, LS^{\pi}) = \sum_{i=1}^{M} c_i\, \Phi_i(\gamma_i\, LS^{\pi})\,, \tag{2.1.1}$$

where

$$\sum_{i=1}^{M} c_i^2 = 1\,. \tag{2.1.2}$$

A configuration state function (CSF), $\Phi_i(\gamma_i\, LS^{\pi})$, in (2.1.1) has a given parity (π) and LS symmetry. The non-relativistic Hamiltonian for an N-electron system is given by

$$H = \sum_{i=1}^{N}\left[-\frac{1}{2}\nabla_i^2 - \frac{Z}{r_i}\right] + \sum_{i<j}^{N}\frac{1}{r_{ij}}\,. \tag{2.1.3}$$

The CSFs are built from a common basis of one-electron spin-orbitals

$$\phi(nlm_l m_s) = \frac{1}{r}P(nl\,;r)Y_{lm_l}(\theta,\varphi)\chi_{m_s}, \tag{2.1.4}$$

where the radial functions $P(nl\,;r)$ are to be determined on a grid [20]. For the approximate wave function (2.1.1), the integro-differential MCHF equations have the form

$$\left\{\frac{d^2}{dr^2} + \frac{2}{r}\left[Z - Y(nl\,;r)\right] - \frac{l(l+1)}{r^2} - \varepsilon_{nl,nl}\right\}P(nl\,;r) = \frac{2}{r}X(nl\,;r) + \sum_{n'\neq n}\varepsilon_{nl,n'l}P(n'l\,;r) \tag{2.1.5}$$

for the unknown radial functions [20]. The equations are coupled to each other through the direct Y and exchange X potentials and the Lagrange multipliers $\varepsilon_{nl,n'l}$. The Lagrange multipliers force the radial orbitals to be orthonormal within the same l subspace. Under these conditions the configuration state functions are orthonormal

$$\langle \Phi_i | \Phi_j \rangle = \delta_{i,j}. \tag{2.1.6}$$

The mixing coefficients appearing in the expansion over CSFs also enter in the form of the potentials and are determined by solving the configuration interaction (CI) problem

$$\mathbf{Hc} = E\ \mathbf{c}, \tag{2.1.7}$$

with $H_{ij} = \langle \Phi_i | H | \Phi_j \rangle$ being the Hamiltonian matrix and $\mathbf{c} = (c_1, c_2, \ldots, c_M)^t$ the column vector of mixing coefficients. For a given set of mixing coefficients, the equations (2.1.5) are solved by the self-consistent field (SCF) procedure. The SCF and CI problems are solved, one after the other, until convergence of both the radial functions and the selected CI-eigenvector is achieved.

2.2 The Breit-Pauli approximation

In the Breit-Pauli approximation [20], the Hamiltonian is extended to include relativistic corrections up to a relative order of $(\alpha Z)^2$. The Breit-Pauli Hamiltonian can be written

$$H_{BP} = H_{NR} + H_{RS} + H_{FS}, \tag{2.2.1}$$

where H_{NR} is the ordinary non-relativistic many-electron Hamiltonian (2.1.3). The relativistic shift operator H_{RS} commutes with L and S and can be written

$$H_{RS} = H_{MC} + H_{D1} + H_{D2} + H_{OO} + H_{SSC}, \tag{2.2.2}$$

where H_{MC} is the mass correction term

$$H_{MC} = -\frac{\alpha^2}{8} \sum_{i=1}^{N} (\nabla_i^2)^\dagger \nabla_i^2 \tag{2.2.3}$$

and H_{D1} and H_{D2} are the one- and two-body Darwin terms

$$H_{D1} = -\frac{Z\alpha^2}{8} \sum_{i=1}^{N} \nabla_i^2 \left(\frac{1}{r_i} \right), \tag{2.2.4}$$

$$H_{D2} = \frac{\alpha^2}{4} \sum_{i<j}^{N} \nabla_i^2 \left(\frac{1}{r_{ij}} \right). \tag{2.2.5}$$

H_{SSC} is the spin-spin contact term

$$H_{SSC} = -\frac{8\pi\alpha^2}{3} \sum_{i<j}^{N} (\boldsymbol{s}_i \cdot \boldsymbol{s}_j) \delta(\boldsymbol{r}_i \cdot \boldsymbol{r}_j) \tag{2.2.6}$$

and finally H_{OO} is the orbit-orbit term

$$H_{OO} = -\frac{\alpha^2}{2} \sum_{i<j}^{N} \left[\frac{\boldsymbol{p}_i \cdot \boldsymbol{p}_j}{r_{ij}} + \frac{\boldsymbol{r}_{ij} (\boldsymbol{r}_{ij} \cdot \boldsymbol{p}_i) \boldsymbol{p}_j}{r_{ij}^3} \right] \tag{2.2.7}$$

The fine-structure operator H_{FS} describes interactions between the spin and orbital angular momenta of the electrons, and does not commute with L and S but only with the total angular momentum $J = L + S$. The fine-structure operator consists of three terms

$$H_{FS} = H_{SO} + H_{SOO} + H_{SS}. \tag{2.2.8}$$

Here H_{SO} is the nuclear spin-orbit term

$$H_{SO} = -\frac{Z\alpha^2}{2} \sum_{i=1}^{N} \frac{1}{r_i^3} \boldsymbol{l}_i \cdot \boldsymbol{s}_i \tag{2.2.9}$$

H_{SOO} is the spin-other-orbit term

$$H_{SOO} = -\frac{\alpha^2}{2} \sum_{i<j}^{N} \frac{\boldsymbol{r}_{ij} \times \boldsymbol{p}_i}{r_{ij}^3} (\boldsymbol{s}_i + 2\boldsymbol{s}_j) \tag{2.2.10}$$

and H_{SS} is the spin-spin term

$$H_{OO} = \alpha^2 \sum_{i<j}^{N} \frac{1}{r_i^3} \left[\boldsymbol{s}_i \cdot \boldsymbol{s}_j - 3 \frac{(\boldsymbol{s}_i \cdot \boldsymbol{r}_{ij})(\boldsymbol{s}_j \cdot \boldsymbol{r}_{ij})}{r_{ij}^2} \right]. \tag{2.2.11}$$

The Breit-Pauli Hamiltonian commutes with the total angular momentum operator J, and thus the corresponding wave functions should be eigenfunctions of J^2 and J_z. In the multiconfiguration approximation the Breit-Pauli wave func-

tions are obtained as linear combinations

$$\Psi(\gamma JM_J) = \sum_{i=1}^{M} c_i \, \Phi_i(\gamma_i \, L_i S_i J M_J) \, , \tag{2.2.12}$$

where $\Phi_i(\gamma LSJM_J)$ are LSJ coupled CSFs, that is

$$\Phi_i(\gamma LSJM_J) = \sum_{M_L M_S} \langle LM_L SM_S | LSJM_J \rangle \Phi_i(\gamma_i \, LM_L SM_S) \, , \tag{2.2.13}$$

Since neither L nor S are good quantum numbers CSFs with different LS need to be included in the expansion (2.2.12), and we have a mixing of different LS terms. In this case the wave function is given in the so-called intermediate coupling.

2.3 Multiconfiguration Dirac-Hartree-Fock approach

In the multiconfiguration Dirac-Hartree-Fock (MCDHF) approximation, an atomic state function (ASF) of parity π, an $\Psi(\gamma\pi J)$, is given by a linear combination of CSFs with the same parity, $\Phi(\gamma_i \pi J)$, i.e.

$$\Psi(\gamma PJ) = \sum_i c_i \Phi(\gamma_i \pi J), \tag{2.3.1}$$

where J is the total angular momentum of the configuration. The multiconfiguration energy functional is based on the Dirac-Coulomb (DC) Hamiltonian, given by (in a.u.),

$$H_{DC} = \sum_{j=1}^{N} \Big(c\boldsymbol{\alpha}_j \cdot \boldsymbol{p}_j + (\beta_j - 1)c^2 + V(r_j) \Big) + \sum_{j<k}^{N} \frac{1}{r_{jk}}, \tag{2.3.2}$$

where $\boldsymbol{\alpha}$ and β are the fourth-order Dirac matrices, $\boldsymbol{p}$ is the momentum operator, and $V(r_j)$ is the central part of the electrostatic electron-nucleus interaction. In the calculations, the nuclear charge distribution was modeled by the two-component Fermi function.

The configuration state functions $\Phi(\gamma_i \pi J)$ are antisymmetrized linear combinations of products of relativistic orbitals

$$\phi(r) = \frac{1}{r} \begin{pmatrix} P_{n\kappa}(r)\chi_{\kappa m}(\hat{r}) \\ iQ_{n\kappa}(r)\chi_{-\kappa m}(\hat{r}) \end{pmatrix}. \tag{2.3.3}$$

Here κ is the relativistic angular quantum number, $P_{n\kappa}(r)$ and $Q_{n\kappa}(r)$ are the large and small component radial wavefunctions and $\chi_{\kappa m}(\hat{r})$ is the spinor spherical harmonic in the lsj coupling scheme

$$\chi_{\kappa m}(\hat{r}) = \sum_{m_l, m_s} \left\langle l \frac{1}{2} m_l m_s | jm \right\rangle Y_{lm_l}(\theta, \varphi) \xi_{m_s}(\sigma). \tag{2.3.4}$$

The radial functions $P_{n\kappa}(r)$ and $Q_{n\kappa}(r)$ are numerically represented on a logarithmic grid and are required to be orthonormal within each κ symmetry

$$\int_0^\infty [P_{n'\kappa}(r) P_{n\kappa}(r) + Q_{n'\kappa}(r) Q_{n\kappa}(r)]\, dr = \delta_{n'n}. \tag{2.3.5}$$

In the multiconfiguration self-consistent field (MC-SCF) procedure both the radial functions and the expansion coefficients for the configuration state functions are optimized to self-consistency.

2.4 Relativistic configuration interaction

In the relativistic configuration interaction (RCI) calculations the wave function is expanded in configuration state functions, but now only the expansion coefficients are determined. This is done by diagonalizing the hamiltonian matrix. In the RCI calculations the transverse photon interaction [21]

$$H_{\text{Breit}} = -\sum_{i<j}^{N} \left[\boldsymbol{\alpha}_i \cdot \boldsymbol{\alpha}_j \frac{\cos(\omega_{ij} r_{ij}/c)}{r_{ij}} + (\boldsymbol{\alpha}_i \cdot \boldsymbol{\nabla}_i)(\boldsymbol{\alpha}_j \cdot \boldsymbol{\nabla}_j) \frac{\cos(\omega_{ij} r_{ij}/c) - 1}{\omega_{ij}^2 r_{ij}/c^2} \right] \tag{2.4.1}$$

may be included in the hamiltonian. The photon frequency ω_{ij} used by the RCI program in calculating the matrix elements of the transverse photon interaction is taken to be the difference in the diagonal Lagrange multipliers ε_i and ε_j associated with the orbitals. In general, diagonal Lagrange multipliers are approximate electron removal energies only when orbitals are spectroscopic and singly occupied. Thus it is not known how well the multiconfiguration Dirac-Fock method can determine the full transverse photon interaction when correlation orbitals are present. Frequently, only the low frequency limit $\omega_{ij} \longrightarrow 0$, referred to as the Breit interaction, is used.

2.5 Computation of transition parameters

The evaluation of radiative transition data (transition probabilities, oscillator strengths) between two states $\gamma'\pi'J'M'$ and $\gamma\pi JM$ built on different and independently optimized orbital sets is non-trivial. The transition data can be expressed in terms of the transition moment which is defined as

$$\langle \Psi(\gamma\pi J) \| \mathbf{T} \| \Psi(\gamma'\pi'J') \rangle = \sum_{j,k} c_j c'_k \langle \Phi(\gamma_j \pi J) \| \mathbf{T} \| \Phi(\gamma'_k \pi' J') \rangle, \qquad (2.5.1)$$

where $\mathbf{T}$ is the transition operator. For electric multipole transitions there are two forms of the transition operator, the length (Babushkin) and velocity (Coulomb) forms [22]. For the multiconfiguration Dirac-Hartree-Fock solutions the agreement in the two values may be used as an indicator of accuracy [23]. The calculation of the transition moment breaks down to the task of summing up reduced matrix elements between different CSFs. Since the orbitals of the initial and final states are orthonormal but different, the two states $\gamma'\pi'J'M'$ and $\gamma\pi JM$ were transformed in such a way that the orbital sets became biorthonormal [19]. Standard methods were then used to evaluate the matrix elements for the transformed CSFs.

2.6 Biorthogonal transformations

The biorthogonal transformation is explained in details in [19] focusing on the calculation of transition probabilities using nonorthogonal orbitals. This method has been implemented in ATSP2K [24] and in GRASP2K [25, 26] for the calculation of transition data. The idea is simple: two orbital sets that are not orthonormal to each other are first transformed to become biorthonormal. For a coupling matrix element $\langle \tilde{\Lambda}_l | H | \tilde{\Lambda}_r \rangle$ built in their own orbital basis $\left\{\phi_i^L\right\}$ and $\left\{\phi_j^R\right\}$ that are not orthonormal,

$$\langle \phi_i^L | \phi_j^R \rangle = S_{ij}^{LR}, \qquad (2.6.1)$$

linear transformations

$$\phi^A = \phi^L \mathbf{C}^{LA}; \quad \phi^B = \phi^R \mathbf{C}^{RB}, \qquad (2.6.2)$$

are found to transform the two original orbital sets into two new biorthonormal sets

$$\langle \phi_i^A | \phi_j^B \rangle = \delta_{ij}, \tag{2.6.3}$$

The advantage of the biorthonormality property (2.6.3) of the transformed orbital sets is that the evaluation of any matrix element can proceed as in the orthonormal case, as originally found by Moshinsky and Seligman [27]. There is an infinity of pairs of transformation matrices ($\mathbf{C}^{LA}$, $\mathbf{C}^{RB}$) that produce biorthonormal basis sets. In our approach [19], the choice adopted is predicted by the restrictions on the configuration state function spaces used for $\tilde{\Lambda}_l$ and $\tilde{\Lambda}_r$. We require the transformation matrices to be upper triangular, a suitable choice for estimating the effect of the orbital transformation on the mixing coefficients $\{\alpha_i^L\} \rightarrow \{\alpha_i^A\}$ / $\{\alpha_i^R\} \rightarrow \{\alpha_i^B\}$ giving the two representations of the $|\tilde{\Lambda}_l\rangle$ and $|\tilde{\Lambda}_r\rangle$ functions in both original and transformed (biorthonormal) basis sets

$$|\tilde{\Lambda}_l\rangle = \sum_i \alpha_i^L |\Phi_i^L\rangle = \sum_i \alpha_i^A |\Phi_i^A\rangle \tag{2.6.4}$$

$$|\tilde{\Lambda}_r\rangle = \sum_i \alpha_i^R |\Phi_i^R\rangle = \sum_i \alpha_i^B |\Phi_i^B\rangle \, . \tag{2.6.5}$$

There is an important built-in constraint in the algorithm: the wavefunction expansion spaces for both left and right should be 'closed under de-excitation' to allow this class of transformation. Restricted active space (RAS) and complete active space (CAS) expansions satisfy this property.

2.7 Tensorial expressions for two–particle operator

A scalar two–particle operator may be presented in the following form [28, 29]:

$$\widehat{G}^{(\kappa_1 \kappa_2 k, \sigma_1 \sigma_2 k)} = \sum_{i>j} g(r_i, r_j) \sum_p (-1)^{k-p} \left[\widehat{g}_i^{(\kappa_1 \sigma_1)} \times \widehat{g}_j^{(\kappa_2 \sigma_2)} \right]_{p,-p}^{(k\ k)}, \tag{2.7.1}$$

where $g(r_i, r_j)$ is the radial part of the operator, $\widehat{g}_i^{(\kappa_1 \sigma_1)}$ is a tensor acting upon the orbital and spin variables of the i–th function, κ_1, κ_2 are the ranks of the operator acting in orbital space, and σ_1, σ_2 are the ranks of the operator acting in spin space.

A two–particle operator in second quantization method is written as follows:

$$G^{(\kappa_1\kappa_2 k,\sigma_1\sigma_2 k)} = \sum_{n_i l_i, n_j l_j, n_{i'} l_{i'}, n_{j'} l_{j'}} \widehat{G}(ij,i'j') = \frac{1}{2}\sum_{i,j,i',j'} a_i a_j a^{\dagger}_{j'} a^{\dagger}_{i'} \left(i,j\,|g|\,i',j'\right), \tag{2.7.2}$$

where $i \equiv n_i l_i s m_{l_i} m_{s_i}$, $(i,j|g|i',j')$ is the two–electron matrix element of the operator $G^{(\kappa_1\kappa_2 k,\sigma_1\sigma_2 k)}$, and a_i is the electron creation and $a^{\dagger}_j$ the electron annihilation operators. Meanwhile two tensorial forms are well known in second quantization [30]. In the first form the two–electron operator has the tensorial product

$$\left[\left[a^{(\lambda_i)} \times a^{(\lambda_j)}\right]^{(\kappa_{12}\sigma_{12})} \times \left[\tilde{a}{}^{(\lambda'_i)} \times \tilde{a}{}^{(\lambda'_j)}\right]^{(\kappa'_{12}\sigma'_{12})}\right]^{(kk)}_{p,-p}. \tag{2.7.3}$$

The tensor $\tilde{a}{}^{(\lambda)}_{m_\lambda}$ is defined as

$$\tilde{a}{}^{(\lambda)}_{m_\lambda} = (-1)^{\lambda - m_\lambda}\, a^{\dagger(\lambda)}_{-m_\lambda}, \tag{2.7.4}$$

where $\lambda \equiv l,s$ in non–relativistic theory and $\lambda \equiv j$ in relativistic theory.

In the second form the second quantization operators are coupled by pairs consisting of electron creation and annihilation operators. In the paper by Gaigalas *et al.* [31] the following general expression of two–particle operator is proposed, which allows one to make the most of the advantages of Racah algebra [32]–[35].

$$\begin{aligned}
\widehat{G}^{(\kappa_1\kappa_2 k,\sigma_1\sigma_2 k)} = \sum_{\alpha}\sum_{\kappa_{12},\sigma_{12},\kappa'_{12},\sigma'_{12}} \Theta(\Xi)\Big\{ & A^{(kk)}_{p,-p}(n_\alpha\lambda_\alpha,\Xi)\,\delta(u,1) \\
& + \sum_{\beta}\left[B^{(\kappa_{12}\sigma_{12})}(n_\alpha\lambda_\alpha,\Xi) \times C^{(\kappa'_{12}\sigma'_{12})}\left(n_\beta\lambda_\beta,\Xi\right)\right]^{(kk)}_{p,-p}\delta(u,2) \\
& + \sum_{\beta\gamma}\left[\left[D^{(l_\alpha s)} \times D^{(l_\beta s)}\right]^{(\kappa_{12}\sigma_{12})} \times E^{(\kappa'_{12}\sigma'_{12})}\left(n_\gamma\lambda_\gamma,\Xi\right)\right]^{(kk)}_{p,-p}\delta(u,3) \\
& + \sum_{\beta\gamma\delta}\left[\left[D^{(l_\alpha s)} \times D^{(l_\beta s)}\right]^{(\kappa_{12}\sigma_{12})} \times \left[D^{(l_\gamma s)} \times D^{(l_\delta s)}\right]^{(\kappa'_{12}\sigma'_{12})}\right]^{(kk)}_{p,-p}\delta(u,4)\Big\}.
\end{aligned} \tag{2.7.5}$$

In the expression (2.7.5) u is the overall number of shells acted upon by a given tensorial product of creation/annihilation operators. The parameter Ξ denotes the whole array of parameters (and sometimes an internal summation over some of these is implied, as well) that connects the amplitudes Θ of tensorial products of creation/annihilation operators in the expression (2.7.5) to these tensorial products (see Gaigalas *et al.* [31]). Also, attention must be paid to the fact that the ranks κ_1, κ_2, κ, σ_1, σ_2 and σ are also included into the parameter Ξ.

Whereas in traditional expressions, e. g. (2.7.2), the summation runs over the principle and the orbital quantum numbers of open shells without detailing these, in the expression written above the first term represents the case of a two–particle operator acting upon the same shell $n_\alpha\lambda_\alpha$, the second term corresponds to the operator $\widehat{G}^{(\kappa_1\kappa_2 k,\sigma_1\sigma_2 k)}$ acting upon two different shells $n_\alpha\lambda_\alpha$, $n_\beta\lambda_\beta$. When the operator $\widehat{G}^{(\kappa_1\kappa_2 k,\sigma_1\sigma_2 k)}$ acts upon three shells the third term in (2.7.5) must be considered and when it acts upon four – the fourth one. It is defined in this expression the shells $n_\alpha\lambda_\alpha$, $n_\beta\lambda_\beta$, $n_\gamma\lambda_\gamma$, $n_\delta\lambda_\delta$ to be different. Thus, the expression (2.7.5) describe the most general use of the operator, suitable to account even for the matrix elements that are of non–diagonal with respect to the configuration.

The tensorial part of a two–particle operator is expressed in terms of operators of the type $A^{(kk)}(n\lambda,\Xi)$, $B^{(kk)}(n\lambda,\Xi)$, $C^{(kk)}(n\lambda,\Xi)$, $D^{(ls)}$, $E^{(kk)}(n\lambda,\Xi)$ (for more details see [31]). They correspond to one of the forms:

$$a^{(q\lambda)}_{m_q}, \tag{2.7.6}$$

$$\left[a^{(q\lambda)}_{m_{q1}} \times a^{(q\lambda)}_{m_{q2}}\right]^{(\kappa_1\sigma_1)}, \tag{2.7.7}$$

$$\left[a^{(q\lambda)}_{m_{q1}} \times \left[a^{(q\lambda)}_{m_{q2}} \times a^{(q\lambda)}_{m_{q3}}\right]^{(\kappa_1\sigma_1)}\right]^{(\kappa_2\sigma_2)}, \tag{2.7.8}$$

$$\left[\left[a^{(q\lambda)}_{m_{q1}} \times a^{(q\lambda)}_{m_{q2}}\right]^{(\kappa_1\sigma_1)} \times a^{(q\lambda)}_{m_{q3}}\right]^{(\kappa_2\sigma_2)}, \tag{2.7.9}$$

$$\left[\left[a^{(q\lambda)}_{m_{q1}} \times a^{(q\lambda)}_{m_{q2}}\right]^{(\kappa_1\sigma_1)} \times \left[a^{(q\lambda)}_{m_{q3}} \times a^{(q\lambda)}_{m_{q4}}\right]^{(\kappa_2\sigma_2)}\right]^{(kk)}. \tag{2.7.10}$$

For example, if we take a two–particle operator acting upon two shells, then we see from expression (2.7.5) that the spin–angular part of two–particle operator is expressed via operators $B^{(\kappa_{12}\sigma_{12})}\left(n_\alpha\lambda_\alpha,\Xi\right)$ and $C^{\left(\kappa'_{12}\sigma'_{12}\right)}\left(n_\beta\lambda_\beta,\Xi\right)$. In the case when the operator $\widehat{G}^{(\kappa_1\kappa_2 k,\sigma_1\sigma_2 k)}$ acts in such a manner that two operators of second quantization act upon one shell and two act upon another, the $B^{(\kappa_{12}\sigma_{12})}\left(n_\alpha\lambda_\alpha,\Xi\right)$ and $C^{\left(\kappa'_{12}\sigma'_{12}\right)}\left(n_\beta\lambda_\beta,\Xi\right)$ are expressed as (2.7.7). But in the case when three operators of second quantization act upon one shell and one acts upon another, then $B^{(\kappa_{12}\sigma_{12})}\left(n_\alpha\lambda_\alpha,\Xi\right)$ and $C^{\left(\kappa'_{12}\sigma'_{12}\right)}\left(n_\beta\lambda_\beta,\Xi\right)$ are expressed either as (2.7.6) and (2.7.8) or (2.7.6) and (2.7.9).

In writing down the expressions (2.7.6)–(2.7.10) the quasispin formalism was used, where $a^{(\lambda)}_{m_\lambda}$ and $\tilde{a}{}^{(\lambda)}_{m_\lambda}$ are components of the tensor $a^{(q\lambda)}_{m_q m_\lambda}$, having in additional quasispin space the rank $q=\frac{1}{2}$ and projections $m_q=\pm\frac{1}{2}$, i.e.

$$a^{(q\lambda)}_{\frac{1}{2}m_\lambda}=a^{(ls)}_{m_l m_s} \tag{2.7.11}$$

and

$$a^{(q\lambda)}_{-\frac{1}{2}m_\lambda}=\tilde{a}{}^{(ls)}_{m_l m_s}\,. \tag{2.7.12}$$

The amplitudes $\Theta\left(\Xi\right)$ are all proportional to the two–electron submatrix element of a two–particle operator g,

$$\Theta\left(\Xi\right)\sim\left(n_i\lambda_i n_j\lambda_j\left\|g\right\|n_{i'}\lambda_{i'}n_{j'}\lambda_{j'}\right). \tag{2.7.13}$$

According to the approach, [31], a general expression of a submatrix element for any two-particle operator between functions with u open shells can be written as follows:

$$\begin{aligned}
&\left(\psi_u\left(LS\right)\left\|\widehat{G}^{(\kappa_1\kappa_2 k,\sigma_1\sigma_2 k)}\right\|\psi_u\left(L'S'\right)\right)\\
&=\sum_{n_i l_i,n_j l_j,n'_i l'_i,n'_j l'_j}\left(\psi_u\left(LS\right)\left\|\widehat{G}\left(n_i l_i,n_j l_j,n'_i l'_i,n'_j l'_j\right)\right\|\psi_u\left(L'S'\right)\right)\\
&=\sum_{n_i l_i,n_j l_j,n'_i l'_i,n'_j l'_j}\sum_{\kappa_{12},\sigma_{12},\kappa'_{12},\sigma'_{12}}\sum_{K_l,K_s}\left(-1\right)^{\Delta}\Theta'\left(n_i\lambda_i,n_j\lambda_j,n'_i\lambda'_i,n'_j\lambda'_j,\Xi\right)\\
&\times T\left(n_i\lambda_i,n_j\lambda_j,n'_i\lambda'_i,n'_j\lambda'_j,\Lambda^{bra},\Lambda^{ket},\Xi,\Gamma\right)R\left(\lambda_i,\lambda_j,\lambda'_i,\lambda'_j,\Lambda^{bra},\Lambda^{ket},\Gamma\right).
\end{aligned} \tag{2.7.14}$$

So, to calculate the spin-angular part of a submatrix element of this type, one has to obtain:

1. **Recoupling matrix** $R\left(\lambda_i,\lambda_j,\lambda_i',\lambda_j',\Lambda^{bra},\Lambda^{ket},\Gamma\right)$. This recoupling matrix accounts for the change in going from matrix element $\left(\psi_u\left(LS\right)\left\|\widehat{G}\right\|\psi_u\left(L'S'\right)\right)$, which has u open shells in the *bra* and *ket* functions, to the submatrix element $T\left(n_i\lambda_i,n_j\lambda_j,n_i'\lambda_i',n_j'\lambda_j',\Lambda^{bra},\Lambda^{ket},\Xi,\Gamma\right)$, which has only the shells being acted upon by the two–particle operator in its *bra* and *ket* functions.

2. **Submatrix elements** $T\left(n_i\lambda_i,n_j\lambda_j,n_i'\lambda_i',n_j'\lambda_j',\Lambda^{bra},\Lambda^{ket},\Xi,\Gamma\right)$.

3. **Phase factor** Δ.

4. $\Theta'\left(n_i\lambda_i,n_j\lambda_j,n_i'\lambda_i',n_j'\lambda_j',\Xi\right)$, which is proportional to the radial part. It consists of a submatrix element $\left(n_i\lambda_i n_j\lambda_j\left\|g^{(\kappa_1\kappa_2 k,\sigma_1\sigma_2 k)}\right\|\psi_u\left(L'S'\right)\right)$, in some cases of simple factors and $3nj$-coefficients.

Some important points to note are the following:

The recoupling matrices $R\left(\lambda_i,\lambda_j,\lambda_i',\lambda_j',\Lambda^{bra},\Lambda^{ket},\Gamma\right)$ in this approach are much simpler than in other known approaches. We have obtained their analytical expressions in terms of just $6j-$ and $9j-$coefficients. That is why it is chosen a special form of an operator in second quantization, where second quantization operators acting upon the same shell are tensorially coupled together.

The tensorial part of a two-particle operator is expressed in terms of (products of) operators of the type $A^{(kk)}(n\lambda,\Xi)$, $B^{(kk)}(n\lambda,\Xi)$, $C^{(kk)}(n\lambda,\Xi)$, $D^{(ls)}$, $E^{(kk)}(n\lambda,\Xi)$. Their explicit expressions are (2.7.6–2.7.10). We denote their submatrix elements by $T\left(n_i\lambda_i,n_j\lambda_j,n_i'\lambda_i',n_j'\lambda_j',\Lambda^{bra},\Lambda^{ket},\Xi,\Gamma\right)$. The parameter Γ represents the whole array of parameters connecting the recoupling matrix R to the submatrix element T. It is worth noting that each of the tensorial quantities (2.7.6–2.7.10) acts upon one and the same shell. So, all the advantages of tensor algebra and the quasispin formalism may be efficiently exploited in the process of their calculation.

As seen, by using this approach, the calculation of the angular parts of matrix elements between functions with u open shells ends up as a calculation of submatrix elements of tensors (2.7.6), (2.7.7) within a single shell of equivalent electrons.

In the work by Gaigalas *et al.* [31] there is chosen an optimal number of distributions, which is necessary to obtain the matrix elements of any two–electron operator, when the *bra* and *ket* functions consist of arbitrary number of shells. This is presented in Table 2.7.1. We point out that for distributions 2–5 and 19–42 the shells' sequence numbers α, β, γ, δ (in *bra* and *ket* functions of a submatrix element) satisfy the condition $\alpha < \beta < \gamma < \delta$, while for distributions 6–18 no conditions upon α, β, γ, δ are imposed. This permits to reduce the number of distributions. For distributions 19–42 this condition is imposed only for obtaining simple analytical expressions for the recoupling matrices $R\left(\lambda_i, \lambda_j, \lambda_i', \lambda_j', \Lambda^{bra}, \Lambda^{ket}, \Gamma\right)$.

Table 2.7.1: Distributions of shells, upon which the second quantization operators are acting, that appear in the submatrix elements of any two–particle operator, when *bra* and *ket* functions have u open shells [31].

No.	a_i	a_j	$a_{i'}^{\dagger}$	$a_{j'}^{\dagger}$	**submatrix element**
1.	α	α	α	α	$\left(\ldots n_\alpha l_\alpha^{N_\alpha} \ldots \middle\| \widehat{G}(n_i l_i n_j l_j n_i' l_i' n_j' l_j') \middle\| \ldots n_\alpha l_\alpha^{N_\alpha} \ldots\right)$
2.	α	β	α	β	
3.	β	α	β	α	$\left(\ldots n_\alpha l_\alpha^{N_\alpha} \ldots n_\beta l_\beta^{N_\beta} \ldots \middle\|\right.$
4.	α	β	β	α	$\widehat{G}(n_i l_i n_j l_j n_i' l_i' n_j' l_j')$
5.	β	α	α	β	$\left.\middle\| \ldots n_\alpha l_\alpha^{N_\alpha} \ldots n_\beta l_\beta^{N_\beta} \ldots\right)$
6.	α	α	β	β	$\left(\ldots n_\alpha l_\alpha^{N_\alpha} \ldots n_\beta l_\beta^{N_\beta} \ldots \middle\| \widehat{G} \middle\| \ldots n_\alpha l_\alpha^{N_\alpha-2} \ldots n_\beta l_\beta^{N_\beta+2} \ldots\right)$
7.	β	α	α	α	
8.	α	β	α	α	$\left(\ldots n_\alpha l_\alpha^{N_\alpha} \ldots n_\beta l_\beta^{N_\beta} \ldots \middle\|\right.$
9.	β	β	β	α	$\widehat{G}(n_i l_i n_j l_j n_i' l_i' n_j' l_j')$
10.	β	β	α	β	$\left.\middle\| \ldots n_\alpha l_\alpha^{N_\alpha+1} \ldots n_\beta l_\beta^{N_\beta-1} \ldots\right)$
11.	β	γ	α	γ	
12.	γ	β	γ	α	$\left(\ldots n_\alpha l_\alpha^{N_\alpha} n_\beta l_\beta^{N_\beta} n_\gamma l_\gamma^{N_\gamma} \ldots \middle\|\right.$
13.	γ	β	α	γ	$\widehat{G}(n_i l_i n_j l_j n_i' l_i' n_j' l_j')$
14.	β	γ	γ	α	$\left.\middle\| \ldots n_\alpha l_\alpha^{N_\alpha+1} n_\beta l_\beta^{N_\beta-1} n_\gamma l_\gamma^{N_\gamma} \ldots\right)$
15.	γ	γ	α	β	$\left(\ldots n_\alpha l_\alpha^{N_\alpha} n_\beta l_\beta^{N_\beta} n_\gamma l_\gamma^{N_\gamma} \ldots \middle\| \widehat{G}(n_i l_i n_j l_j n_i' l_i' n_j' l_j')\right.$
16.	γ	γ	β	α	$\left.\middle\| \ldots n_\alpha l_\alpha^{N_\alpha+1} n_\beta l_\beta^{N_\beta+1} n_\gamma l_\gamma^{N_\gamma-2} \ldots\right)$
17.	α	β	γ	γ	$\left(\ldots n_\alpha l_\alpha^{N_\alpha} n_\beta l_\beta^{N_\beta} n_\gamma l_\gamma^{N_\gamma} \ldots \middle\| \widehat{G}(n_i l_i n_j l_j n_i' l_i' n_j' l_j')\right.$
18.	β	α	γ	γ	$\left.\middle\| \ldots n_\alpha l_\alpha^{N_\alpha-1} n_\beta l_\beta^{N_\beta-1} n_\gamma l_\gamma^{N_\gamma+2} \ldots\right)$

Table 2.7.1: (continued).

19.	α	β	γ	δ	$\Big(n_\alpha l_\alpha^{N_\alpha} n_\beta l_\beta^{N_\beta} n_\gamma l_\gamma^{N_\gamma} n_\delta l_\delta^{N_\delta} \Big\|$
20.	β	α	γ	δ	$\widehat{G}(n_i l_i n_j l_j n_i' l_i' n_j' l_j')$
21.	α	β	δ	γ	$\Big\| n_\alpha l_\alpha^{N_\alpha-1} n_\beta l_\beta^{N_\beta-1} n_\gamma l_\gamma^{N_\gamma+1} n_\delta l_\delta^{N_\delta+1}\Big)$
22.	β	α	δ	γ	
23.	γ	δ	α	β	$\Big(n_\alpha l_\alpha^{N_\alpha} n_\beta l_\beta^{N_\beta} n_\gamma l_\gamma^{N_\gamma} n_\delta l_\delta^{N_\delta} \Big\|$
24.	γ	δ	β	α	$\widehat{G}(n_i l_i n_j l_j n_i' l_i' n_j' l_j')$
25.	δ	γ	α	β	$\Big\| n_\alpha l_\alpha^{N_\alpha+1} n_\beta l_\beta^{N_\beta+1} n_\gamma l_\gamma^{N_\gamma-1} n_\delta l_\delta^{N_\delta-1}\Big)$
26.	δ	γ	β	α	
27.	α	γ	β	δ	$\Big(n_\alpha l_\alpha^{N_\alpha} n_\beta l_\beta^{N_\beta} n_\gamma l_\gamma^{N_\gamma} n_\delta l_\delta^{N_\delta} \Big\|$
28.	α	γ	δ	β	$\widehat{G}(n_i l_i n_j l_j n_i' l_i' n_j' l_j')$
29.	γ	α	δ	β	$\Big\| n_\alpha l_\alpha^{N_\alpha-1} n_\beta l_\beta^{N_\beta+1} n_\gamma l_\gamma^{N_\gamma-1} n_\delta l_\delta^{N_\delta+1}\Big)$
30.	γ	α	β	δ	
31.	β	δ	α	γ	$\Big(n_\alpha l_\alpha^{N_\alpha} n_\beta l_\beta^{N_\beta} n_\gamma l_\gamma^{N_\gamma} n_\delta l_\delta^{N_\delta} \Big\|$
32.	δ	β	γ	α	$\widehat{G}(n_i l_i n_j l_j n_i' l_i' n_j' l_j')$
33.	β	δ	γ	α	$\Big\| n_\alpha l_\alpha^{N_\alpha+1} n_\beta l_\beta^{N_\beta-1} n_\gamma l_\gamma^{N_\gamma+1} n_\delta l_\delta^{N_\delta-1}\Big)$
34.	δ	β	α	γ	
35.	α	δ	β	γ	$\Big(n_\alpha l_\alpha^{N_\alpha} n_\beta l_\beta^{N_\beta} n_\gamma l_\gamma^{N_\gamma} n_\delta l_\delta^{N_\delta} \Big\|$
36.	δ	α	γ	β	$\widehat{G}(n_i l_i n_j l_j n_i' l_i' n_j' l_j')$
37.	α	δ	γ	β	$\Big\| n_\alpha l_\alpha^{N_\alpha-1} n_\beta l_\beta^{N_\beta+1} n_\gamma l_\gamma^{N_\gamma+1} n_\delta l_\delta^{N_\delta-1}\Big)$
38.	δ	α	β	γ	
39.	β	γ	α	δ	$\Big(n_\alpha l_\alpha^{N_\alpha} n_\beta l_\beta^{N_\beta} n_\gamma l_\gamma^{N_\gamma} n_\delta l_\delta^{N_\delta} \Big\|$
40.	γ	β	δ	α	$\widehat{G}(n_i l_i n_j l_j n_i' l_i' n_j' l_j')$
41.	β	γ	δ	α	$\Big\| n_\alpha l_\alpha^{N_\alpha+1} n_\beta l_\beta^{N_\beta-1} n_\gamma l_\gamma^{N_\gamma-1} n_\delta l_\delta^{N_\delta+1}\Big)$
42.	γ	β	α	δ	

2.7.1 Breit-Pauli Hamiltonian in biorthogonal orbital basis

To study various atomic properties in a biorthogonal orbital basis we need to revise the spin-angular formalism. The *bra* and *ket* functions differ in a biorthogonal orbital basis, so it's needed to reject some symmetries changing *bra* and *ket* functions in the radial integrals. In the thesis spin-angular formalism [36, 37] was revised and redefined. In this section we give what modifications was done for certain interactions:

- *spin-spin interaction*

  The spin–spin operator H^{ss} itself contains tensorial structure of two different types, summed over k [38],

$$H^{ss} \equiv \sum_k \left[H_{ss}^{(k+1k-12,112)} + H_{ss}^{(k-1k+12,112)} \right]. \tag{2.7.15}$$

  The submatrix elements of the H^{ss} operator are

$$\begin{aligned} &\left(n_i \lambda_i n_j \lambda_j \left\| H_{ss}^{(k+1k-12,112)} \right\| n_{i'} \lambda_{i'} n_{j'} \lambda_{j'} \right) \\ &\quad = \frac{3}{\sqrt{5}} \sqrt{(2k+3)^{(5)}} \left(l_i \left\| C^{(k+1)} \right\| l_{i'} \right) \left(l_j \left\| C^{(k-1)} \right\| l_{j'} \right) \\ &\quad \times N^{k-1} \left(n_i l_i n_j l_j, n_{i'} l_{i'} n_{j'} l_{j'} \right), \end{aligned} \tag{2.7.16}$$

$$\begin{aligned} &\left(n_i \lambda_i n_j \lambda_j \left\| H_{ss}^{(k-1k+12,112)} \right\| n_{i'} \lambda_{i'} n_{j'} \lambda_{j'} \right) \\ &\quad = \frac{3}{\sqrt{5}} \sqrt{(2k+3)^{(5)}} \left(l_i \left\| C^{(k-1)} \right\| l_{i'} \right) \left(l_j \left\| C^{(k+1)} \right\| l_{j'} \right) \\ &\quad \times N^{k-1} \left(n_j l_j n_i l_i, n_{j'} l_{j'} n_{i'} l_{i'} \right), \end{aligned} \tag{2.7.17}$$

  where $(2k+3)^{(5)} \equiv (2k+3)(2k+2)(2k+1)(2k)(2k-1)$. The radial integral N^k in (2.7.16), (2.7.17) is defined as in Glass and Hibbert [39]:

$$\begin{aligned} &N^k \left(n_i l_i n_j l_j, n_{i'} l_{i'} n_{j'} l_{j'} \right) \\ &\quad = \frac{\alpha^2}{4} \int_0^\infty \int_0^\infty P_i(r_1) P_j(r_2) \frac{r_2^k}{r_1^{k+3}} \varepsilon(r_1 - r_2) P_{i'}(r_1) P_{j'}(r_2) \, dr_1 dr_2, \end{aligned} \tag{2.7.18}$$

  where $\varepsilon(x)$ is a Heaviside step–function,

$$\varepsilon(x) = \begin{cases} 1; & \text{for } x > 0, \\ 0; & \text{for } x \leq 0. \end{cases} \tag{2.7.19}$$

  In general, the previous formalism is appropriate for a biorthogonal orbital basis except for a few cases. It is for $\alpha\beta\beta\alpha$ and $\beta\alpha\alpha\beta$ distributions.

Operator H^{ss} has the tensorial structure given below for the $\alpha\beta\beta\alpha$ distribution

$$H_{12}^{ss} \equiv \sum_k \left[H(\alpha\beta\beta\alpha)_{ss}^{(k+1k-12,112)} + H(\alpha\beta\beta\alpha)_{ss}^{(k-1k+12,112)} \right] \quad (2.7.20)$$

and its submatrix elements considering (2.7.16–2.7.17) are

$$\begin{aligned} &\left(n_\alpha \lambda_\alpha n_\beta \lambda_\beta \left\| H(\alpha\beta\beta\alpha)_{ss}^{(k+1k-12,112)} \right\| n_\beta \lambda_\beta n_\alpha \lambda_\alpha \right) \\ &\quad = \frac{3}{\sqrt{5}} \sqrt{(2k+3)^{(5)}} \left(l_\alpha \left\| C^{(k+1)} \right\| l_\beta \right) \left(l_\beta \left\| C^{(k-1)} \right\| l_\alpha \right) \\ &\quad \times N^{k-1} \left(n_\alpha l_\alpha n_\beta l_\beta, n_\beta l_\beta n_\alpha l_\alpha \right), \end{aligned} \quad (2.7.21)$$

$$\begin{aligned} &\left(n_\alpha \lambda_\alpha n_\beta \lambda_\beta \left\| H(\alpha\beta\beta\alpha)_{ss}^{(k-1k+12,112)} \right\| n_\beta \lambda_\beta n_\alpha \lambda_\alpha \right) \\ &\quad = \frac{3}{\sqrt{5}} \sqrt{(2k+3)^{(5)}} \left(l_\alpha \left\| C^{(k-1)} \right\| l_\beta \right) \left(l_\beta \left\| C^{(k+1)} \right\| l_\alpha \right) \\ &\quad \times N^{k-1} \left(n_\beta l_\beta n_\alpha l_\alpha, n_\alpha l_\alpha n_\beta l_\beta \right). \end{aligned} \quad (2.7.22)$$

For the $\beta\alpha\alpha\beta$ distribution the operator H^{ss} has the tensorial structure

$$H_{12}^{ss} \equiv \sum_k \left[H(\beta\alpha\alpha\beta)_{ss}^{(k+1k-12,112)} + H(\beta\alpha\alpha\beta)_{ss}^{(k-1k+12,112)} \right] \quad (2.7.23)$$

and its submatrix elements considering (2.7.16–2.7.17) are

$$\begin{aligned} &\left(n_\beta \lambda_\beta n_\alpha \lambda_\alpha \left\| H(\beta\alpha\alpha\beta)_{ss}^{(k+1k-12,112)} \right\| n_\alpha \lambda_\alpha n_\beta \lambda_\beta \right) \\ &\quad = \frac{3}{\sqrt{5}} \sqrt{(2k+3)^{(5)}} \left(l_\beta \left\| C^{(k+1)} \right\| l_\alpha \right) \left(l_\alpha \left\| C^{(k-1)} \right\| l_\beta \right) \\ &\quad \times N^{k-1} \left(n_\beta l_\beta n_\alpha l_\alpha, n_\alpha l_\alpha n_\beta l_\beta \right), \end{aligned} \quad (2.7.24)$$

$$\left(n_\beta\lambda_\beta n_\alpha\lambda_\alpha\left\|H(\beta\alpha\alpha\beta)^{(k-1k+12,112)}_{ss}\right\|n_\alpha\lambda_\alpha n_\beta\lambda_\beta\right)$$
$$=\frac{3}{\sqrt{5}}\sqrt{(2k+3)^{(5)}}\left(l_\beta\left\|C^{(k-1)}\right\|l_\alpha\right)\left(l_\alpha\left\|C^{(k+1)}\right\|l_\beta\right)$$
$$\times N^{k-1}\left(n_\alpha l_\alpha n_\beta l_\beta, n_\beta l_\beta n_\alpha l_\alpha\right). \qquad (2.7.25)$$

These distributions have similar tensorial structure. So in an orthogonal basis we can reduce the number of tensorial structures using the symmetry. The sum of operators for $\alpha\beta\beta\alpha$ and $\beta\alpha\alpha\beta$ distributions

$$H(\alpha\beta\beta\alpha)^{ss}_{12}+H(\beta\alpha\alpha\beta)^{ss}_{12}$$
$$=-\frac{1}{\sqrt{5}}\sum_{k,p}\sum_{\kappa_{12}\kappa'_{12}}\sqrt{(2k+3)^{(5)}}\left(l_\alpha\left\|C^{(k+1)}\right\|l_\beta\right)\left(l_\alpha\left\|C^{(k-1)}\right\|l_\beta\right)$$
$$\times N^{k-1}\left(n_\alpha l_\alpha n_\beta l_\beta, n_\beta l_\beta n_\alpha l_\alpha\right)\left[(-1)^{\kappa'_{12}}+(-1)^{\kappa_{12}}\right]$$
$$\times(-1)^{k-p}[\kappa_{12},\kappa'_{12}]^{1/2}\begin{Bmatrix} l_\alpha & l_\beta & k+1\\ l_\alpha & l_\beta & k-1\\ \kappa_{12} & \kappa'_{12} & 2\end{Bmatrix}$$
$$\times\left[[a^{(l_\alpha s)}\times\tilde{a}^{(l_\alpha s)}]^{(\kappa_{12}1)}[a^{(l_\beta s)}\times\tilde{a}^{(l_\beta s)}]^{(\kappa'_{12}1)}\right]^{(22)}_{(p,-p)}. \qquad (2.7.26)$$

This allows for these two ($\alpha\beta\beta\alpha$ and $\beta\alpha\alpha\beta$) distributions at the same time calculate spin-angular part and radial integrals. Studying spin–spin interaction in a biorthogonal orbital basis we reject this symmetry

$$N^{k-1}\left(n_\alpha l_\alpha n_\beta l_\beta, n_\beta l_\beta n_\alpha l_\alpha\right)\neq N^{k-1}\left(n_\beta l_\beta n_\alpha l_\alpha, n_\alpha l_\alpha n_\beta l_\beta\right). \qquad (2.7.27)$$

Refusing the symmetry we get the expression below instead of (2.7.26)

$$
\begin{aligned}
&H(\alpha\beta\beta\alpha)^{ss}_{12} + H(\beta\alpha\alpha\beta)^{ss}_{12} \\
&\quad = -\frac{1}{\sqrt{5}} \sum_{k,p} \sum_{\kappa_{12}\kappa'_{12}} \sqrt{(2k+3)^{(5)}} \left(l_\alpha \left\| C^{(k+1)} \right\| l_\beta\right) \left(l_\alpha \left\| C^{(k-1)} \right\| l_\beta\right) \\
&\quad \times \Big[(-1)^{\kappa'_{12}} N^{k-1}\left(n_\alpha l_\alpha n_\beta l_\beta, n_\beta l_\beta n_\alpha l_\alpha\right) \\
&\qquad\qquad + \ (-1)^{\kappa_{12}} N^{k-1}\left(n_\beta l_\beta n_\alpha l_\alpha, n_\alpha l_\alpha n_\beta l_\beta\right)\Big] \\
&\quad \times (-1)^{k-p}[\kappa_{12},\kappa'_{12}]^{1/2} \begin{Bmatrix} l_\alpha & l_\beta & k+1 \\ l_\alpha & l_\beta & k-1 \\ \kappa_{12} & \kappa'_{12} & 2 \end{Bmatrix} \\
&\quad \times \left[\left[a^{(l_\alpha s)} \times \tilde{a}^{(l_\alpha s)}\right]^{(\kappa_{12}1)} \left[a^{(l_\beta s)} \times \tilde{a}^{(l_\beta s)}\right]^{(\kappa'_{12}1)}\right]^{(22)}_{(p,-p)}.
\end{aligned}
\tag{2.7.28}
$$

So in a biorthogonal orbital basis, instead using (2.7.26), we use (2.7.28). Comparing these expressions we see that spin-angular part is the same and we calculate it just once, but radial integrals we calculate for each of the distributions separately.

- *spin-other-orbit interaction*

  The spin–other–orbit operator H^{soo} itself contains tensorial structure of six different types, summed over k (Gaigalas *et al.* [40]):

$$
\begin{aligned}
H^{sso} \equiv \sum_k \Big[& H^{(k-1k1,101)}_{sso} + H^{(k-1k1,011)}_{sso} + H^{(kk1,101)}_{sso} \\
& + H^{(kk1,011)}_{sso} + H^{(k+1k1,101)}_{sso} + H^{(k+1k1,011)}_{sso}\Big].
\end{aligned}
\tag{2.7.29}
$$

  Their submatrix elements are:

$$
\begin{aligned}
&\left(n_i\lambda_i n_j\lambda_j \left\| H^{(k-1k1,\sigma_1\sigma_2 1)}_{soo} \right\| n_{i'}\lambda_{i'} n_{j'}\lambda_{j'}\right) \\
&\quad = 2\cdot 2^{\sigma_2}(k)^{-1/2}\left\{(2k-1)(2k+1)(l_i+l_{i'}-k+1)(k-l_i+l_{i'})\right. \\
&\quad \left.\times (k+l_i-l_{i'})(k+l_i+l_{i'}+1)\right\}^{1/2} \left(l_i \left\| C^{(k)} \right\| l_{i'}\right) \left(l_j \left\| C^{(k)} \right\| l_{j'}\right) \\
&\quad \times N^{k-2}\left(n_j l_j n_i l_i, n_{j'} l_{j'} n_{i'} l_{i'}\right),
\end{aligned}
\tag{2.7.30}
$$

$$\left(n_i\lambda_i n_j\lambda_j\left\|H_{soo}^{(kk1,\sigma_1\sigma_2 1)}\right\|n_{i'}\lambda_{i'}n_{j'}\lambda_{j'}\right)$$
$$=-2\cdot 2^{\sigma_2}(2k+1)^{1/2}\left(l_i\left\|C^{(k)}\right\|l_{i'}\right)\left(l_j\left\|C^{(k)}\right\|l_{j'}\right)\left\{(k(k+1))^{-1/2}\right.$$
$$\times(l_i(l_i+1)-k(k+1)-l_{i'}(l_{i'}+1))\left\{(k+1)N^{k-2}\left(n_j l_j n_i l_i, n_{j'}l_{j'}n_{i'}l_{i'}\right)\right.$$
$$\left.\left.-kN^k\left(n_i l_i n_j l_j, n_{i'}l_{i'}n_{j'}l_{j'}\right)\right\}-2(k(k+1))^{1/2}V^{k-1}\left(n_i l_i n_j l_j, n_{i'}l_{i'}n_{j'}l_{j'}\right)\right\}, \tag{2.7.31}$$

$$\left(n_i\lambda_i n_j\lambda_j\left\|H_{soo}^{(k+1k1,\sigma_1\sigma_2 1)}\right\|n_{i'}\lambda_{i'}n_{j'}\lambda_{j'}\right)$$
$$=2\cdot 2^{\sigma_2}(k+1)^{-1/2}\{(2k+1)(2k+3)(l_i+l_{i'}-k)(k-l_i+l_{i'}+1)$$
$$\times(k+l_i-l_{i'}+1)(k+l_i+l_{i'}+2)\}^{1/2}\left(l_i\left\|C^{(k)}\right\|l_{i'}\right)\left(l_j\left\|C^{(k)}\right\|l_{j'}\right)$$
$$\times N^k\left(n_i l_i n_j l_j, n_{i'}l_{i'}n_{j'}l_{j'}\right). \tag{2.7.32}$$

The radial integrals in (2.7.30)–(2.7.32) are as in Glass and Hibbert [39]:

$$V^k\left(n_i l_i n_j l_j, n_{i'}l_{i'}n_{j'}l_{j'}\right)$$
$$=\frac{\alpha^2}{4}\int_0^\infty\int_0^\infty P_i(r_1)P_j(r_2)\frac{r_<^{k-1}}{r_>^{k+2}}r_2\frac{\partial}{\partial r_1}P_{i'}(r_1)P_{j'}(r_2)\,dr_1dr_2. \tag{2.7.33}$$

For $\alpha\alpha\alpha\alpha$, $\alpha\beta\alpha\beta$ and $\beta\alpha\beta\alpha$ distributions in an orthogonal basis it was made some simplification. According to the relation for radial integrals

$$V^{k-1}\left(n_i l_i n_j l_j, n_{i'}l_{i'}n_{j'}l_{j'}\right)+V^{k-1}\left(n_{i'}l_{i'}n_{j'}l_{j'}, n_i l_i n_j l_j\right)$$
$$=kN^k\left(n_i l_i n_j l_j, n_{i'}l_{i'}n_{j'}l_{j'}\right)-(k+1)N^{k-2}\left(n_j l_j n_i l_i, n_{j'}l_{j'}n_{i'}l_{i'}\right) \tag{2.7.34}$$

in tensorial structures $(kk1,101)$ and $(kk1,011)$ (2.7.31) those integrals compensate each other. So in orthogonal basis we haved four different tensorial structures instead of six. In biorthogonal orbital basis we refuse that simplification and use (2.7.29).

Realization of biorthogonal orbital approximation in the LIBANG library. The above described modifications were made in the programs: SS1221.F for spin–spin interaction and in TWO1.F for spin–other orbit interaction. For other interactions we don't need to modify expressions theoretically, just programmatically. Such modifications were made in NONRELAT51.F, NONRELAT52.F, NONRELAT53.F, RK.F for orbit–orbit interaction and in NONRELAT31.F for one–electron operator.

2.8 A Partitioned Correlation Function Interaction approach

An ASF in the Partitioned Correlation Function Interaction approach is determined as the sum of the multireference (MR) function and by p partitioned correlation functions (PCFs)

$$|\Psi(\gamma LS^{\pi})\rangle = |\Psi^{\mathrm{MR}}(\gamma LS^{\pi})\rangle + \sum_{i=1}^{p} \alpha_i \, |\Lambda_i\rangle \ , \tag{2.8.1}$$

each of the PCFs corresponding to a given partition of the correlation function (CF) space:

$$|\Lambda\rangle = \sum_{j}^{dim(\Lambda)} c_j^{\Lambda} \, |\Phi_j^{\Lambda}\rangle \ . \tag{2.8.2}$$

We use the notation Ψ^{Λ} for the function consisting of the MR function and one of the correcting PCFs Λ

$$|\Psi^{\Lambda}(\gamma LS^{\pi})\rangle = \sum_{j=1}^{m} a_j^{\Lambda} \, |\Phi_i^{\mathrm{MR}}(\gamma_j LS^{\pi})\rangle + \sum_{j}^{dim(\Lambda)} c_j^{\Lambda} \, |\Phi_j^{\Lambda}\rangle \ . \tag{2.8.3}$$

In the PCFI approach, this function is obtained by solving the corresponding MCHF equations to optimize the Λ-PCF orbital set and mixing coefficients. Such a calculation that optimizes the MR eigenvector composition $\{a_j^{\Lambda}\}$ with orbitals frozen to the MR-MCHF solution, the mixing coefficients $\{c_j^{\Lambda}\}$ and the Λ-PCF radial functions, will be referred to as a MR-PCF calculation.

Assuming the CSFs of the MR and CF spaces to be orthonormal and

$\langle\Psi^\Lambda|\Psi^\Lambda\rangle = 1$, we have

$$\langle\Psi^\Lambda|\Psi^\Lambda\rangle = \langle\Psi^{\rm MR}|\Psi^{\rm MR}\rangle + \langle\Lambda|\Lambda\rangle = \sum_{j=1}^{m}(a_j^\Lambda)^2 + \sum_{j}^{dim(\Lambda)}(c_j^\Lambda)^2 = 1\,,$$

revealing that $\langle\Lambda|\Lambda\rangle \neq 1$. To keep a natural interpretation of the PCF weights, we renormalize each PCF according to

$$\overline{\Lambda} = \frac{1}{\sqrt{\sum_j (c_j^\Lambda)^2}}\,\Lambda\,.$$

The PCFI approach consists in regrouping the m components of the MR space and the p CF subspaces in an *a priori* low-dimension interaction matrix to get a compact representation of the total wave function

$$|\Psi\rangle = \sum_{i=1}^{m} a_i|\Phi_i^{\rm MR}\rangle + \sum_{j}^{p} b_j|\overline{\Lambda}_j\rangle\,, \tag{2.8.4}$$

where the mixing coefficients $\{a_i\}$ and $\{b_j\}$ are obtained by solving the generalized eigenvalue problem of dimension $(M = m + p)$

$$\mathbf{Hc} = E\,\mathbf{Sc}\,. \tag{2.8.5}$$

The corresponding Hamiltonian matrix may be explicitly written as

$$\mathbf{H} = \begin{pmatrix} \boxed{\begin{matrix}\langle\Phi_1^{\rm MR}|H|\Phi_1^{\rm MR}\rangle & \cdots & \langle\Phi_1^{\rm MR}|H|\Phi_m^{\rm MR}\rangle \\ \vdots & \ddots & \vdots \\ \langle\Phi_m^{\rm MR}|H|\Phi_1^{\rm MR}\rangle & \cdots & \langle\Phi_m^{\rm MR}|H|\Phi_m^{\rm MR}\rangle\end{matrix}} & & \boxed{\begin{matrix}\langle\Phi_1^{\rm MR}|H|\overline{\Lambda}_1\rangle \\ \vdots \\ \langle\Phi_m^{\rm MR}|H|\overline{\Lambda}_1\rangle\end{matrix}} & \cdots & \boxed{\begin{matrix}\langle\Phi_1^{\rm MR}|H|\overline{\Lambda}_p\rangle \\ \vdots \\ \langle\Phi_m^{\rm MR}|H|\overline{\Lambda}_p\rangle\end{matrix}} \\ & & \boxed{\langle\overline{\Lambda}_1|H|\overline{\Lambda}_1\rangle} & \cdots & \boxed{\langle\overline{\Lambda}_1|H|\overline{\Lambda}_p\rangle} \\ & \vdots & \vdots & \ddots & \vdots \\ & & \vdots & \cdots & \boxed{\langle\overline{\Lambda}_p|H|\overline{\Lambda}_p\rangle} \end{pmatrix} \tag{2.8.6}$$

The matrix dimension M is simply given by the sum of the number of CSFs belonging to the MR (m) and the number of PCF functions (p). The overlap matrix has the same structure, with a value of unity on the diagonal thanks to the renormalization ($|\Lambda_i\rangle \rightarrow |\overline{\Lambda}_i\rangle$). It can be obtained by merely substituting the H

operator, appearing in each matrix element, by the unit operator.

Some variational freedom in the coefficients is lost by the fact that solving (2.8.5) does not allow relaxation in the relative weights within each PCF. The latter are indeed fixed linear combinations,

$$|\overline{\Lambda}\rangle = \sum_k \overline{c}_k^{\Lambda} \, |\Phi_k\rangle \tag{2.8.7}$$

and as such, we will refer to $|\overline{\Lambda}\rangle$ as a *constrained* CSFs expansion in the sense that the orbitals and the expansion coefficients are not allowed to change. The coefficients $\{\overline{c}_k^{\Lambda}\}$ will be called the *constrained coefficients*. The effect associated with this loss of flexibility on a property, that we are investigating in the next section, will be qualified as the *constraint effect*.

2.8.1 Deconstraining Partitioned Correlation Functions

In the PCFI method, the expansion coefficients for the CSFs in the PCF are constrained (locked) so that there is no possibility of relative changes due to the interaction with other PCFs. To recover this variational freedom, the PCFs can be deconstrained by transferring h_j CSFs from the j-th PCF to the basis and at the same time setting their weights to zero, i.e. extending the space according to

$$\{\Phi_1^{\mathrm{MR}}, \ldots, \Phi_m^{\mathrm{MR}}\} \bigcup_{j=1}^{p} \{\overline{\Lambda}_j\} \longrightarrow \{\Phi_1^{\mathrm{MR}}, \ldots, \Phi_m^{\mathrm{MR}}\} \bigcup_{j=1}^{p} \{\Phi_1^j, \ldots, \Phi_{h_j}^j, \overline{\Lambda}_j^d\}. \tag{2.8.8}$$

The superscript d for the PCF $\overline{\Lambda}_j^d$ indicates a renormalized *de*-constrained Partitioned Correlation Function whose weights of the transferred CSFs have been set to zero. The many-electron wave function expansion becomes

$$\Psi = \sum_{i=1}^{m} c_i \Phi_i^{\mathrm{MR}} + \sum_{j=1}^{p} \left\{ \sum_{k=1}^{h_j} c_k^j \Phi_k^j + c_j \overline{\Lambda}_j^d \right\}, \tag{2.8.9}$$

where the expansion coefficients are obtained from a higher dimension ($M = m + \sum_{j=1}^{p}(h_j + 1)$) *a priori* generalized eigenvalue problem. The size of each block in (2.8.6) involving at least one PCF is growing accordingly to the number of deconstrained CSFs. In the limit of the completely deconstrained case (ie. $h_j = dim(\overline{\Lambda}_j) \;\; \forall j$), we regain full variational freedom in the coefficients, with the advantage that each CSF brings its tailored orbital basis. M is then at his

maximum value, ie. the total number of CSFs, and the wave function (2.8.9) will be referred as being "deconstrained". It is strictly equivalent to a configuration interaction problem in the CSF space built on various mutually non-orthonormal orbital sets.

For solving the eigenvalue problem (2.8.5) and for building efficiently the interaction matrices associated to the selected operators in the basis of CSFs and deconstrained PCFs spanning the wave function (2.8.9), we modify the original way of presenting the biorthonormal transformation [19] to evaluate $O_{ij} = \langle \Lambda_i | O | \Lambda_j \rangle$, where O is the Hamilton or unit operator. Following the original formalism, we perform a biorthonormal transformation

$$\langle \phi_k^i | \phi_m^j \rangle = S_{km}^{ij} \rightarrow \langle \tilde{\phi}_k^i | \tilde{\phi}_m^j \rangle = \delta_{n_k,n_m} \delta_{l_k,l_m}$$

to express the original left and right hand side PCFs in the new CSF bases $\{\tilde{\Phi}_k^i\}$ and $\{\tilde{\Phi}_l^j\}$

$$|\Lambda_i\rangle = \sum_{k=1}^{n_i} d_k^i |\Phi_k^i\rangle = \sum_{k=1}^{n_i} \tilde{d}_k^i |\tilde{\Phi}_k^i\rangle \tag{2.8.10}$$

$$|\Lambda_j\rangle = \sum_{l=1}^{n_j} d_l^j |\Phi_l^j\rangle = \sum_{l=1}^{n_j} \tilde{d}_l^j |\tilde{\Phi}_l^j\rangle \ , \tag{2.8.11}$$

where the counter-transformed eigenvectors $\{\tilde{d}_k^i\}$ and $\{\tilde{d}_l^j\}$ ensure the invariance of the total wave functions. Giving the matrix representation $\tilde{\mathbf{O}}$ of an operator O

$$\tilde{O}_{kl} = \langle \tilde{\Phi}_k^i | O | \tilde{\Phi}_l^j \rangle \ , \tag{2.8.12}$$

the matrix element between these PCFs is written as

$$\langle \Lambda_i | O | \Lambda_j \rangle = \sum_{k,l} (\tilde{d}_k^i)^* \tilde{d}_l^j \langle \tilde{\Phi}_k^i | O | \tilde{\Phi}_l^j \rangle = (\ \tilde{\mathbf{d}}^i)^t \ \tilde{\mathbf{O}} \ \tilde{\mathbf{d}}^j \tag{2.8.13}$$

where $\tilde{\mathbf{d}}$ is the column vector of counter-transformed mixing coefficients. Note that each CSF expansion should be *closed under de-excitation* (CUD) for allowing the biothonormal transformation [128, 19]. By strictly following this methodology, we may think that we should apply one biorthonormal transformation for each matrix element associated to any off-diagonal sub-matrix block involving two non-orthogonal orbital sets.

Using this strategy, relaxing the PCFI constraint to any degree becomes possi-

ble. The price to pay is the increase of the size of the Partition Correlation Function Interaction problem (2.8.5). In the limit of the completely deconstrained case (ie. $h_j = dim(\overline{\Lambda}_j) \ \forall j$) , the PCFI approach is strictly equivalent to a configuration interaction problem in the original complete CSF space. It is used the label DPCFI for this "deconstrained" approach. Since each CSF could be built, if worthwhile, on its own orbital basis, without any radial orthogonality constraints with the other ones, this DPCFI approach is strictly equivalent to a general configuration interaction problem in non-orthogonal orbitals.
The (D)PCFI procedure can be summarized as follows:

1. Perform a HF/MCHF calculation for the single-/multi-reference wave function,

2. Freeze the orbitals belonging to this MR space and perform p separate MR-PCF MCHF calculations for the different Partitioned Correlation Functions,

3. (Optional) Deconstrain each PCF by transferring the desired CSFs from the CF to the MR basis,

4. Build the Hamiltonian and other relevant operators interaction matrices by performing the biorthonormal transformations, if necessary, using the weight matrix formalism,

5. Solve the eigenvalue problem for getting the many-electron wave function,

6. Compute the desired property with the PCFI eigenvector(s).

Chapter 3

Energies and transition rates for isoelectronic sequences [A1-A4]

Spectroscopic data of boron-, carbon-, nitrogen, and oxygen-like ions are highly useful in the diagnostics of solar, astrophysical, and fusion plasmas [42] – [44]. For many years researchers have studied these isoelectronic sequences, providing both experimental and theoretical energy levels and transitions rates. In the sections below a review of the research for these sequences are given.

We present accurate and comprehensive calculations using the fully relativistic MCDHF and RCI methods. All calculations were performed with the GRASP2K code [25, 26]. For the calculations of spin-angular parts of matrix elements the second quantization method in coupled tensorial form and quasispin technique were adopted. For the calculations of transition data the biorthogonal orbital method was used. We give energies, transition rates of electric dipole (E1), magnetic dipole (M1), electric quadrupole (E2), magnetic quadrupole (M2), and lifetimes for states of the $(1s^2)\ 2s^2 2p^N$, $2s2p^{N+1}$, and $2p^{N+2}$ configurations, where $N = 1,\ 2,\ 3,\ 4$ are respectively for the B-, C-, N-, and O-like ions. The accuracy of the present data is assessed, and energy levels and rates for selected transitions are compared with previously reported values. The excellent description of the energy separations along the sequence makes it possible to crosscheck experimental energies for a number of ions. The calculations are also helpful in analyzing new data from electron-beam ion traps (EBITs), fusion plasmas, and astrophysical sources.

3.1 Generation of configuration expansions and calculation method

In the present calculations of the above-mentioned sequences, wave functions for all states belonging to a specific configuration were determined simultane-

ously in an extended optimal level (EOL) calculation [45]. The configuration expansions were obtained using the active set (AS) method [46]. Here CSFs of a specified parity and J symmetry are generated by excitations from a number of reference configurations to a set of relativistic orbitals. By applying restrictions on the allowed excitations, different electron correlation effects can be targeted. For energies and transition rates, valence and core-valence correlation effects are by far the most important. However, core-core effects also come into play at the highest level of accuracy [47]. In the present work valence, core-valence, and core-core correlation effects were included. To monitor the convergence of the calculated energies and transition parameters, the active sets were increased in a systematic way by adding layers of correlation orbitals. The configuration expansions were obtained by single and double (SD)-excitations to active sets with principal (n) and orbital (l) quantum numbers, that are given in Table 3.1.1 from all shells of the $(1s^2)\ 2s^2 2p^N$, $2s2p^{N+1}$, and $2p^{N+2}$ configurations. For the oxygen isoelectronic sequence were the restriction that there should be only a single excitation from the $1s$ shell.

Table 3.1.1: Size of configuration expansions.

	n and l	enlarged MR set
B-like	$n = 3\ldots9$	$\{2s^22p,\ 2p^3,\ 2s2p3d,\ 2p3d^2\}$ for odd states
	$l = 0\ldots5$	$\{2s2p^2,\ 2p^23d,\ 2s^23d,\ 2s3d^2\}$ for even states
	(for $n = 7$ the $l = 0\ldots6$)	
	(for $n = 9$ the $l = 0\ldots4$)	
C-like	$n = 3\ldots8$	$\{2s2p^3,\ 2p^33d,\ 2s^22p3d,\ 2s2p3d^2\}$ for odd states
	$l = 0\ldots5$	$\{2s^22p^2,\ 2p^4,\ 2s2p^23d,\ 2s^23d^2\}$ for even states
	(for $n = 8$ the $l = 0\ldots4$)	
N-like	$n = 3\ldots8$	$\{2s^22p^3,\ 2p^5,\ 2s2p^33d,\ 2s^22p3d^2\}$ for odd states
	$l = 0\ldots4$	$\{2s2p^4,\ 2p^43d,\ 2s^22p^23d,\ 2s2p^23d^2\}$ for even states
	(for $n = 6$ the $l = 0\ldots5$)	
O-like	$n = 3\ldots8$	$\{2s2p^5,\ 2p^53d,\ 2s^22p^33d\}$ for odd states
	$l = 0\ldots5$	$\{2s^22p^4,\ 2p^6,\ 2s2p^43d\}$ for even states

The self-consistent field calculations for each layer of orbitals were followed by RCI calculations, including the Breit interaction. At the final stage the multireference set was enlarged to contain all CSFs with the larger weights in the CSF calculation. Particularly important were some configurations with $3d$ orbitals. The enlarged multireference sets are given in Table 3.1.1 for even and

Table 3.1.2: Summary of the extended optimal level MCDHF calculations performed indicating the range of eigenvalues and the size of the interaction matrix for each configuration.

Configuration	J	Parity	Eigenvalues	Size
		B-like		
$1s^2 2s^2 2p$	1/2, 3/2	–	1,1	202 297
$1s^2 2s 2p^2$	1/2, 3/2, 5/2	+	1-3,1-3,1-2	302 420
$1s^2 2p^3$	1/2, 3/2, 5/2	–	2,2-4,1	363 181
		C-like		
$1s^2 2s^2 2p^2$	0, 1, 2	+	1-2,1,1-2	341 948
$1s^2 2s 2p^3$	0, 1, 2, 3	–	1,1-4,1-4,1	946 241
$1s^2 2p^4$	0, 1, 2	+	3-4,1-2,3-4	341 948
		N-like		
$1s^2 2s^2 2p^3$	1/2, 3/2, 5/2	–	1,1-3,1	698 631
$1s^2 2s 2p^4$	1/2, 3/2, 5/2	+	1-3,1-3,1-2	679 954
$1s^2 2p^5$	1/2, 3/2	–	2,4	382 541
		O-like		
$1s^2 2s^2 2p^4$	0, 1, 2	+	1-2,1,1-2	709 690
$1s^2 2s 2p^5$	0, 1, 2	–	1,1-2,1	702 892
$1s^2 2p^6$	0	+	3	67 375

odd states of each isoelectronic sequence. Among the states generated by SD-excitations from the multireference set only those interacting with the multireference states were kept, and the jj reduction technique [25] was applied. In Table 3.1.2 are given final expansion for the states of even and odd configurations distributed over the J symmetry blocks for each isoelectronic sequences. By increasing the multireference set some higher order correlation effects were captured. These higher order effects were important both for improving the energy separations further as well as for bringing the transition rates in the length and velocity form in close agreement [48]. The leading quantum electrodynamic (QED) effects - vacuum polarization and self-energy - were included in the final multireference RCI calculations.

3.2 B-like ions

Theoretically predicted energy levels and oscillator strengths are available from a number of sources [49] – [56]. Froese Fischer and Tachiev have presented energy levels and rates for electric dipole transitions in boron-like ions between B I and Si IX for low lying excited states based on calculations using multiconfiguration Hartree-Fock Breit-Pauli (MCHF-BP) wave functions [52, 53]. Froese Fischer

also presented energy levels, transition rates and lifetimes of boron-like ions using the multiconfiguration Dirac-Hartree-Fock method [54]. Koc calculated energy levels and transitions rates based on the multireference relativistic configuration interaction (MR RCI) method with the no-pair Dirac-Coulomb-Breit Hamiltonian [55, 56, 57]. Corrégé and Hibbert have presented energy levels, oscillator strengths and transitions probabilities for C II, N III and O IV using the code CIV3 [58]. Merkelis et al. used the stationary second-order many-body perturbation theory (MBPT) to compute energies for n = 2 levels and transition rates form boron-like ions for Z = 8 to 26 [59]. Jonauskas et al. [43] used multiconfiguration Dirac-Fock (MCDF) to calculate energies of the 407 lowest levels in Fe XXII and transition probabilities, oscillator and line strengths for E1, E2, M1 transitions. Bogdanovich et al. presented energy spectra and the radiative lifetimes of the levels of configurations $2s^2 2p$, $2s2p^2$, $2p^3$ and $2s^2 3l$ with Z = 7 to 45 using the configuration interaction method [60]. Jönsson et al. presented energy levels, specific mass shift parameters, hyperfine interaction constants, and transition probabilities for C II, N III, and O IV using MCDHF method [61, 62]. Hao and Jiang calculated energy levels, transition rates, and line strengths for several ions along the B I isoelectronic sequence also using MCDHF method [63].

3.2.1 Results and evaluation of data

A full set of energies, E1, M1, E2, M2 transition rates, line strengths, oscillator strengths, and lifetimes for the states of the $(1s^2)2s^2 2p, 2s2p^2$, and $2p^3$ configurations in all boron-like ions between N III and Zn XXVI are reported in the paper [A1]. In the thesis just some of these results are described.

Table 3.2.1 shows the energy levels for Si X from RCI calculations including the Breit interaction and leading QED effects, with configuration expansions obtained by SD-excitations from the $\{2s^2 2p,\ 2p^3\}$ and $\{2s2p^2\}$ references to increasing active sets of orbitals $n = 3 \ldots 9$. The column denoted MR displays energies from RCI calculations with configuration expansions obtained by SD-excitations from the enlarged $\{2s^2 2p,\ 2p^3,\ 2s2p3d,\ 2p3d^2\}$ and $\{2s2p^2,\ 2p^2 3d,\ 2s^2 3d,\ 2s3d^2\}$ multireferences to the $n = 9$ active set of orbitals. The energies seem to be rather well converged with respect to the active set of orbitals with energy changes of some 10 cm^{-1} to 30 cm^{-1} when going from $n = 8$ to $n = 9$. The effects of the increasing multireferences are slightly larger.

Table 3.2.1: Convergence of energy levels in Si X. Energy levels are given in (cm^{-1}).

Level	J	$n=3$	$n=4$	$n=5$	$n=6$	$n=7$	$n=8$	$n=9$	MR	Obs. [64]
$2s^2 2p\ ^2P^o$	1/2	0	0	0	0	0	0	0	0	0
	3/2	6 982	6 995	6 995	7 001	7 000	6 999	6 999	7 000	6 991
$2s2p^2\ ^4P$	1/2	159 247	160 052	160 333	160 775	160 821	160 902	160 929	160 953	161 010
	3/2	161 713	162 528	162 811	163 253	163 299	163 381	163 408	163 431	163 490
	5/2	165 267	166 092	166 378	166 818	166 864	166 946	166 973	166 997	167 060
$2s2p^2\ ^2D$	3/2	290 189	288 447	288 128	288 134	288 027	288 023	288 020	287 997	287 850
	5/2	290 194	288 463	288 144	288 152	288 045	288 041	288 038	288 011	287 880
$2s2p^2\ ^2S$	1/2	372 928	369 525	368 788	368 209	368 009	367 960	367 929	367 943	367 670
$2s2p^2\ ^2P$	1/2	393 839	391 379	390 834	390 550	390 400	390 362	390 349	390 289	390 040
	3/2	397 751	395 333	394 798	394 526	394 377	394 340	394 328	394 266	394 030
$2p^3\ ^4S^o$	3/2	508 713	508 691	508 701	509 185	509 219	509 310	509 313	509 332	509 330
$2p^3\ ^2D^o$	3/2	578 470	576 134	575 651	575 720	575 627	575 649	575 637	575 593	575 430
	5/2	578 479	576 172	575 694	575 770	575 679	575 701	575 690	575 621	575 450
$2p^3\ ^2P^o$	1/2	652 480	648 412	647 617	647 326	647 156	647 096	647 076	647 032	646 760
	3/2	653 087	649 035	648 239	647 950	647 780	647 721	647 701	647 660	647 390

Table 3.2.2: Energy levels for N III, Ar XIV, and Co XXIII. Energy levels are given in (cm^{-1}).

Level	J	Level (cm^{-1})			Splitting (cm^{-1})		
		Calc.	Obs. [64]	Diff.	Calc.	Obs. [64]	Diff.
				N III			
$2s^2 2p\ ^2P^o$	1/2	0	0	0			
	3/2	176.5	174.4	2.1	176.5	174.4	2.1
$2s2p^2\ ^4P$	1/2	57 097.6	57 187.1	−89.5			
	3/2	57 157.7	57 246.8	−89.1	60.1	59.7	0.4
	5/2	57 239.6	57 327.9	−88.3	142.0	140.8	1.2
$2s2p^2\ ^2D$	5/2	101 117.1	101 023.9	93.2			
	3/2	101 124.5	101 030.6	93.9	7.4	6.7	0.7
$2s2p^2\ ^2S$	1/2	131 378.0	131 004.3	373.7			
$2s2p^2\ ^2P$	1/2	146 034.4	145 875.7	158.7			
	3/2	146 145.5	145 985.8	159.7	111.1	110.1	1.0
$2p^3\ ^4S^o$	3/2	186 756.3	186 797.1	−40.8			
$2p^3\ ^2D^o$	5/2	203 171.4	203 074.6	96.8			
	3/2	203 185.6	203 088.9	96.7	14.2	14.3	−0.1
$2p^3\ ^2P^o$	1/2	230 811.4	230 404.3	407.1			
	3/2	230 811.4	230 408.6	402.8	0.0	4.3	−4.3
				Ar XIV			
$2s^2 2p\ ^2P^o$	1/2	0	0	0			
	3/2	22 668	22 658	10	22 668	22 658	10
$2s2p^2\ ^4P$	1/2	229 351	230 270	−919			
	3/2	237 939	238 950	−1 011	8 588	8 680	−92
	5/2	249 426	250 420	−994	20 075	20 150	−75
$2s2p^2\ ^2D$	3/2	410 312	410 200	112			
	5/2	411 272	411 210	62	960	1 010	−50
$2s2p^2\ ^2S$	1/2	514 675	514 420	255			
$2s2p^2\ ^2P$	1/2	545 434	545 250	184			
	3/2	554 954	554 680	274	9 520	9 430	90
$2p^3\ ^4S^o$	3/2	718 046	718 900	−854			
$2p^3\ ^2D^o$	3/2	811 122	810 200	922			
	5/2	813 022	812 800	222	1 900	2 600	−700
$2p^3\ ^2P^o$	1/2	908 929	908 700	229			
	3/2	913 247	913 000	247	4 318	4 300	18
				Co XXIII			
$2s^2 2p\ ^2P^o$	1/2	0	0	0			
	3/2	139 712	139 290	422	139 712	139 290	422
$2s2p^2\ ^4P$	1/2	430 472	431 560	−1 088			
	3/2	498 309	499 270	−961	67 837	67 710	127
	5/2	559 266	559 760	−494	128 794	128 200	594
$2s2p^2\ ^2D$	3/2	788 546	788 520	26			
	5/2	819 221	819 150	71	30 675	30 630	45
$2s2p^2\ ^2P$	1/2	903 830	903 260	570			
	3/2	1 065 389	1 064 960	429	161 559	161 700	−141
$2s2p^2\ ^2S$	1/2	1 051 638	1 050 860	778			
$2p^3\ ^4S^o$	3/2	1 337 944	1 338 760	−816			
$2p^3\ ^2D^o$	3/2	1 486 134	1 486 350	−216			
	5/2	1 523 263	1 523 150	113	37 129	36 800	329
$2p^3\ ^2P^o$	1/2	1 672 634	1 672 130	504			
	3/2	1 746 108	1 745 870	238	73 474	73 740	−266

Table 3.2.2 displays the experimental energy levels and the computed energies from the largest RCI calculations including the Breit interaction and QED corrections. The computed energies agree very well with the experimental values. Energy differences are in most cases around a few hundred cm^{-1}. There are exception for Ar XIV and Co XXIII for states $2s2p^2\ ^4P_{1/2,\ 3/2,\ 5/2}$ and $2p^3\ ^4S^o_{3/2}$, which are of the order 1000 cm^{-1} too low. We attribute these differences to uncertainties in the experimental values. Also the fine-structure separations are well described with the exception of $2p^3\ ^2D_{3/2,\ 5/2}$ in Ar XIV. Again we believe that the problem with the latter structure lies on the experimental side. Our calculated energy levels are in good agreement with Koc [55, 57] energies values.

In Table 3.2.3 we compare E1 transition rates for O IV with rates taken from MR RCI [55, 57], MCHF [54], CIV3 [58] calculations and values taken from NIST [64]. In this table we give rates in the length gauge and ratio R between the transition rates in length and velocity gauges. A value close to $R = 1$ for an allowed transition is a known indicator of accuracy [23]. The ratio R is often close to 1 for the strong allowed transitions, but not for all weak spin-forbidden transitions. As is seen in Table 3.2.3 transitions rates are in good agreement with other methods.

Table 3.2.3: Comparison of E1 transitions rates for O IV. Transition rates (A) are given in (s^{-1}).

Levels		This work					
Upper	Lower	A_{RCI}	R	$A_{\mathrm{MR\ RCI}}$ [55, 57]	A_{MCHF} [54]	A_{CIV3} [58]	A_{NIST} [64]
$2s2p^2\ ^4P_{1/2}$	$2s^22p\ ^2P^o_{1/2}$	1.464e+03	0.69		1.493e+03	1.474e+03	
$2s2p^2\ ^4P_{3/2}$	$2s^22p\ ^2P^o_{1/2}$	4.072e+01	1.03		3.908e+01	3.747e+01	
$2s2p^2\ ^2D_{3/2}$	$2s^22p\ ^2P^o_{1/2}$	6.020e+08	1.00	6.01e+08	6.026e+08	5.978e+08	5.95e+08
$2s2p^2\ ^2S_{1/2}$	$2s^22p\ ^2P^o_{1/2}$	1.246e+09	1.01	1.25e+09	1.256e+09	1.251e+09	1.21e+09
$2s2p^2\ ^2P_{1/2}$	$2s^22p\ ^2P^o_{1/2}$	4.764e+09	1.00	4.77e+09	4.768e+09	4.750e+09	4.86e+09
$2s2p^2\ ^2P_{3/2}$	$2s^22p\ ^2P^o_{1/2}$	1.206e+09	1.00	1.21e+09	1.207e+09	1.202e+09	1.22e+09
$2s2p^2\ ^4P_{1/2}$	$2s^22p\ ^2P^o_{3/2}$	1.438e+03	0.71		1.466e+03	1.448e+03	
$2s2p^2\ ^4P_{3/2}$	$2s^22p\ ^2P^o_{3/2}$	2.847e+02	0.51		2.944e+02	2.895e+02	
$2s2p^2\ ^4P_{5/2}$	$2s^22p\ ^2P^o_{3/2}$	1.195e+03	0.68		1.194e+03	1.163e+03	
$2s2p^2\ ^2D_{5/2}$	$2s^22p\ ^2P^o_{3/2}$	7.106e+08	0.99	7.09e+08	7.114e+08	7.056e+08	7.08e+08
$2s2p^2\ ^2D_{3/2}$	$2s^22p\ ^2P^o_{3/2}$	1.156e+08	1.00	1.15e+08	1.156e+08	1.148e+08	1.18e+08
$2s2p^2\ ^2S_{1/2}$	$2s^22p\ ^2P^o_{3/2}$	2.310e+09	1.01	2.32e+09	2.329e+09	2.324e+09	2.40e+09
$2s2p^2\ ^2P_{1/2}$	$2s^22p\ ^2P^o_{3/2}$	2.474e+09	1.00	2.47e+09	2.477e+09	2.464e+09	2.41e+09
$2s2p^2\ ^2P_{3/2}$	$2s^22p\ ^2P^o_{3/2}$	6.040e+09	1.00	6.04e+09	6.043e+09	6.019e+09	6.06e+09
$2p^3\ ^4S^o_{3/2}$	$2s2p^2\ ^4P_{1/2}$	1.059e+09	1.00	1.06e+09	1.060e+09	1.059e+09	1.07e+09
$2p^3\ ^2D^o_{3/2}$	$2s2p^2\ ^4P_{1/2}$	7.256e+02	1.34		5.332e+02	5.112e+02	
$2p^3\ ^2P^o_{1/2}$	$2s2p^2\ ^4P_{1/2}$	1.605e+04	1.12		1.546e+04	1.170e+04	

Continued...

Table 3.2.3: (continued)

Levels		This work					
Upper	Lower	A_{RCI}	R	$A_{\mathrm{MR\ RCI}}$ [55, 57]	A_{MCHF} [54]	A_{CIV3} [58]	A_{NIST} [64]
$2p^3\ ^2P^o_{3/2}$	$2s2p^2\ ^4P_{1/2}$	7.220e+02	0.76		1.186e+03	1.806e+03	
$2p^3\ ^4S^o_{3/2}$	$2s2p^2\ ^4P_{3/2}$	2.112e+09	1.00	2.11e+09	2.115e+09	2.113e+09	2.13e+09
$2p^3\ ^2D^o_{5/2}$	$2s2p^2\ ^4P_{3/2}$	1.471e+03	1.43		1.110e+03	1.080e+03	
$2p^3\ ^2D^o_{3/2}$	$2s2p^2\ ^4P_{3/2}$	1.677e+04	1.14		1.457e+04	1.425e+04	
$2p^3\ ^2P^o_{1/2}$	$2s2p^2\ ^4P_{3/2}$	2.985e+03	1.03		3.716e+03	2.874e+03	
$2p^3\ ^2P^o_{3/2}$	$2s2p^2\ ^4P_{3/2}$	4.353e+04	1.05		4.553e+04	4.113e+04	
$2p^3\ ^4S^o_{3/2}$	$2s2p^2\ ^4P_{5/2}$	3.155e+09	1.00	3.15e+09	3.161e+09	3.158e+09	3.19e+09
$2p^3\ ^2D^o_{5/2}$	$2s2p^2\ ^4P_{5/2}$	5.560e+04	1.13		4.887e+04	4.771e+04	
$2p^3\ ^2D^o_{3/2}$	$2s2p^2\ ^4P_{5/2}$	3.098e+03	1.23		2.676e+03	2.583e+03	
$2p^3\ ^2P^o_{3/2}$	$2s2p^2\ ^4P_{5/2}$	1.601e+04	1.11		1.421e+04	1.473e+04	
$2p^3\ ^4S^o_{3/2}$	$2s2p^2\ ^2D_{5/2}$	3.311e+02	1.11		2.544e+02	3.620e+02	
$2p^3\ ^2D^o_{5/2}$	$2s2p^2\ ^2D_{5/2}$	1.355e+09	1.00	1.35e+09	1.353e+09	1.354e+09	1.36e+09
$2p^3\ ^2D^o_{3/2}$	$2s2p^2\ ^2D_{5/2}$	1.522e+08	1.00	1.52e+08	1.521e+08	1.521e+08	1.46e+08
$2p^3\ ^2P^o_{3/2}$	$2s2p^2\ ^2D_{5/2}$	2.544e+09	1.01	2.55e+09	2.561e+09	2.557e+09	2.60e+09
$2p^3\ ^4S^o_{3/2}$	$2s2p^2\ ^2D_{3/2}$	7.391e−02	0.16		3.476e−04		
$2p^3\ ^2D^o_{5/2}$	$2s2p^2\ ^2D_{3/2}$	9.919e+07	1.00	9.87e+07	9.898e+07	9.902e+07	9.70e+07
$2p^3\ ^2D^o_{3/2}$	$2s2p^2\ ^2D_{3/2}$	1.296e+09	1.00	1.29e+09	1.294e+09	1.295e+09	1.31e+09
$2p^3\ ^2P^o_{1/2}$	$2s2p^2\ ^2D_{3/2}$	2.855e+09	1.01	2.87e+09	2.875e+09	2.870e+09	2.89e+09
$2p^3\ ^2P^o_{3/2}$	$2s2p^2\ ^2D_{3/2}$	2.920e+08	1.01	2.93e+08	2.940e+08	2.934e+08	2.89e+08
$2p^3\ ^4S^o_{3/2}$	$2s2p^2\ ^2S_{1/2}$	3.104e+01	0.90		2.855e+01	3.185e+01	
$2p^3\ ^2P^o_{1/2}$	$2s2p^2\ ^2S_{1/2}$	3.904e+08	0.99	3.85e+08	3.861e+08	3.862e+08	4.05e+08
$2p^3\ ^2P^o_{3/2}$	$2s2p^2\ ^2S_{1/2}$	4.201e+08	0.99	4.13e+08	4.156e+08	4.151e+08	4.05e+08
$2p^3\ ^4S^o_{3/2}$	$2s2p^2\ ^2P_{1/2}$	3.872e+02	0.79		3.192e+02	3.894e+02	
$2p^3\ ^2D^o_{3/2}$	$2s2p^2\ ^2P_{1/2}$	2.182e+08	0.99	2.17e+08	2.193e+08	2.194e+08	2.17e+08
$2p^3\ ^2P^o_{1/2}$	$2s2p^2\ ^2P_{1/2}$	8.896e+08	1.00	8.87e+08	8.953e+08	8.931e+08	8.83e+08
$2p^3\ ^2P^o_{3/2}$	$2s2p^2\ ^2P_{1/2}$	2.066e+08	1.00	2.06e+08	2.080e+08	2.078e+08	2.21e+08
$2p^3\ ^4S^o_{3/2}$	$2s2p^2\ ^2P_{3/2}$	1.439e+03	0.76		1.193e+03	1.455e+03	
$2p^3\ ^2D^o_{5/2}$	$2s2p^2\ ^2P_{3/2}$	2.561e+08	0.99	2.55e+08	2.574e+08	2.575e+08	2.57e+08
$2p^3\ ^2D^o_{3/2}$	$2s2p^2\ ^2P_{3/2}$	4.145e+07	1.00	4.12e+07	4.165e+07	4.166e+07	4.29e+07
$2p^3\ ^2P^o_{1/2}$	$2s2p^2\ ^2P_{3/2}$	4.316e+08	1.00	4.31e+08	4.343e+08	4.334e+08	4.39e+08
$2p^3\ ^2P^o_{3/2}$	$2s2p^2\ ^2P_{3/2}$	1.097e+09	1.00	1.09e+09	1.104e+09	1.102e+09	1.10e+09

Table 3.2.4 displays E2, M1 rates in the length gauge from present calculations. For the electric quadrupole transitions, the ratio R between the transition rates in length and velocity gauges is given. The rates are compared with rates from other calculations and with experimental values.

In Table 3.2.5 lifetimes of all the levels of the $2s^22p$, $2s2p^2$ and $2p^3$ configurations are displayed for N III and Si X. Lifetimes are compared with other MCHF and MCDHF calculations by Froese Fischer [54] and, when available,

Table 3.2.4: Comparison of M1 and E2 transitions rates for Ne VI, Ca XVI, Zn XXVI. Transition rates (A) are given in (s^{-1}).

Levels		Type	This work		$A_{\text{MR RCI}}$ [55, 57]	A_{MCDHF} [54]	A_{NIST} [64]
Upper	Lower		A_{RCI}	R			
			Ne VI				
$2s^2 2p\ ^2P^o_{3/2}$	$2s^2 2p\ ^2P^o_{1/2}$	M1	2.028e−02		2.05e−02	2.089e−02	2.02e−02
$2s^2 2p\ ^2P^o_{3/2}$	$2s^2 2p\ ^2P^o_{1/2}$	E2	2.216e−08	0.82	2.45e−08	2.321e−08	
			P XI				
$2s^2 2p\ ^2P^o_{3/2}$	$2s^2 2p\ ^2P^o_{1/2}$	M1	8.232e+00		8.16e+00	8.237e+00	8.19e+00
$2s^2 2p\ ^2P^o_{3/2}$	$2s^2 2p\ ^2P^o_{1/2}$	E2	6.362e−05	1.03	6.27e−05	6.394e−05	
			Ca XVI				
$2s^2 2p\ ^2P^o_{3/2}$	$2s^2 2p\ ^2P^o_{1/2}$	M1	4.408e+02		4.39e+02	4.414e+02	
$2s^2 2p\ ^2P^o_{3/2}$	$2s^2 2p\ ^2P^o_{1/2}$	E2	1.267e−02	1.02	1.26e−02	1.274e−02	
			Mn XXI				
$2s^2 2p\ ^2P^o_{3/2}$	$2s^2 2p\ ^2P^o_{1/2}$	M1	8.802e+03		8.76e+03	8.817e+03	8.80e+03
$2s^2 2p\ ^2P^o_{3/2}$	$2s^2 2p\ ^2P^o_{1/2}$	E2	6.835e−01	1.02	6.79e−01	6.873e−01	6.90e−01
			Zn XXVI				
$2s^2 2p\ ^2P^o_{3/2}$	$2s^2 2p\ ^2P^o_{1/2}$	M1	9.777e+04		9.74e+04	9.796e+04	
$2s^2 2p\ ^2P^o_{3/2}$	$2s^2 2p\ ^2P^o_{1/2}$	E2	1.695e+01	1.02	1.68e+01	1.704e+01	

with experimental measurements. Our theoretical lifetimes agree with measured lifetimes to within one to two times of the experimental error limits.

3.2.2 Summary

All results of energy levels, transition rates, line strengths, oscillator strengths and lifetimes for relativistic configuration interaction calculations for transitions among the $(1s^2)\ 2s^2 2p$, $2s 2p^2$, and $2p^3$ configurations of all boron-like ions from N III to Zn XXVI are reported in [A1]. The results for the energies, transition rates and lifetimes are compared with the earlier available values obtained from calculations in the Breit-Pauli approximation [52], in the relativistic configuration interaction method [55, 56], in the CIV3 method [58] and also with experimental measurements. Results from our present calculations are in very good agreement with other theoretical methods, as well as with experimental values. The present energy values generally agree within a few hundred cm^{-1} with the experimentally compiled results for all the studied ions. Transition rates agree very well with rates from other recent calculations.

Table 3.2.5: Lifetimes for N III, Si X. Lifetimes (τ) are given in (s).

Levels	τ_{RCI}	$\tau_{\mathrm{MCHF/MCDF}}$ [54]	τ_{exp}
		N III	[65]
$2s^2 2p\ ^2P^o_{3/2}$	2.023e+04	2.0747e+04	
$2s2p^2\ ^4P_{1/2}$	1.418e−03	1.3736e−03	
$2s2p^2\ ^4P_{3/2}$	1.424e−02	1.3691e−02	
$2s2p^2\ ^4P_{5/2}$	3.554e−03	3.5592e−03	
$2s2p^2\ ^2D_{5/2}$	1.996e−09	1.9959e−09	(2.09±0.08)e−09
$2s2p^2\ ^2D_{3/2}$	1.985e−09	1.9847e−09	(2.09±0.08)e−09
$2s2p^2\ ^2S_{1/2}$	3.642e−10	3.5839e−10	(3.2±0.6)e−10
$2s2p^2\ ^2P_{1/2}$	1.764e−10	1.7622e−10	(1.9±0.5)e−10
$2s2p^2\ ^2P_{3/2}$	1.763e−10	1.7616e−10	(2.0±0.6)e−10
$2p^3\ ^4S^o_{3/2}$	2.058e−10	2.2072e−10	(2.6±0.5)e−10
$2p^3\ ^2D^o_{5/2}$	8.786e−10	8.8405e−10	
$2p^3\ ^2D^o_{3/2}$	8.795e−10	8.8482e−10	
$2p^3\ ^2P^o_{1/2}$	2.987e−10	2.9310e−10	
$2p^3\ ^2P^o_{3/2}$	2.991e−10	2.9346e−10	
		Si X	[66]
$2s^2 2p\ ^2P^o_{3/2}$	3.245e−01	3.2431e−01	
$2s2p^2\ ^4P_{1/2}$	1.870e−06	1.9055e−06	
$2s2p^2\ ^4P_{3/2}$	1.389e−05	1.4098e−05	
$2s2p^2\ ^4P_{5/2}$	4.066e−06	4.1390e−06	
$2s2p^2\ ^2D_{3/2}$	4.550e−10	4.5452e−10	(4.9±0.3)e−10
$2s2p^2\ ^2D_{5/2}$	4.909e−10	4.9046e−10	(4.9±0.3)e−10
$2s2p^2\ ^2S_{1/2}$	1.087e−10	1.0864e−10	(1.0±0.08)e−10
$2s2p^2\ ^2P_{1/2}$	5.947e−11	5.9444e−11	(5.8±0.5)e−11
$2s2p^2\ ^2P_{3/2}$	5.816e−11	5.8128e−11	(5.8±0.5)e−11
$2p^3\ ^4S^o_{3/2}$	6.407e−11	6.3882e−11	(5.9±0.5)e−11
$2p^3\ ^2D^o_{3/2}$	1.825e−10	1.8168e−10	(1.75±0.1)e−10
$2p^3\ ^2D^o_{5/2}$	1.813e−10	1.8034e−10	(1.75±0.1)e−10
$2p^3\ ^2P^o_{1/2}$	7.645e−11	7.6155e−11	(7.8±0.5)e−11
$2p^3\ ^2P^o_{3/2}$	7.715e−11	7.6859e−11	(7.8±0.5)e−11

3.3 C-like ions

Fawcett has presented oscillator strengths and energy levels for allowed n=2–n=2 and n=2–n=3 transitions in carbon-like ions between F IV and Ni XXIII based on calculations using the Hartree-Fock-Relativistic (HFR) code of Cowan [67, 68]. Aggarwal *et. al* used the CIV3 code to obtain rates between low-lying states for a number of ions from F IV to Ar XIII [69] –[71]. Zhang and Sampson used the relativistic distorted wave method to obtain values for a large number of states [72, 73]. Froese Fischer and Tachiev calculated energy levels and transition rates for low-lying states for ions up to Al VIII using multiconfiguration Breit-Pauli wave functions [52]. More recently Jönsson and Bieroń used the RCI method to obtain energy levels, transition rates, hyperfine-structure parameters and Landé g_J factors for low lying states in N II, O III, F IV, Ne V, and Ti XVII [48].

3.3.1 Results and evaluation of data

A full set of energies, E1, M1, E2 transition rates, hyperfine-structure parameters and Landé g_J factors for states of the $(1s^2)2s^22p^2$, $2s2p^3$, and $2p^4$ configurations for carbon-like ions between F IV and Ni XXIII are presented in the paper [A2]. In this section we will present data for some ions and compare with other theoretical methods and with experiment.

Table 3.3.1 displays the experimental energy levels and the computed energies from the largest RCI calculations including QED corrections. The computed energies agree very well with the experimental values. Energy differences are in most cases around a few hundred cm^{-1}. The only exceptions are the $2s2p^3\ ^5S^o_2$ and $2p^4\ ^1S_0$ states, which sometimes are of the order 500 cm^{-1} too low and too high, respectively. Also the fine-structure separations are well described, although there are some difficulties to reproduce the fine-structure splittings in $2s2p^3\ ^3P^o$ for Na VI, Mg VII, and Al VIII, where the fine-structure is very small and highly irregular. The same difficulties to account for fine-structure separations in these ions are seen for calculations in the Breit-Pauli approximation [71, 52]. The fine-structure for $2s2p^3\ ^3P^o$ is strongly affected by the multireference set, and to improve the accuracy in the calculated values within the RCI scheme it would be desirable to increase the multireference set further. Overall, the present RCI calculations give much improved energy structures compared to other calculations, with a balanced description for all the studied states and ions.

Table 3.3.1: Energy levels for F IV, K XIV. Energy levels are given in (cm^{-1}).

Level	J	Level (cm^{-1})			Splitting (cm^{-1})		
		Calc.	Obs. [64]	Diff.	Calc.	Obs. [64]	Diff.
				F IV			
$2s^2 2p^2\ ^3P$	0	0	0	0			
	1	227.0	226.0	1.0	227.0	226.0	1.0
	2	613.4	614.0	−0.6	613.2	614.0	−0.6
$2s^2 2p^2\ ^1D$	2	25 371.9	25 238.2	133.7			
$2s^2 2p^2\ ^1S$	0	53 769.8	53 541.2	228.6			
$2s2p^3\ ^5S^o$	2	73 979.3	74 194.7	−215.4			
$2s2p^3\ ^3D^o$	3	147 917.2	147 843.0	74.2			
	2	147 963.9	147 888.7	75.2	46.7	45.7	1.0
	1	147 976.5	147 903.5	73.0	59.3	60.5	−1.2
$2s2p^3\ ^3P^o$	2	175 449.0	175 236.8	212.2			
	1	175 453.0	175 241.9	211.1	4.0	5.1	−1.1
	0	175 480.0	175 263.9	216.1	31.0	27.1	3.9
$2s2p^3\ ^1D^o$	2	229 210.5	228 903.8	306.7			
$2s2p^3\ ^3S^o$	1	238 512.8	238 296.7	216.1			
$2s2p^3\ ^1P^o$	1	257 916.0	257 386.5	529.5			
$2p^4\ ^3P$	2	348 608.5	348 327.4	281.1			
	1	349 049.7	348 766.6	283.1	441.2	439.2	2.0
	0	349 248.0	348 959.8	288.2	639.5	632.4	7.1
$2p^4\ ^1D$	2	367 779.1	367 402.6	376.5			
$2p^4\ ^1S$	0	422 818.2	422 030.0	788.2			
				K XIV			
$2s^2 2p^2\ ^3P$	0	0	0	0			
	1	13 242	13 235	7	13 242	13 235	7
	2	28 230	28 225	5	28 230	28 225	5
$2s^2 2p^2\ ^1D$	2	96 080	95 913	167			
$2s^2 2p^2\ ^1S$	0	179 161	178 914	247			
$2s2p^3\ ^5S^o$	2	250 521	250 640	−119			
$2s2p^3\ ^3D^o$	2	458 821	458 754	67			
	1	459 538	459 498	40	717	744	−27
	3	461 024	461 002	22	2 203	2 248	−45
$2s2p^3\ ^3P^o$	0	537 617	537 402	215			
	1	538 248	538 032	216	631	630	1
	2	540 144	539 938	206	2 527	2 536	−9
$2s2p^3\ ^1D^o$	2	676 864	676 460	404			
$2s2p^3\ ^3S^o$	1	678 037	677 710	327			
$2s2p^3\ ^1P^o$	1	755 567	755 050	517			
$2p^4\ ^3P$	2	1 030 329	1 030 090	239			
	1	1 050 818	1 050 620	198	20 489	20 530	−41
	0	1 056 343	1 056 200	143	26 014	26 110	−96
$2p^4\ ^1D$	2	1 109 135	1 108 800	335			
$2p^4\ ^1S$	0	1 255 446	1 254 810	636			

E1 transitions rates in length gauge for some ions of carbon sequence are given in Table 3.3.2. Also the ratio R between the transition rates in length and velocity gauges is given. A value close to $R = 1$ means that both gauges are in good agreement. To illustrate the level of agreement between different methods, calculated rates for some transitions along the sequence are displayed in Table 3.3.2. The agreement between the present values and the Breit-Pauli values by Froese Fischer and Tachiev [52] is very good, especially for strong transitions. The calculations by Aggarwal *et al.* [69] –[71] are comparatively small in terms of electron correlation effects included. Nevertheless, the general agreement between these calculations and the Breit-Pauli calculations by Froese Fischer and Tachiev as well as the present fully relativistic ones is satisfactory (see [48] for a more comprehensive assessment of the accuracy). The strongest transitions in the arrays have been calculated by Fawcett using the HFR code [67]. Although small, these calculations agree quite well with the present calculation for the high-Z end, where correlation effects are less important.

In Table 3.3.3 there is also rates for M1 and E2 transitions between the fine-structure levels of the $2s^2 2p^2$ configuration for Mg VII. Rates are based on computed transition energies. These transitions are comparatively weak. The strength of the M1 transitions, however, increases along the sequence to reach rates up to 10^5 s^{-1} for Ni XXIII. The M1 and E2 transitions have been considered in the work by Froese Fischer and Tachiev [52], and in Table 3.3.3 their values are compared with the present ones for Mg VII. As seen from the table there is a good agreement between the two sets of calculations.

The transition between the coupling schemes is illustrated in Table 3.3.4, where g_J factors are displayed for $2s^2 2p^2\ ^3P_2$, $2s^2 2p^2\ ^1D_2$, $2s2p^3\ ^3P^o_1$, and $2s2p^3\ ^1P^o_1$ in seven ions along the sequence. The Landé g_J factors are related to the angular momentum coupling. For light elements the values are close to what is expected from pure *LS* coupling. As Z increases coupling conditions change, and we approach values of the g_J factors characteristic of cases with large term mixing.

3.3.2 Summary

Results of energy levels, transition rates, hyperfine interaction constants, and Landé g_J factors for relativistic configuration interaction calculations for transitions among the $(1s^2)\ 2s^2 2p^2$, $2s2p^3$, and $2p^4$ configurations of all carbon-like

Table 3.3.2: Comparison of E1 transition rates for F IV, Na VI, Al VIII, P X, Ar XIII, Ti XVII, Fe XXI from different calculations. Transition rates (A) are given in (s^{-1}).

Levels		This work				
Upper	Lower	A_{RCI}	R	A_{HFR} [67]	A_{CIV3} [69, 70, 71]	$A_{\mathrm{MCHF-BP}}$ [52]
			F IV			
$2s2p^3\ ^3P^o_1$	$2s^22p^2\ ^3P_0$	8.165e+08	1.01	8.912e+08	8.779e+08	8.277e+08
$2s2p^3\ ^1P^o_1$	$2s^22p^2\ ^3P_0$	6.082e+04	0.95		3.180e+04	6.328e+04
$2p^4\ ^1D_2$	$2s2p^3\ ^3D^o_2$	2.924e+05	1.04		2.730e+05	2.921e+05
$2p^4\ ^1D_2$	$2s2p^3\ ^1D^o_2$	3.242e+09	1.01	3.884e+09	3.487e+09	3.213e+09
			Na VI			
$2s2p^3\ ^3P^o_1$	$2s^22p^2\ ^3P_0$	1.250e+09	1.00	1.285e+09	1.328e+08	1.287e+09
$2s2p^3\ ^1P^o_1$	$2s^22p^2\ ^3P_0$	1.232e+05	0.92		7.941e+04	1.223e+05
$2p^4\ ^1D_2$	$2s2p^3\ ^3D^o_2$	1.798e+06	1.03		1.720e+06	1.738e+06
$2p^4\ ^1D_2$	$2s2p^3\ ^1D^o_2$	5.627e+09	1.00	6.265e+09	6.069e+09	5.393e+09
			Al VIII			
$2s2p^3\ ^3P^o_1$	$2s^22p^2\ ^3P_0$	1.694e+09	1.00	1.784e+09	1.786e+09	1.747e+09
$2s2p^3\ ^1P^o_1$	$2s^22p^2\ ^3P_0$	2.633e+05	0.92		2.008e+05	2.579e+05
$2p^4\ ^1D_2$	$2s2p^3\ ^3D^o_2$	7.532e+06	1.02		7.282e+06	7.314e+06
$2p^4\ ^1D_2$	$2s2p^3\ ^1D^o_2$	8.232e+09	1.00	8.959e+09	8.830e+09	7.912e+09
			P X			
$2s2p^3\ ^3P^o_1$	$2s^22p^2\ ^3P_0$	2.144e+09	1.00	2.182e+09	2.246e+09	
$2s2p^3\ ^1P^o_1$	$2s^22p^2\ ^3P_0$	5.997e+05	0.92		5.035e+05	
$2p^4\ ^1D_2$	$2s2p^3\ ^3D^o_2$	2.430e+07	1.02		2.359e+07	
$2p^4\ ^1D_2$	$2s2p^3\ ^1D^o_2$	1.106e+10	1.00	1.187e+10	1.178e+10	
			Ar XIII			
$2s2p^3\ ^3P^o_1$	$2s^22p^2\ ^3P_0$	2.808e+09	1.00	2.784e+09	2.927e+09	
$2s2p^3\ ^1P^o_1$	$2s^22p^2\ ^3P_0$	2.244e+06	0.94		2.010e+06	
$2p^4\ ^1D_2$	$2s2p^3\ ^3D^o_2$	9.790e+07	1.01		9.537e+07	
$2p^4\ ^1D_2$	$2s2p^3\ ^1D^o_2$	1.579e+10	1.00	1.670e+10	1.664e+10	
			Ti XVII			
$2s2p^3\ ^3P^o_1$	$2s^22p^2\ ^3P_0$	3.592e+09	1.00	3.606e+09		
$2s2p^3\ ^1P^o_1$	$2s^22p^2\ ^3P_0$	1.068e+07	0.97			
$2p^4\ ^1D_2$	$2s2p^3\ ^3D^o_2$	3.622e+08	1.01	3.447e+08		
$2p^4\ ^1D_2$	$2s2p^3\ ^1D^o_2$	2.321e+10	1.00	2.429e+10		
			Fe XXI			
$2s2p^3\ ^3P^o_1$	$2s^22p^2\ ^3P_0$	4.213e+10	1.00	4.186e+10		
$2s2p^3\ ^1P^o_1$	$2s^22p^2\ ^3P_0$	2.850e+07	0.98			
$2p^4\ ^1D_2$	$2s2p^3\ ^3D^o_2$	7.878e+08	1.00	7.262e+08		
$2p^4\ ^1D_2$	$2s2p^3\ ^1D^o_2$	3.182e+10	1.00	3.311e+10		

Table 3.3.3: Comparison of E2 and M1 rates in (s^{-1}) for Mg VII.

Upper	Lower	Type	A_{RCI}	$A_{MCHF-BP}$[52]
$2s^2 2p^2\ ^3P_2$	$2s^2 2p^2\ ^3P_0$	E2	2.293e−07	2.328e−07
$2s^2 2p^2\ ^1D_2$	$2s^2 2p^2\ ^3P_0$	E2	1.352e−04	1.277e−04
$2s^2 2p^2\ ^3P_2$	$2s^2 2p^2\ ^3P_1$	E2	4.709e−08	4.684e−08
$2s^2 2p^2\ ^1D_2$	$2s^2 2p^2\ ^3P_1$	E2	3.276e−04	3.534e−04
$2s^2 2p^2\ ^1D_2$	$2s^2 2p^2\ ^3P_2$	E2	2.021e−03	1.965e−03
$2s^2 2p^2\ ^1S_0$	$2s^2 2p^2\ ^3P_2$	E2	3.848e−02	3.809e−02
$2s^2 2p^2\ ^1S_0$	$2s^2 2p^2\ ^1D_2$	E2	3.991e+00	3.890e+00
$2s^2 2p^2\ ^3P_1$	$2s^2 2p^2\ ^3P_0$	M1	2.469e−02	2.546e−02
$2s^2 2p^2\ ^3P_2$	$2s^2 2p^2\ ^3P_1$	M1	8.066e−02	8.031e−02
$2s^2 2p^2\ ^1D_2$	$2s^2 2p^2\ ^3P_1$	M1	1.225e+00	1.237e+00
$2s^2 2p^2\ ^1S_0$	$2s^2 2p^2\ ^3P_1$	M1	3.701e+01	3.710e+01
$2s^2 2p^2\ ^1D_2$	$2s^2 2p^2\ ^3P_2$	M1	3.246e+00	3.224e+00

Table 3.3.4: Landé g_J factors for some ions in the sequence.

Level	F IV	Na VI	Al VIII	P X	Ar XIII	Ti XVII	Fe XXI
$2s^2 2p^2\ ^3P_2$	1.500	1.499	1.497	1.495	1.485	1.446	1.376
$2s^2 2p^2\ ^1D_2$	1.000	1.000	1.001	1.003	1.012	1.048	1.116
$2s2p^3\ ^3P^o_1$	1.500	1.499	1.497	1.494	1.483	1.445	1.385
$2s2p^3\ ^1P^o_1$	1.000	1.001	1.002	1.008	1.026	1.079	1.152

ions from F IV to Ni XXIII are reported in [A2]. The results for the energies and transition rates are compared with the earlier available values obtained from calculations in the Breit-Pauli approximation [69, 70, 71, 52] and by the HFR code [67]. The present energy values generally agree within a few hundred cm^{-1} with the experimentally compiled results for all the studied ions and compare favorably with values from other calculations. The Babushkin (length) and Coulomb (velocity) forms of transition rates agree within less than 1% for a majority of the allowed transitions.

3.4 N-like ions

Transitions in ions of the nitrogen isoelectronic sequence are frequently observed in the spectra of astrophysical sources as well as in tokamak and laser-produced plasmas [74] – [79]. Due to the importance in astrophysics and plasma physics much theoretical and experimental work has been performed on the nitrogen sequence during the years. Using laser irradiated solid targets Kaufman et al. [80] measured the strong $2s^2 2p^3 - 2s2p^4$ and $2s2p^4 - 2p^5$ transition arrays for

ions from Cl XI to V XVII. Later Edlén [81] observed level intervals within and between the configurations $2s^2 2p^3$, $2s2p^4$ and $2p^5$ of the nitrogen sequence. By comparing with the corresponding theoretical values from the tables of Cheng, Kim, and Desclaux [49] he derived recommended level values for ions in the range $Z = 10 - 36$. More highly charged ions can be reached by EBITs and recently some of the $2s^2 2p^3 - 2s2p^4$ transitions in nitrogen-like tungsten have been measured [82].

Some experimental work on transition rates and lifetimes are available. Träbert et al. measured the lifetime of the $2s^2 2p^3\ ^2P_{1/2,3/2}$ levels of S X at a heavy-ion storage ring [83]. Träbert et al. also measured the lifetime of highly ionized silicon using beam-foil spectroscopy [84].

On the theoretical side a number of studies have been done for the nitrogen sequence. Godefroid and Froese Fischer [85] used the MCHF-BP to compute fine-structure splittings and transition rates for the ground configuration in the nitrogen sequence up to Zn XXIV. The same transitions were covered by Becker et al. [86] using the SUPERSTRUCTURE (SS) code [87], also with relativistic corrections in the Breit-Pauli approximation. Merkelis et al. used second-order MBPT with relativistic corrections in the Breit-Pauli approximation to compute oscillator strengths between the levels of the $2s^2 2p^3$, $2s2p^4$ and $2p^5$ [88] and between the levels of the $2s^2 2p^3$ configuration [89]. Ions in the range $Z = 10 - 30$ were covered. Bhatia et al. [79] determined transition parameters between $n = 2$ and $n = 3$ levels of Ar XII, Ti XVI, Fe XX, Zn XXIV, Kr XXX using the SUPERSTRUCTURE code. Orloski and Trigueiros [90] used the multiconfiguration Hartree-Fock relativistic approach with electrostatic parameters optimized by a least-squares procedure to derive weighted oscillator strengths and lifetimes for levels in the Si VIII spectrum. Vilkas and Ishikawa [91] used relativistic MRMP theory calculations for the term energies and transition probabilities of a number of ions in the sequence. Previous MCHF-BP calculations were extended by Tachiev and Froese Fischer [92], who computed energy and E1, E2, M1, M2 transition data between all levels up to $2p^2 3d$ for ions in the range $Z = 7 - 17$. Within the Iron project Nahar [93] used the Breit-Pauli R-matrix (BPRM) method and the SUPERSTRUCTURE code to derive an extensive set of oscillator strengths, line strengths and radiative decay rates for transitions in Fe XX. Jonauskas et al. [94] took a broad approach and applied multiconfiguration Dirac-Fock (MCDF) and configuration interaction on the basis of transformed radial orbitals (CITRO) with variable parameters including relativistic

effects in the Breit-Pauli approximation to derive energies of the 700 lowest levels in Fe XX and corresponding transition parameters. Landi and Bhatia [95] used the SUPERSTRUCTURE code to obtain energy levels, oscillator strengths, and spontaneous radiative decay rates for levels in Mg VI. Finally, Wang et al. [96] used multiconfiguration Dirac-Fock self-consistent field method and the relativistic configuration interaction method with quantum-electrodynamics corrections to calculate the fine-structure energy levels of the ground-state configuration up to $Z = 22$. The goal of the work was to find the mechanism responsible for the orderings of fine-structure energy levels.

3.4.1 Results and evaluation of data

A full set of energies, E1, M1, E2 transition rates, line strengths, oscillator strengths, and lifetimes for the states of the $(1s^2)2s^22p^3$, $2s2p^4$ and $2p^5$ configurations for nitrogen-like ions between F III and Kr XXX are presented in the paper [A3]. In this section we will present data for some ions comparing with other theoretical methods and with experiment.

Table 3.4.1 compares the calculated energies from the present work with energies from MRMP calculations by Vilkas and Ishikawa [91] and with observations. Both sets of calculations agree very well with observations. For the states of the $2s^22p^3$ and $2s2p^4$ configurations, the general agreement with experiment is similar, but for the two states of the $2p^5$ configuration the present RCI calculations are in better agreement with observations. For the $2s^22p^3\ ^2P^o$ states in Ne IV, the energies of the MRMP calculations are in better agreement with observations than are the ones from the RCI calculations. Note, however, that the order of the two fine-structure levels is wrong for MRMP.

In Table 3.4.2, the RCI and MRMP energies for Fe XX are compared with energies from other methods and with observations. On the whole, the RCI and MRMP calculations stand out with energy differences around one order of magnitude smaller that the other methods.

The lifetimes are compared with experimental values and with values from other calculations in Table 3.4.3 and Table 3.4.4. As is seen from the tables, lifetimes for Si VII and S X ions are in good agreement with other theoretical results and experimental measurements.

Table 3.4.5 displays transition rates from different calculations for Si VIII. The present RCI calculations are in excellent agreement with the MCHF-BP calcula-

Table 3.4.1: Comparison of energy levels for Ne IV, Ca XIV, Zn XXIV. Energy levels (E) and the difference of theoretical energies from observed (Diff.) are given in (cm^{-1}).

Level	J	E_{obs} [64]	$Diff_{RCI}$	$Diff_{MRMP}$ [91]
		Ne IV		
$2s^2 2p^3\ ^4S^o$	3/2	0	0	0
$2s^2 2p^3\ ^2D^o$	5/2	41 234.6	211.7	−22.6
	3/2	41 279.5	210.9	−23.5
$2s^2 2p^3\ ^2P^o$	1/2	62 434.6	304.0	−178.6
	3/2	62 441.3	301.0	−197.3
$2s2p^4\ ^4P$	5/2	183 860.0	134.0	−720.0
	3/2	184 477.0	131.9	−720.0
	1/2	184 799.0	136.9	−699.0
$2s2p^4\ ^2D$	5/2	254 080.5	403.6	−930.5
	3/2	254 102.1	406.7	−956.1
$2s2p^4\ ^2S$	1/2	299 627.9	749.1	−211.9
$2s2p^4\ ^2P$	3/2	320 029.6	612.9	−240.6
	1/2	320 740.5	622.6	−234.5
$2p^5\ ^2P^o$	3/2	484 904.1	655.5	4 256.9
	1/2	485 867.1	666.9	4 263.9
		Ca XIV		
$2s^2 2p^3\ ^4S^o$	3/2	0	0	0
$2s^2 2p^3\ ^2D^o$	3/2	105 870	363	231
	5/2	113 520	310	120
$2s^2 2p^3\ ^2P^o$	1/2	172 400	362	128
	3/2	183 360	334	202
$2s2p^4\ ^4P$	5/2	515 800	27	−249
	3/2	535 870	22	−265
	1/2	545 090	15	−228
$2s2p^4\ ^2D$	3/2	710 710	424	−146
	5/2	712 500	385	−237
$2s2p^4\ ^2S$	1/2	825 050	609	239
$2s2p^4\ ^2P$	3/2	858 240	581	−108
	1/2	885 610	586	−243
$2p^5\ ^2P^o$	3/2	1 347 870	575	1 640
	1/2	1 380 110	580	1 655
		Zn XXIV		
$2s^2 2p^3\ ^4S^o$	3/2	0	0	0
$2s^2 2p^3\ ^2D^o$	3/2	188 130	−204	−399
	5/2	254 110	193	−10
$2s^2 2p^3\ ^2P^o$	1/2	357 130	111	−71
	3/2	501 140	−507	−360
$2s2p^4\ ^4P$	5/2	956 600	−170	−232
	3/2	1 084 810	−317	−369
	1/2	1 110 540	−219	−280
$2s2p^4\ ^2D$	3/2	1 328 550	−96	−306
	5/2	1 371 750	193	−27
$2s2p^4\ ^2S$	1/2	1 516 340	234	277
$2s2p^4\ ^2P$	3/2	1 578 630	481	255
	1/2	1 767 650	−727	−1 101
$2p^5\ ^2P^o$	3/2	2 451 700	70	920
	1/2	2 657 600	−835	117

Table 3.4.2: Comparison of energy levels in Fe XX. Energy levels (E) and the difference of theoretical energies from observed (Diff.) are given in (cm^{-1}).

Level	J	E_{obs} [64]	$Diff_{RCI}$	$Diff_{MRMP}$ [91]	$Diff_{SS}$ [79]	$Diff_{BPRM}$ [93]	$Diff_{CITRO}$ [94]	$Diff_{MCDF}$ [94]
$2s^2 2p^3\ ^4S^o$	3/2	0	0	0	0	0	0	0
$2s^2 2p^3\ ^2D^o$	3/2	138 620	198	5	1 978	2 283	236	3 095
	5/2	176 130	212	5	2 859	5 485	−178	3 407
$2s^2 2p^3\ ^2P^o$	1/2	260 270	307	105	−2 697	4 307	201	2 939
	3/2	323 340	226	270	−3 463	5 214	−972	2 622
$2s2p^4\ ^4P$	5/2	752 730	−60	−224	−5 629	4 677	−2 344	919
	3/2	820 630	−46	−222	−7 932	3 497	−2 927	779
	1/2	842 480	−27	−164	−8 037	3 704	−3 057	1 056
$2s2p^4\ ^2D$	3/2	1 042 570	267	−104	1 707	8 055	−3 326	8 354
	5/2	1 058 360	227	−188	2 856	9 713	−2 893	7 862
$2s2p^4\ ^2S$	1/2	1 195 260	476	319	24	9 985	−3 135	10 229
$2s2p^4\ ^2P$	3/2	1 242 430	522	61	8 974	10 880	−3 222	13 338
	1/2	1 340 040	509	−133	5 272	11 265	−3 781	12 356
$2p^5\ ^2P^o$	3/2	1 954 310	611	1 419		12 380	−5 869	17 474
	1/2	2 061 990	619	1 476		14 086	−6 348	17 189

Table 3.4.3: Comparison of lifetimes in Si VIII. Lifetimes (τ) is given in (ps).

Levels	τ_{RCI}	$\tau_{MCHF-BP}$ [92]	τ_{MRMP} [91]	τ_{MBPT} [88, 89]	τ_{exp} [83]
$2s2p^4\ ^4P_{5/2}$	261.2	260.5	266.5	272.1	280 ± 30
$2s2p^4\ ^4P_{3/2}$	251.9	251.3	256.9	263.7	
$2s2p^4\ ^4P_{1/2}$	246.9	246.4	251.6	258.4	
$2s2p^4\ ^2D_{5/2}$	97.3	97.1	98.1	100.0	90 ± 15
$2s2p^4\ ^2D_{3/2}$	95.4	95.1	96.6	98.6	
$2s2p^4\ ^2P_{3/2}$	23.1	23.1	23.1	23.2	23 ± 3
$2s2p^4\ ^2P_{1/2}$	23.2	23.1	23.2	23.2	

Table 3.4.4: Comparison of lifetimes in S X. Lifetimes (τ) is given in (ms).

Levels	τ_{RCI}	$\tau_{MCHF-BP}$ [92]	τ_{MBPT} [88, 89]	τ_{exp} [84]
$2s^2 2p^3\ ^2P^o_{1/2}$	5.111	5.085	5.28	5.20 ± 0.15
$2s^2 2p^3\ ^2P^o_{3/2}$	2.109	2.103	2.16	2.10 ± 0.06

Table 3.4.5: Comparison of E1 transition rates in Si VIII. Transition rates (A) are given in (s^{-1}).

Levels		This work				
Upper	Lower	A_{RCI}	R	$A_{\mathrm{MCHF-BP}}$ [92]	A_{MRMP} [91]	A_{MBPT} [88, 89]
$2s2p^4\ ^2P_{3/2}$	$2s^22p^3\ ^2P^o_{3/2}$	6.706e+09	1.00	6.711e+09	6.742e+09	6.812e+09
$2s2p^4\ ^2P_{3/2}$	$2s^22p^3\ ^2P^o_{1/2}$	1.704e+09	1.00	1.706e+09	1.728e+09	1.716e+09
$2s2p^4\ ^2P_{3/2}$	$2s^22p^3\ ^2D^o_{5/2}$	3.037e+10	1.00	3.048e+10	3.022e+10	3.021e+10
$2s2p^4\ ^2P_{3/2}$	$2s^22p^3\ ^2D^o_{3/2}$	4.437e+09	1.00	4.453e+09	4.627e+09	4.441e+09
$2s2p^4\ ^2P_{1/2}$	$2s^22p^3\ ^2P^o_{3/2}$	8.105e+09	1.00	8.124e+09	7.913e+09	8.048e+09
$2s2p^4\ ^2P_{1/2}$	$2s^22p^3\ ^2P^o_{1/2}$	5.044e+09	1.00	5.053e+09	5.567e+09	5.195e+09
$2s2p^4\ ^2P_{1/2}$	$2s^22p^3\ ^2D^o_{3/2}$	2.995e+10	1.00	3.006e+10	2.963e+10	2.978e+10
$2s2p^4\ ^2D_{3/2}$	$2s^22p^3\ ^2P^o_{1/2}$	1.080e+09	1.00	1.082e+09	1.061e+09	1.025e+09
$2s2p^4\ ^2D_{3/2}$	$2s^22p^3\ ^2D^o_{5/2}$	7.357e+08	1.01	7.360e+08	7.486e+08	7.148e+08
$2s2p^4\ ^2D_{3/2}$	$2s^22p^3\ ^2D^o_{3/2}$	8.623e+09	1.00	8.645e+09	8.547e+09	8.404e+09
$2s2p^4\ ^2D_{5/2}$	$2s^22p^3\ ^2P^o_{3/2}$	1.507e+09	0.99	1.510e+09	1.489e+09	1.434e+09
$2s2p^4\ ^2D_{5/2}$	$2s^22p^3\ ^2D^o_{3/2}$	3.585e+08	0.99	3.615e+08	3.366e+08	3.567e+08
$2s2p^4\ ^2D_{5/2}$	$2s^22p^3\ ^2D^o_{5/2}$	8.408e+09	1.00	8.424e+09	8.371e+09	8.212e+09
$2s2p^4\ ^4P_{1/2}$	$2s^22p^3\ ^4S^o_{3/2}$	4.049e+09	1.00	4.058e+09	3.974e+09	3.870e+09
$2s2p^4\ ^4P_{3/2}$	$2s^22p^3\ ^4S^o_{3/2}$	3.968e+09	1.00	3.978e+09	3.893e+09	3.792e+09
$2s2p^4\ ^4P_{5/2}$	$2s^22p^3\ ^4S^o_{3/2}$	3.826e+09	1.00	3.836e+09	3.753e+09	3.675e+09
$2s2p^4\ ^2D_{5/2}$	$2s^22p^3\ ^4S^o_{3/2}$	4.455e+04	1.05	4.776e+04		4.534e+04
$2s2p^4\ ^2D_{3/2}$	$2s^22p^3\ ^4S^o_{3/2}$	9.895e+04	1.02	1.040e+05		9.182e+04
$2s2p^4\ ^2S_{1/2}$	$2s^22p^3\ ^4S^o_{3/2}$	8.146e+06	1.00	8.206e+06		8.058e+06
$2s2p^4\ ^2P_{1/2}$	$2s^22p^3\ ^4S^o_{3/2}$	5.452e+06	1.05	5.414e+06		5.054e+06

tions by Tachiev and Froese Fischer [92], with a mean difference of only 0.13 % for the displayed allowed transitions and 2.5 % for weak intercombination transitions. The agreement with the MRMP [91] and MBPT [88, 89] calculations is also very good, although worse than for MCHF-BP.

Table 3.4.6 gives transition rates, including M1 and E2 transitions within the ground configuration, from different calculations in Fe XX. There is a very good consistency between the present RCI calculations and the MBPT [88, 89] calculations. Only for two E1 transitions with relatively low rates do the differences exceed a few percent. The RCI calculations are also in reasonable agreement with the MCDF calculations by Jonauskas *et al.* [94]. When it comes to the Breit-Pauli R-matrix (BPRM) calculations by Nahar, there are considerable differences for some transitions. For example, both the $2s2p^4\ ^2D_{3/2} - 2s^22p^3\ ^4S^o_{3/2}$ and $2s2p^4\ ^2P_{3/2} - 2s^22p^3\ ^4S^o_{3/2}$ transition rates from the latter calculation differ by a factor two from other calculations.

Table 3.4.6: Comparison of E1, E2 and M1 transition rates in Fe XX. Transition rates (A) are given in (s^{-1}).

Levels		This work					
Upper	Lower	A_{RCI}	R	A_{MCDF} [94]	A_{BPRM} [93]	A_{MBPT} [88, 89]	A_{NIST} [64]
E1 transitions							
$2s2p^4\ ^2P_{3/2}$	$2s^22p^3\ ^2P^o_{3/2}$	9.038e+09	0.99	9.36e+09		9.187e+09	9.40e+09^C
$2s2p^4\ ^2P_{3/2}$	$2s^22p^3\ ^2P^o_{1/2}$	8.380e+09	1.00	8.64e+09		8.315e+09	9.1e+09^C
$2s2p^4\ ^2P_{3/2}$	$2s^22p^3\ ^2D^o_{5/2}$	9.321e+10	1.00	9.74e+10		9.247e+10	1.0e+11^C
$2s2p^4\ ^2P_{3/2}$	$2s^22p^3\ ^2D^o_{3/2}$	1.362e+10	1.00	1.47e+10		1.372e+10	1.47e+10^C
$2s2p^4\ ^2P_{1/2}$	$2s^22p^3\ ^2P^o_{3/2}$	8.835e+10	1.00	9.20e+10	8.26e+10	8.769e+10	9.6e+10^C
$2s2p^4\ ^2P_{1/2}$	$2s^22p^3\ ^2P^o_{1/2}$	3.677e+09	1.00	4.14e+09		3.720e+09	4.4e+09^D
$2s2p^4\ ^2P_{1/2}$	$2s^22p^3\ ^2D^o_{3/2}$	2.648e+10	1.00	2.85e+10		2.614e+10	2.91e+10^C
$2s2p^4\ ^2D_{3/2}$	$2s^22p^3\ ^2P^o_{1/2}$	2.668e+09	1.00	2.81e+09		2.661e+09	2.98e+09^C
$2s2p^4\ ^2D_{3/2}$	$2s^22p^3\ ^2D^o_{5/2}$	3.036e+07	1.22	4.95e+07		2.539e+07	4.3e+07^E
$2s2p^4\ ^2D_{3/2}$	$2s^22p^3\ ^2D^o_{3/2}$	3.849e+10	1.00	3.97e+10		3.825e+10	4.3e+10^C
$2s2p^4\ ^2D_{5/2}$	$2s^22p^3\ ^2P^o_{3/2}$	5.416e+09	0.98	5.61e+09		5.500e+09	6.0e+09^C
$2s2p^4\ ^2D_{5/2}$	$2s^22p^3\ ^2D^o_{3/2}$	1.446e+07	1.07	1.39e+07	1.09e+07	1.096e+07	2.7e+07^E
$2s2p^4\ ^2D_{5/2}$	$2s^22p^3\ ^2D^o_{5/2}$	2.930e+10	1.00	3.04e+10		2.916e+10	3.3e+10^C
$2s2p^4\ ^4P_{1/2}$	$2s^22p^3\ ^4S^o_{3/2}$	1.875e+10	1.00	1.92e+10	1.28e+10	1.852e+10	2.09e+10^C
$2s2p^4\ ^4P_{3/2}$	$2s^22p^3\ ^4S^o_{3/2}$	1.676e+10	1.00	1.72e+10	1.37e+10	1.667e+10	1.86e+10^C
$2s2p^4\ ^4P_{5/2}$	$2s^22p^3\ ^4S^o_{3/2}$	1.186e+10	1.00	1.22e+10	1.19e+10	1.194e+10	1.3e+10^C
$2s2p^4\ ^2D_{5/2}$	$2s^22p^3\ ^4S^o_{3/2}$	1.583e+07	1.00	1.40e+07		1.602e+07	
$2s2p^4\ ^2D_{3/2}$	$2s^22p^3\ ^4S^o_{3/2}$	1.555e+09	1.01	1.52e+09	2.87e+09	1.428e+09	1.9e+09^E
$2s2p^4\ ^2S_{1/2}$	$2s^22p^3\ ^4S^o_{3/2}$	1.663e+09	1.00	1.69e+09	1.48e+10	1.539e+09	1.9e+09^E
$2s2p^4\ ^2P_{3/2}$	$2s^22p^3\ ^4S^o_{3/2}$	4.082e+09	1.01	4.16e+09	8.75e+09	3.811e+09	4.6e+09^E
$2s2p^4\ ^2P_{1/2}$	$2s^22p^3\ ^4S^o_{3/2}$	1.212e+08	1.03	1.32e+08		1.226e+08	
E2 transitions							
$2s^22p^3\ ^2P^o_{1/2}$	$2s^22p^3\ ^2D^o_{3/2}$	5.297e+00	1.07		5.40e+00	4.99e+00	5.2e+00^E
$2s^22p^3\ ^2P^o_{3/2}$	$2s^22p^3\ ^2D^o_{5/2}$	1.497e+01	1.06		1.54e+01	1.39e+01	1.5e+01^E
$2p^5\ ^2P^o_{1/2}$	$2p^5\ ^2P^o_{3/2}$	2.072e+00	1.07		2.15e+00	1.87e+00	2.2e+00^E
M1 transitions							
$2s^22p^3\ ^2P^o_{1/2}$	$2s^22p^3\ ^4S^o_{3/2}$	3.136e+04		3.13e+04	2.97e+04	2.98e+04	3.3e+04^D
$2s^22p^3\ ^2P^o_{3/2}$	$2s^22p^3\ ^4S^o_{3/2}$	2.921e+04		2.98e+04	2.91e+04	2.85e+04	2.91e+04^C
$2s^22p^3\ ^2P^o_{1/2}$	$2s^22p^3\ ^2D^o_{3/2}$	5.801e+03		5.87e+03	6.06e+03	5.62e+03	6.10e+03^D
$2s^22p^3\ ^2P^o_{3/2}$	$2s^22p^3\ ^2D^o_{3/2}$	4.341e+04		4.28e+04	4.34e+04	4.06e+04	4.49e+04^D

The ratings C, D, E in the A_{NIST} column refer to estimated accuracies for transition probabilities. C: $\leq 25\%$, D: $\leq 50\%$, E: $> 50\%$.

3.4.2 Summary

All results of spectroscopic data for the levels of the $2s^2 2p^3$, $2s2p^4$, and $2p^5$ configurations in F III to Kr XXX are computed using a fully relativistic configuration-interaction method and reported in [A3]. Our computed energies agree very well with the experimental values with differences between 300 and 600 cm^{-1} for the majority of the ions in the sequence. Some possible experimental misidentifications of lines in Si VIII have been pointed out. The transition energies and rates from the present study are in excellent agreement with the data given by Tachiev and Froese Fischer [92]. For the higher-ionized atoms, the transition data are believed to be more accurate than the data from other methods.

3.5 O-like ions

Baluja and Zeipen [97] calculated excitation energies and transition probabilities for M1 and E2 transitions within the $2p^4$ ground-state configuration in the O I isoelectronic sequence for $Z = 8-36$ using the CIV3 code. The MCHF-BP were performed by Tachiev and Froese Fischer [92, 52] who computed energy and E1, E2, M1, and M2 transition data between all levels up to $2p^3 3d$ for oxygen-like ions in the range $Z = 8-20$. Bhatia and Landi performed calculations for several oxygen-like ions such as Ne III [98] and Ca XIII [99]. Landi et al. [100] used the SUPERSTRUCTURE code to obtain energy levels, oscillator strengths, and radiative transition propabilities for all the oxygen-like ions with $Z = 11-30$. Deb and Hibbert [101] presented accurate oscillator strengths, line strengths and radiative rates for 1073 E1 transitions among the 86 levels belonging to the $2s^2 2p^4, 2s2p^5, 2p^6$, and $2s^2 2p^3 ({}^4S^o,\ {}^2D^o,\ {}^2P^o) 3l$ configurations in Mg V using the CIV3 code.

Gaigalas et al. [102, 103] used the second-order many-body perturbation theory (MBPT) with relativistic corrections in the Breit-Pauli approximation to compute energy spectra, electric dipole, quadrupole and magnetic dipole transitions in the oxygen isoelectronic sequence between the levels of the $1s^2 2s^2 2p^4$, $1s^2 2s2p^5$ and $1s^2 2p^6$ configurations for $Z = 10-26$. Froese Fisher et al. [104] used the MCDHF method to calculate transition rates for the $2s^2 2p^4\ {}^3P_{1,2}-2s^2 2p^3 3s\ {}^5S^o_2$ and $2s^2 2p^4\ {}^3P_{1,2} - 2s2p^5\ {}^3P^o_2$ transitions in the oxygen-like ions for $Z = 9-18$. Vilkas et al. [105, 106] used MRMP perturbation theory for the ground and low-lying excited states of oxygen-like iron and oxygen-like ions

with nuclear charge up to $Z = 60$. No transition data were published. Safronova and Shlyaptseva [107] used the $1/Z$ perturbation theory method with inclusion of relativistic and radiative corrections to calculate absolute energies and autoionization rates of the C-, N-, O- and F-like autoionizing doubly-excited states for $Z = 18 - 26$. Bogdanovich et al. used the configuration interaction method to calculate energy spectra for in Mg V, Si VII, and S IX ions [108]; energy spectra and lifetimes for all states of first five configurations of Cl X [109]; and energy spectra, oscillator strengths and the emission transition probabilities of oxygen-like chromium Cr XVII [110].

During the last few years highly ionized ions of iron were of particular interest. Jonauskas et al. [111] reported 656 energy levels and 214 840 E1, E2 and M1 transition probabilities in oxygen-like Fe XIX using MCDHF. Landi and Gu [112] produced a large amount of radiative and collisional data for ions of Fe XVII-XXII using the FAC code. Nahar [113] presented an extensive set of oscillator strengths, line strengths, and radiative decay rates for allowed and forbidden transitions in Fe XIX using the relativistic Breit-Pauli R-matrix method.

3.5.1 Results and evaluation of data

A full set of energies, E1, M1, E2, and M2 transition rates, oscillator strengths, and lifetimes for the states of the $(1s^2)\ 2s^2 2p^4$, $2s2p^5$, and $2p^6$ configurations for oxygen-like ions between F II to Kr XXIX are presented in the paper [A4]. In this section we will present data for some ions comparing with other theoretical methods and with experiment.

For lower degrees on ionization, the Breit-Pauli (BP) method has often been used in the past. In Table 3.5.1, results from three fully relativistic methods based on Dirac theory (RCI, MRMP, MBPT) are compared with Breit-Pauli methods (MCHF-BP, SS, and CIV3). From the differences, we see that in Ne III ($Z = 10$) some of the BP methods are among the most accurate but by Ca XIII ($Z = 20$) the fully relativistic methods that include the Breit and QED corrections have become the most accurate with the present RCI results having the lowest maximun difference with observed. For all levels there is good agreement between RCI and MRMP, except for the highest level. Unlike the present work, many early calculations (MCHF-BP, SS, CIV3, for example) treated the core as inactive. Table 3.5.1 shows the importance of the core-polarization correction for levels with a vacancy in the $2s$ shell. Present results are in much better agreement with

Table 3.5.1: Comparison of theoretical energy levels for Ne III, Ca XIII with values derived from observed wavelengths. Energy levels (E) and the difference of theoretical energies from observed (Diff.) are given in (cm^{-1}).

Level	J	E_{obs} [64]	$Diff_{RCI}$	$Diff_{MRMP}$ [106]	$Diff_{MBPT}$ [102]	$Diff_{MCHF-BP}$ [54]	$Diff_{SS}$ [98, 95]	$Diff_{CIV3}$ [97]
				Ne III				
$2s^2 2p^4\ ^3P$	2	0	0	0	0	0	0	0
	1	643	2	−15	2	−5	101	−12
	0	921	2	−22	5	−9	148	−18
$2s^2 2p^4\ ^1D$	2	25 841	113	−82	−268	256	3 378	894
$2s^2 2p^4\ ^1S$	0	55 753	305	−371	−294	19	16 731	−30
$2s2p^5\ ^3P^o$	2	204 290	318	345	−3 604	428	11 058	
	1	204 873	327	363	−3 597	424	11 135	
	0	205 194	409	345	−3 596	423	11 173	
$2s2p^5\ ^1P^o$	1	289 479	836	2 180	−1 260	1 224	26 032	
				Ca XIII				
$2s^2 2p^4\ ^3P$	2	0	0	0	0	0	0	0
	1	24 460	8	−80	−251	340	556	−49
	0	28 888	8	−72	−151	−56	600	−319
$2s^2 2p^4\ ^1D$	2	88 208	129	4	80	879	3 737	1 163
$2s^2 2p^4\ ^1S$	0	178 613	310	−43	−597	30	2 074	−393
$2s2p^5\ ^3P^o$	2	618 268	243	58	−2 186	3 445	10 265	
	1	638 238	274	129	−2 311	3 701	10 711	
	0	650 105	309	88	−2 386	3 884	10 956	
$2s2p^5\ ^1P^o$	1	850 300	532	189	−3 071	4 358	19 496	
$2p^6\ ^1S$	0	1 440 320	849	−2 361	−6 083	5 163	34 605	

observed levels.

A very important ion is Fe XIX for which energies have been computed by a variety of relativistic methods, including the recently developed FAC code [114]. Differences with observed energy levels are reported in Table 3.5.2. Except for the energy of $2p^6\ ^1S$, the MRMP energies are the most accurate but the RCI values are more regular in their difference with observed.

For ions in the region $Z > 30$ uncertainties in the "observed" energies become substantial. There are significant discrepancies for As XXVI, Se XXVII and Br XXVIII spectra between the NIST database values based on measurements reported by [115] and those derived by [116] from a variety of sources. Both are reported in Table 3.5.3 and for each method – (c) RCI, and (d) MRMP – the calculated energy level is given along with the differences from the observed values and Edlén values obtained from semiempirically fitted $1/Z$ expansions. For the $2s^2 2p^4$ levels in Br XXVIII both theoretical results are in better agreement with the Edlén values.

Table 3.5.2: Comparison of fully relativistic theoretical energy levels with values derived from observed wavelengths for Fe XIX. Energy levels (E) and the difference of theoretical energies from observed (Diff.) are given in (cm^{-1}).

Level	J	E_{obs} [64]	$Diff_{RCI}$	$Diff_{MRMP}$ [106]	$Diff_{PT}$ [107]	$Diff_{MBPT}$ [102]	$Diff_{FAC}$ [112]	$Diff_{MCDF}$ [111]
$2s^2 2p^4\ ^3P$	2	0	0	0	0	0	0	0
	0	75 250	63	−32	150	−508	−52	196
	1	89 441	−7	−190	−1 241	−1 882	−620	−650
$2s^2 2p^4\ ^1D$	2	168 852	133	−60	−1 252	−971	1 726	1 995
$2s^2 2p^4\ ^1S$	0	325 140	277	−191	−240	−4 016	281	1 396
$2s2p^5\ ^3P^o$	2	922 890	154	−35	8 010	−5 455	6 341	10 191
	1	984 740	180	51	8 160	−6 498	6 506	10 266
	0	1 030 020	179	−28	6 680	−7 267	6 038	9 672
$2s2p^5\ ^1P^o$	1	1 267 600	493	171	2 200	−8 673	15 314	20 173
$2p^6\ ^1S$	0	2 134 180	778	−1 370	12 620	−13 969	26 521	41 465

Table 3.5.3: Comparison of fully relativistic theoretical energy levels for Zn XXIII, Ge XXV, As XXVI, Se XXVII, Br XXVIII, Kr XXIX with values derived from observed and semi-empirical (SE) wavelengths. Energy levels (E) and the difference of theoretical energies from observed (Diff.(1)) and SE (Diff.(2)) ones are given (in cm^{-1}).

Level	J	Obs.(NIST) [64]	SE(Edlén) [116]	Diff.(1) This work	Diff.(2) This work	Diff.(1) [106]	Diff.(2) [106]
				Zn XXIII			
$2s^2 2p^4\ ^3P$	2	0	0	0	0	0	0
	0	110 340	110 437	−24	−121	105	8
	1	179 060	178 973	−129	−42	−15	72
$2s^2 2p^4\ ^1D$	2	267 120	267 325	272	67	288	83
$2s^2 2p^4\ ^1S$	0	512 070	512 557	519	32	682	195
$2s2p^5\ ^3P^o$	2	1 176 110	1 176 226	189	73	1 410	1 294
	1	1 282 970	1 282 957	92	105	1 406	1 419
	0	1 380 580	1 380 576	58	62	1 350	1 354
$2s2p^5\ ^1P^o$	1	1 626 230	1 626 251	608	587	1 755	1 734
$2p^6\ ^1S$	0	2 697 570	2 697 367	847	1 050	4 461	4 664
				Ge XXV			
$2s^2 2p^4\ ^3P$	2	0	0	0	0	0	0
	0	127 240	127 793	44	−509	161	−392
	1	243 540	243 568	−34	−62	112	84
$2s^2 2p^4\ ^1D$	2	336 200	336 229	44	15	108	79
$2s^2 2p^4\ ^1S$	0	646 650	646 933	148	−135	362	79
$2s2p^5\ ^3P^o$	2	1 324 130	1 324 308	113	−65	1 343	1 165
	1	1 457 310	1 457 440	169	39	1 518	1 388
	0	1 596 720	1 597 034	214	−100	1 590	1 276
$2s2p^5\ ^1P^o$	1	1 842 920	1 842 732	480	668	1 717	1 905
$2p^6\ ^1S$	0	3 021 850	3 021 332	777	1 295	4 516	5 034
				As XXVI			
$2s^2 2p^4\ ^3P$	2	0	0	0	0		
	0	137 320	136 385	−1 720	−785		
	1	281 330	281 802	404	−68		

Continued...

Table 3.5.3: (continued)

Level	J	Obs.(NIST) [64]	SE(Edlén) [116]	Diff.(1) This work	Diff.(2) This work	Diff.(1) [106]	Diff.(2) [106]
$2s^2 2p^4\ ^1D$	2	377 300	376 598	−714	−12		
$2s^2 2p^4\ ^1S$	0	726 580	726 315	−509	−244		
$2s2p^5\ ^3P^o$	2	1 403 750	1 404 724	822	−152		
	1	1 550 530	1 551 663	1 171	38		
	0	1 716 190	1 717 549	1 152	−207		
$2s2p^5\ ^1P^o$	1	1 962 370	1 962 613	955	712		
$2p^6\ ^1S$	0		3 195 915		1 476		
				Se XXVII			
$2s^2 2p^4\ ^3P$	2	0	0	0	0		
	0	147 760	144 941	−3 942	−1 123		
	1	323 690	324 396	638	−68		
$2s^2 2p^4\ ^1D$	2	422 380	421 316	−1 101	−37		
$2s^2 2p^4\ ^1S$	0	814 600	814 628	−347	−375		
$2s2p^5\ ^3P^o$	2	1 488 420	1 489 811	1 140	−251		
	1	1 649 100	1 650 791	1 766	75		
	0	1 845 030	1 847 080	1 712	−338		
$2s2p^5\ ^1P^o$	1	2 090 120	2 091 234	1 868	754		
$2p^6\ ^1S$	0		3 379 728		1 704		
				Br XXVIII			
$2s^2 2p^4\ ^3P$	2	0	0	0	0	0	0
	0	218 800	153 478	−66 846	−1 524	−66 765	−1 443
	1	379 800	371 663	−8 194	−57	−7 942	195
$2s^2 2p^4\ ^1D$	2	483 040	470 699	−12 397	−56	−12 236	105
$2s^2 2p^4\ ^1S$	0	944 150	912 501	−32 182	−533	−31 868	−219
$2s2p^5\ ^3P^o$	2		1 579 903		−366		1 042
	1		1 755 028		168		1 656
	0		1 986 274		−490		1 122
$2s2p^5\ ^1P^o$	1		2 229 358		791		2 278
$2p^6\ ^1S$	0		3 573 416		1 999		6 070
				Kr XXIX			
$2s^2 2p^4\ ^3P$	2	0	0	0	0	0	0
	0	160 700	162 011	−676	−1 987	−612	−1 923
	1	423 820	423 933	80	−33	365	252
$2s^2 2p^4\ ^1D$	2	524 890	525 066	119	−57	320	144
$2s^2 2p^4\ ^1S$	0		1 020 595		−730		−363
$2s2p^5\ ^3P^o$	2	1 674 650	1 675 351	181	−520	1 632	931
	1	1 864 320	1 864 603	601	−318	2 139	1 856
	0	2 133 800	2 135 798	1 328	−670	3 039	1 041
$2s2p^5\ ^1P^o$	1	2 377 700	2 377 764	867	803	2 449	2 385
$2p^6\ ^1S$	0		3 777 648		2 351		6 593

On the whole, the RCI and MRMP calculations stand out as having the best agreement with observation. Their energy differences are about an order of magnitude smaller than those for other methods.

In Table 3.5.4 lifetimes from present calculations are compared with results from MCHF-BP calculations by Fischer and Tachiev and observations. As seen

from the table, there is good agreement between theory and experiment for F II and Ne III but for the more highly ionized spectra, the agreement becomes even better. All the computed values are within the uncertainties of experimental measurement.

Table 3.5.4: Comparison of lifetimes. Lifetimes (τ) is given in (*ms*).

Ion	State	τ_{RCI}	$\tau_{\text{MCHF-BP}}$ [54]	τ_{exp}
F II	$2s^2 2p^4\ ^1S_0$	397.8	430.22	420 ± 12 [117]
Ne III	$2s^2 2p^4\ ^1S_0$	206.5	216.73	223 ± 11 [118]
				213 ± 4 [119]
Si VII	$2s^2 2p^4\ ^1D_2$	63.87	63.341	63.6 ± 0.7 [120]
P VIII	$2s^2 2p^4\ ^1D_2$	28.69	28.332	28.63 ± 0.08 [121]
S IX	$2s^2 2p^4\ ^1D_2$	13.74	13.510	13.79 ± 0.05 [121]
Ar XI	$2s^2 2p^4\ ^3P_1$	14.97	14.560	14.8 ± 1.1 [122]

Table 3.5.5 displays E1, E2, M1 and M2 transition rates from different calculations and NIST critically evaluated data for Mg V. The NIST values are based on [92] calculations of line strengths and observed wavelengths and include an accuracy indicator which, for the highest accuracy rating (B+) corresponds to an estimated error of $\leq 7\%$. The accuracy of our transition rates is similar to the accuracy of the transition energies in Table 3.5.1 and, for this moderately ionized atom, there is good agreement between CIV3, MCHF-BP, and RCI.

Table 3.5.6 gives transition rates, including M1 and E2 transitions within the ground configuration, from different calculations and experiment in Fe XIX. Again, the NIST values are based on theoretical calculations for the line strength along with observed wavelengths and, as shown in the table, have a fairly low accuracy rating. The NIST values for E1 transitions in this table are based on Dirac-Hartree-Fock calculations by [49], whereas the E2 and M1 transitions are from a SUPERSTRUCTURE calculations [123]. There is good agreement with the BPRM results of [113] and the SS results of [100] who compute the transition rates by using observed wavelengths and only a computed line strength.

Table 3.5.5: Comparison of transition rates in Mg V. Transition probabilities (A) are given in (s^{-1}).

Levels		This work					
Upper	Lower	A_{RCI}	R	A_{NIST} [64]	$A_{MCHF-BP}$ [54]	A_{MBPT} [102, 103]	A_{CIV3} [101]
E1 transitions							
$2s2p^5\ ^3P^o_2$	$2s^22p^4\ ^3P_2$	6.297e+09	1.01	6.12e+09^{B+}	6.3532e+09	5.930e+09	6.292e+09
$2s2p^5\ ^3P^o_1$	$2s^22p^4\ ^3P_2$	3.571e+09	1.01	3.46e+09^{B+}	3.5997e+09	3.356e+09	3.568e+09
$2s2p^5\ ^1P^o_1$	$2s^22p^4\ ^3P_2$	3.133e+07	1.03	3.08e+07^{C}	3.1443e+07	3.006e+07	
$2s2p^5\ ^3P^o_2$	$2s^22p^4\ ^3P_1$	2.057e+09	1.01	2.00e+09^{B+}	2.0762e+09	1.941e+09	2.056e+09
$2s2p^5\ ^3P^o_1$	$2s^22p^4\ ^3P_1$	2.096e+09	1.01	2.04e+09^{B+}	2.1145e+09	1.975e+09	2.094e+09
$2s2p^5\ ^3P^o_0$	$2s^22p^4\ ^3P_1$	8.479e+09	1.01	8.23e+09^{B+}	8.5455e+09	7.975e+09	8.468e+09
$2s2p^5\ ^1P^o_1$	$2s^22p^4\ ^3P_1$	6.630e+05	1.13	5.93e+05^{D}	6.3117e+05	5.521e+05	6.610e+05
$2s2p^5\ ^3P^o_1$	$2s^22p^4\ ^3P_0$	2.770e+09	1.01	2.69e+09^{B+}	2.7942e+09	2.611e+09	2.767e+09
$2s2p^5\ ^1P^o_1$	$2s^22p^4\ ^3P_0$	1.212e+06	1.08	1.15e+06^{D+}	1.2064e+06	1.126e+06	1.169e+06
$2s2p^5\ ^3P^o_2$	$2s^22p^4\ ^1D_2$	4.021e+06	0.95	4.01e+06^{C}	4.0096e+06	3.963e+06	4.020e+06
$2s2p^5\ ^3P^o_1$	$2s^22p^4\ ^1D_2$	3.125e+05	1.19	2.65e+05^{D}	3.0242e+05	2.446e+05	3.148e+05
$2s2p^5\ ^1P^o_1$	$2s^22p^4\ ^1D_2$	3.128e+10	1.01	3.12e+10^{B+}	3.1711e+10	3.112e+10	3.130e+10
$2s2p^5\ ^3P^o_1$	$2s^22p^4\ ^1S_0$	5.981e+05	0.90	5.79e+05^{D+}	6.1289e+05	5.534e+05	6.043e+05
$2s2p^5\ ^1P^o_1$	$2s^22p^4\ ^1S_0$	1.866e+09	0.99	1.89e+09^{B+}	1.8696e+09	1.929e+09	1.825e+09
$2p^6\ ^1S_0$	$2s2p^5\ ^3P^o_1$	7.180e+06	1.13	6.58e+06^{D}	7.1894e+06	5.984e+06	7.202e+06
$2p^6\ ^1S_0$	$2s2p^5\ ^1P^o_1$	2.243e+10	1.01	2.20e+10^{B+}	2.2871e+10	2.149e+10	2.259e+10
E2 transitions							
$2p^6\ ^1S_0$	$2s^22p^4\ ^3P_2$	3.820e+02	1.02	3.57e+02^{C}	3.6981e+02	3.514e+02	
$2s^22p^4\ ^1S_0$	$2s^22p^4\ ^1D_2$	4.195e+00	1.16	4.09e+00^{B+}	3.9827e+00	4.071e+00	
$2p^6\ ^1S_0$	$2s^22p^4\ ^1D_2$	2.735e+05	1.02	2.74e+05^{B}	2.6967e+05	2.831e+05	
M1 transitions							
$2s^22p^4\ ^1D_2$	$2s^22p^4\ ^3P_2$	1.898e+00		1.87e+00^{B}	1.9046e+00	1.861e+00	
$2s^22p^4\ ^1S_0$	$2s^22p^4\ ^3P_1$	2.221e+01		2.15e+01^{B}	2.1971e+01	2.104e+01	
$2p^6\ ^1S_0$	$2s^22p^4\ ^3P_1$	5.564e+00		3.15e+01^{E}	5.7074e+00	5.737e+00	
$2s2p^5\ ^1P^o_1$	$2s2p^5\ ^3P^o_2$	3.428e+00		3.39e+00^{C+}	3.3906e+00	3.465e+00	
$2s2p^5\ ^1P^o_1$	$2s2p^5\ ^3P^o_1$	1.899e+00		1.95e+00^{C+}	1.9508e+00	1.992e+00	
$2s2p^5\ ^1P^o_1$	$2s2p^5\ ^3P^o_0$	2.591e+00		2.54e+00^{C+}	2.5417e+00	2.595e+00	
M2 transitions							
$2s2p^5\ ^3P^o_2$	$2s^22p^4\ ^3P_2$	6.632e+00		6.60e+00^{B}	6.6809e+00		
$2s2p^5\ ^3P^o_0$	$2s^22p^4\ ^3P_2$	4.150e+00		4.13e+00^{B}	4.1766e+00		
$2s2p^5\ ^1P^o_1$	$2s^22p^4\ ^3P_2$	3.236e+01		3.22e+01^{B}	3.2874e+01		
$2s2p^5\ ^3P^o_1$	$2s^22p^4\ ^3P_1$	4.330e+00		4.31e+00^{B}	4.3617e+00		
$2s2p^5\ ^1P^o_1$	$2s^22p^4\ ^3P_1$	1.095e+01		1.09e+01^{B}	1.1119e+01		
$2s2p^5\ ^3P^o_2$	$2s^22p^4\ ^1D_2$	1.225e+00		1.22e+00^{B}	1.2313e+00		
$2s2p^5\ ^3P^o_1$	$2s^22p^4\ ^1D_2$	2.994e+00		2.98e+00^{B}	3.0059e+00		
$2s2p^5\ ^3P^o_0$	$2s^22p^4\ ^1D_2$	4.273e+00		4.25e+00^{B}	4.2829e+00		
$2p^6\ ^1S_0$	$2s2p^5\ ^3P^o_2$	9.131e+01		9.02e+01^{B}	9.2852e+01		

The ratings $B, B+, C, C+, D, D+, E$ in the A_{NIST} column refer to estimated accuracies for transition probabilities. $B+$: $\leq 7\%$, B: $\leq 10\%$, $C+$: $\leq 18\%$, C: $\leq 25\%$, $D+$: $\leq 40\%$, D: $\leq 50\%$, E: $> 50\%$.

Table 3.5.6: Comparison of transition rates in Fe XIX. Transition probabilities (A) are given in (s^{-1}).

Levels		This work					
Upper	Lower	$A_{\rm RCI}$	R	$A_{\rm NIST}$ [64]	$A_{\rm MCDF}$ [111]	$A_{\rm SS}$ [100]	$A_{\rm BPRM}$ [113]
E1 transitions							
$2s2p^5\ ^3P^o_2$	$2s^22p^4\ ^3P_2$	3.370e+10	1.00	3.9e+10^C	3.57e+10	3.492e+10	3.35e+10
$2s2p^5\ ^3P^o_1$	$2s^22p^4\ ^3P_2$	2.779e+10	1.01	3.17e+10^C	2.91e+10	2.855e+10	2.77e+10
$2s2p^5\ ^1P^o_1$	$2s^22p^4\ ^3P_2$	1.099e+10	1.01	1.3e+10^E	1.15e+10	1.083e+10	1.12e+10
$2s2p^5\ ^3P^o_1$	$2s^22p^4\ ^3P_0$	1.406e+10	1.00	1.6e+10^C	1.49e+10	1.451e+10	1.40e+10
$2s2p^5\ ^1P^o_1$	$2s^22p^4\ ^3P_0$	1.248e+09	1.02	1.6e+09^E	1.34e+09	1.281e+09	1.19e+09
$2s2p^5\ ^3P^o_2$	$2s^22p^4\ ^3P_1$	9.038e+09	0.99	1.04e+10^C	9.60e+09	9.383e+09	9.02e+09
$2s2p^5\ ^3P^o_1$	$2s^22p^4\ ^3P_1$	1.094e+10	1.00	1.26e+10^C	1.16e+10	1.133e+10	1.09e+10
$2s2p^5\ ^3P^o_0$	$2s^22p^4\ ^3P_1$	5.278e+10	1.00	6.05e+10^C	5.57e+10	5.445e+10	
$2s2p^5\ ^1P^o_1$	$2s^22p^4\ ^3P_1$	8.495e+08	1.03	9.3e+08^E	8.41e+08	8.436e+08	8.57e+08
$2s2p^5\ ^3P^o_2$	$2s^22p^4\ ^1D_2$	1.912e+09	0.97	2.2e+09^E	1.94e+09	1.935e+09	1.96e+09
$2s2p^5\ ^1P^o_1$	$2s^22p^4\ ^1D_2$	1.323e+11	1.00	1.49e+11^C	1.42e+11		1.32e+11
$2s2p^5\ ^3P^o_1$	$2s^22p^4\ ^1S_0$	5.970e+08	0.96	7.9e+08^E	6.35e+08	6.364e+08	5.86e+08
$2s2p^5\ ^1P^o_1$	$2s^22p^4\ ^1S_0$	9.591e+09	0.99	1.1e+10^C	1.03e+10	9.798e+09	
$2p^6\ ^1S_0$	$2s2p^5\ ^3P^o_1$	1.040e+10	1.03	1.2e+10^E	1.06e+10	1.026e+10	1.09e+10
$2p^6\ ^1S_0$	$2s2p^5\ ^1P^o_1$	1.358e+11	1.00	1.61e+11^C	1.50e+11	1.403e+11	1.35e+11
E2 transitions							
$2s^22p^4\ ^1D_2$	$2s^22p^4\ ^3P_2$	5.934e+00	1.04	6.00e+00^E	6.18e+00		
$2s^22p^4\ ^1S_0$	$2s^22p^4\ ^1D_2$	4.857e+01	1.07	4.9e+01^E	4.83e+01	4.889e+01	
M1 transitions							
$2s^22p^4\ ^3P_1$	$2s^22p^4\ ^3P_2$	1.449e+04		1.45e+04^C	1.42e+04		
$2s^22p^4\ ^1D_2$	$2s^22p^4\ ^3P_2$	1.693e+04		1.73e+04^C	1.69e+04	1.652e+04	
$2s^22p^4\ ^3P_1$	$2s^22p^4\ ^3P_0$	4.046e+01		4.0e+01^C		4.117e+01	
$2s^22p^4\ ^1D_2$	$2s^22p^4\ ^3P_1$	6.605e+02		6.70e+02^D	6.99e+02	6.320e+02	
$2s^22p^4\ ^1S_0$	$2s^22p^4\ ^3P_1$	1.398e+05		1.50e+05^C	1.39e+05	1.404e+05	
$2s2p^5\ ^3P^o_0$	$2s2p^5\ ^3P^o_1$	4.841e+03		4.82e+03^C		4.853e+03	
$2s2p^5\ ^1P^o_1$	$2s2p^5\ ^3P^o_1$	9.250e+03		9.40e+03^D		9.173e+03	
$2s2p^5\ ^1P^o_1$	$2s2p^5\ ^3P^o_0$	7.722e+03		7.70e+03^D		7.462e+03	

The ratings C, D, E in the $A_{\rm NIST}$ column refer to estimated accuracies for transition probabilities. C: $\leq 25\%$, D: $\leq 50\%$, E: $> 50\%$.

3.5.2 Summary

The full set of spectroscopic data for the levels of the $2s^2 2p^4$, $2s2p^5$, and $2p^6$ configurations in F II to Kr XXIX are computed using a fully relativistic configuration-interaction method and reported in [A4]. Our computed energies agree very well with the experimental values, with differences between 300 and 600 cm^{-1} for the majority of the ions in the sequence. Some possible problems with experimental identification of lines in As XXVI, Se XXVII, and Br XXVIII have been pointed out. The energy levels for these three spectra, presented in this paper, agree much better with the [116] values than with NIST databases (results for these ions are based on [115]). Our energy level calculations are considerably more accurate than other calculations (except for Vilkas and Ishikawa). There are excellent agreements with the most accurate MCHF-BP calculations at the low Z as well as with experimental lifetimes (Table 3.5.4). Basically, the calculations serve as benchmark calculations for transition probabilities for the $2s^2 2p^4$, $2s2p^5$, and $2p^6$ configurations of the oxygen-like sequence without the need for observed transition energies.

Chapter 4

Pecularities of spectroscopic properties of W^{24+} [A5]

Tungsten (W) will be a plasma wall material in the development of future tokamaks. Therefore, the data on spectral properties of its various ions are of great importance. Ions having simple electronic configurations of open shells are studied widely both experimentally and theoretically. This is not the case for ions with open f-shell, due to the large number of the energy levels. The use of the second quantization method in coupled tensorial form combined with quasispin technique, described in [124], opens the real possibilities to efficiently consider such configurations, as well.

4.1 Calculation method

We used different *ab initio* methods, namely MCHF and MCDHF approaches, taking into account relativistic and QED corrections [124]. The nonrelativistic configuration interaction method was used to include BP approximation and RCI method was used to include the transverse Breit interaction (B) at the low-frequency limit and the QED corrections [25, 21]. MCDHF calculations were performed with the GRASP2K relativistic atomic structure package [25, 26] in which for calculations of spin-angular parts of matrix elements the second quantization method in coupled tensorial form and the quasispin technique [124] were adopted. This allowed us to achieve a breakthrough in the field increasing the efficiency and speed of the calculations, thus opening the possibilities to consider extremely complex electronic configurations.

In case of the MCDHF expansions of the even and odd ASF for the energy spectrum calculations we used a MR set of CSFs based on the [Kr]$4d^{10}4f^4$ and [Kr]$4d^{10}4f^35p$ even as well as [Kr]$4d^{10}4f^35s$ and [Kr]$4d^94f^5$ odd configurations. The even and odd ASFs were calculated independently. The state func-

tions of these four configurations form the basis for the zero-order wave function (MR set). The energy functional on which the orbitals were optimized was defined according to EOL scheme [25], where a linear combination of atomic states, corresponding to the lowest two $J = 0, ..., 8$ states, were used (with the same scheme being used for the even and odd states). Admixed CSFs were obtained from single substitutions from all open-shell orbitals to an increasing AS of orbitals. The AS is labeled by an integer n and includes s, p, and d orbitals with principal quantum numbers up to n and f orbitals up to $n-1$. For example, the active set $AS_{n=6}$ contains s, p, and d orbitals with principal quantum number up to 6 and f orbitals up to $n = 5$. The active sets were successively extended to $n = 7$. At all steps only new orbitals were optimized.

4.2 Results

Figure 4.2.1 displays the computed energies of the 977 lowest levels of W^{24+} belonging to the [Kr]$4d^{10}4f^4$ (107 levels), [Kr]$4d^{10}4f^35s$ (82 levels), [Kr]$4d^{10}4f^35p$ (242 levels), and [Kr]$4d^94f^5$ (incomplete, 546 levels) configurations. The results presented are obtained in the both nonrelativistic and relativistic approaches. For the MCHF and CI calculations the ATSP2K package [24] was used. Figure 4.2.1 indicates that both (nonrelativistic and relativistic) approximations lead to a similar general picture of the energy spectra of the [Kr]$4d^{10}4f^4$ and [Kr]$4d^{10}4f^35s$ configurations. However, a detailed analysis of the data reveals the essential differences in the structure of the calculated energy spectra. Thus, for studies of the energy spectra, fine structure, electron transition probabilities, lifetimes, etc., of such ions, one must use already at the very beginning the relativistic approach.

The main peculiarity of the W^{24+} ion consists in the uniqueness of its ground configuration, containing only an open f shell, namely, $4f^4$. As we see from the calculations, the lowest excited state of this ion is $4f^35s$. Normally, electric dipole electronic transitions are allowed between the first excited and ground configuration. As a rule they are the strongest. In our case, however, such transitions are of octopole character. Quite unique are also the electronic transitions from the higher excited configuration to the ground configuration (quadrupole for $4f^35p - 4f^4$) or between the excited configurations (e.g., two-electron transitions).

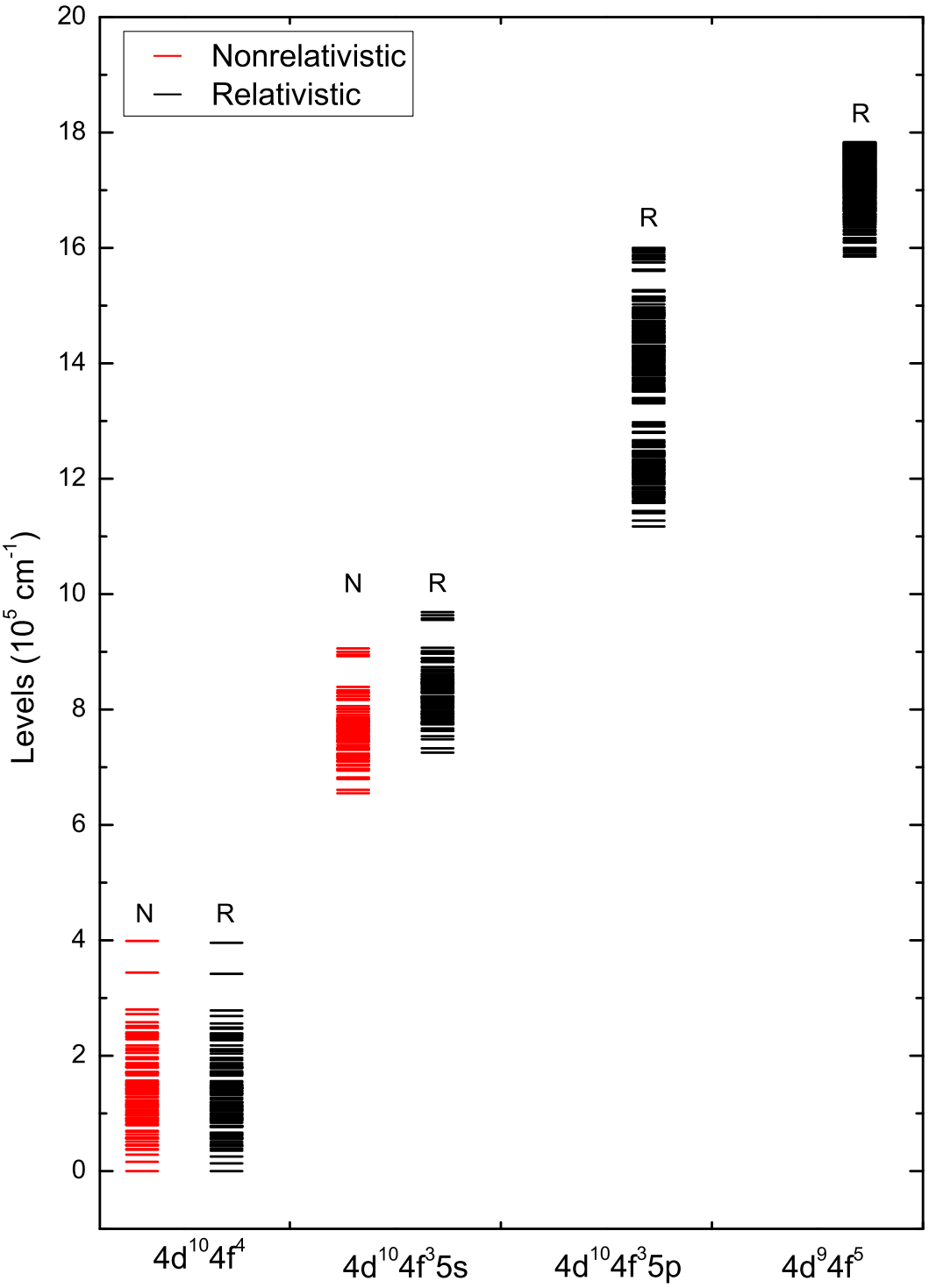

Figure 4.2.1: Configurations of W^{24+} in different approaches [MCHF+BP in red (N) and MCDF+B+QED in black (R)] with AS_7 expansion (single excitation).

The evaluation of the suitability of the $LS-$ and $jj-$couplings for the classification of energy spectra is performed using the methodic described in [125, 126]. Table 4.2.1 presents the square of the largest coefficient averaged over the states

(P_s) in the MCHF+BP and in the MCDHF+B+QED approaches. In the first case the energy levels are characterized by the quantum numbers of the $LS-$coupling whereas in the second one - by $jj-$coupling. The larger P_s value, the better is the coupling scheme. In ideal case P_s may reach 1. We were unable to find the P_s value for [Kr]$4d^{10}4f^35p$ in $LS-$ coupling. It follows from Table 4.2.1 that both coupling schemes are almost equally unsuitable and for the atomic states of these configurations it is important to use the intermediate coupling approximation. However, configuration mixing between investigated non-relativistic configurations is relatively week. Therefore, in case of the electric dipole (E1) electronic transitions, except of the exact selection rules $\Delta J = 0, \pm 1$ ($J = J' \neq 0$), $\Delta l = \pm 1$, the selection rules for the other quantum numbers are approximate.

Table 4.2.1: A square of the largest coefficient averaged over the states (P_s) in the MCHF+BP($LS-$coupling) and in the MCDHF+B+QED ($jj-$coupling) approaches.

Configuration	P_s	
	$LS-$coupling	$jj-$coupling
[Kr] $4d^{10}4f^4$	0.53	0.56
[Kr] $4d^{10}4f^35s$	0.54	0.52
[Kr] $4d^{10}4f^35p$		0.46

The E1 transitions have the largest probabilities. That is why one of the goals of this work is to study their peculiarities in W^{24+}. We can see from Figure 4.2.1 that the E1 transitions are allowed only between the levels of the excited configurations [Kr]$4d^{10}4f^35p$ and [Kr]$4d^{10}4f^35s$. For the calculations of the E1 transitions between initial even [Kr]$4d^{10}4f^35p$ and final odd [Kr]$4d^{10}4f^35s$ configurations we used single reference (SR) set. The even and odd ASFs were calculated independently. The E1 transition data (wavelengths, transition probabilities and line strengths) were calculated using the biorthogonal orbital transformations [19].

In Table 4.2.2 we present most probable transition probabilities (exceeding $6 \times 10^{10}(s^{-1})$) for spontaneous emission and line strengths of E1 transitions in both Babushkin (length) and Coulomb (velocity) gauges. Figure 4.2.2 presents the distribution of the transition probabilities for spontaneous emission A in s^{-1} of electric dipole transitions among the levels of [Kr]$4d^{10}4f^35p$ and [Kr]$4d^{10}4f^35s$ configurations in the Babushkin gauge with respect to their wavelengths. As

Table 4.2.2: Calculated wavelengths λ (in 10^2 Å), transition probabilities A (in 10^{10} s^{-1}) and line strengths S for the most probable (exceeding $6\times10^{10}(s^{-1})$) electric dipole transitions among the levels of [Kr]$4d^{10}4f^{3}5p$ and [Kr]$4d^{10}4f^{3}5s$ configurations. The notation w means position of level among the levels with the same total angular momentum quantum number J and $J\,\pi$ stands for the total angular momentum quantum number J and parity π (classification of the levels in $jj-$coupling).

Upper			Lower			λ	A (in 10^{10} s^{-1})		S	
Configuration	$J\,\pi$	w	Configuration	$J\,\pi$	w	(in 10^2 Å)	A_C	A_B	S_C	S_B
$4f_-^3(J=\frac{3}{2})5p$	0 +	9	$4f_-^3(J=\frac{3}{2})5s$	1 -	1	1.872645	6.722	6.942	0.218	0.225
$4f_-^2(J=2)4f(J_{12}=\frac{5}{2})5p$	0 +	10	$4f_-^2(J=2)4f(J_{12}=\frac{5}{2})5s$	1 -	2	1.885351	6.135	6.300	0.203	0.208
$4f^3(J=\frac{5}{2})5p$	1 +	29	$4f^3(J=\frac{5}{2})5s$	2 -	12	1.816095	6.849	7.018	0.607	0.622
$4f\_4f^2(J=0)5p$	1 +	30	$4f\_4f^2(J=0)5s$	2 -	13	1.790459	7.660	7.874	0.651	0.669
$4f^3(J=\frac{7}{2})5p$	2 +	50	$4f_-^2(J=0)4f(J_{12}=\frac{7}{2})5s$	3 -	12	1.814150	6.525	6.723	0.962	0.991
$4f^3(J=\frac{7}{2})5p$	2 +	52	$4f^3(J=\frac{7}{2})5s$	3 -	13	1.785163	6.296	6.493	0.884	0.912
$4f\_4f^2(J=0)5p$	4 +	59	$4f\_4f^2(J=0)5s$	3 -	14	1.823401	6.468	6.621	1.742	1.783
$4f_-^3(J=\frac{9}{2})5p$	3 +	26	$4f_-^3(J=\frac{9}{2})5s$	4 -	1	1.844713	6.896	7.155	1.496	1.552
$4f^3(J=\frac{7}{2})5p$	5 +	48	$4f^3(J=\frac{7}{2})5s$	4 -	14	1.830873	7.085	7.259	2.361	2.419
$4f_-^3(J=\frac{9}{2})5p$	6 +	22	$4f_-^3(J=\frac{9}{2})5s$	5 -	1	1.861758	6.084	6.233	2.519	2.581
$4f\_4f^2(J=2)(J_{12}=\frac{9}{2})5p$	6 +	39	$4f\_4f^2(J=2)(J_{12}=\frac{9}{2})5s$	5 -	12	1.836273	6.780	6.946	2.693	2.760
$4f_-^2(J=4)4f(J_{12}=\frac{11}{2})5p$	7 +	14	$4f_-^2(J=4)4f(J_{12}=\frac{11}{2})5s$	6 -	1	1.865237	6.235	6.358	2.996	3.054
$4f\_4f^2(J=6)(J_{12}=\frac{13}{2})5p$	8 +	12	$4f\_4f^2(J=6)(J_{12}=\frac{13}{2})5s$	7 -	1	1.867704	6.589	6.698	3.602	3.662
$4f\_4f^2(J=6)(J_{12}=\frac{15}{2})5p$	9 +	4	$4f\_4f^2(J=6)(J_{12}=\frac{15}{2})5s$	8 -	1	1.867316	7.108	7.202	4.340	4.397
$4f_-^2(J=4)4f(J_{12}=\frac{15}{2})5p$	9 +	5	$4f_-^2(J=4)4f(J_{12}=\frac{15}{2})5s$	8 -	2	1.848967	7.075	7.194	4.194	4.264
$4f\_4f^2(J=6)(J_{12}=\frac{17}{2})5p$	10 +	3	$4f\_4f^2(J=6)(J_{12}=\frac{17}{2})5s$	9 -	1	1.838271	7.329	7.458	4.718	4.802

seen from it, there are some transitions with probabilities significantly higher than others. The transition probabilities considered are in the time interval of $10^2\ s^{-1} - 10^{10}\ s^{-1}$. The largest transition rates are localized in two wavelengths intervals. The largest transitions are localized in the 170 Å – 198 Å domain. Transition probabilities, localized in the second domain (285 Å – 310 Å), are generally lower. These domains are of interest for thermonuclear plasma diagnostics.

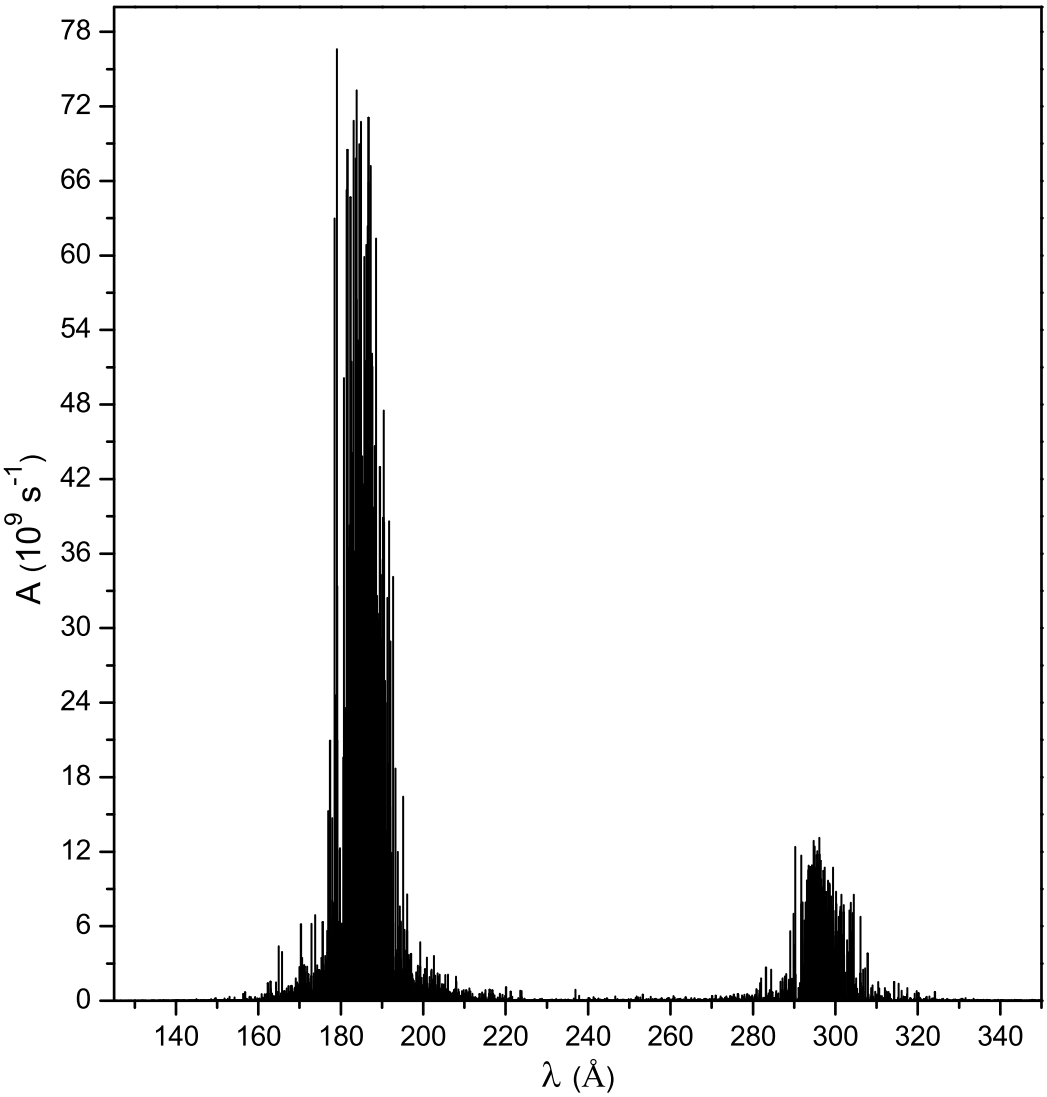

Figure 4.2.2: Theoretical emissions E1 transition probabilities in the MCDF+B+QED approach with AS_7 atomic state function expansion (single excitation) in Babushkin gauge.

In Table 4.2.3 the lifetimes of the 10 lowest excited levels belonging to the con-

figuration [Kr]$4d^{10}4f^{3}5p$ are presented in both Babushkin (length) and Coulomb (velocity) gauges [124]. The good agreement between the two gauges is seen. The lifetimes of the rest (higher) energy levels τ are similar to those presented in Table 4.2.3 and are of the order of $10^{-11}s$.

Table 4.2.3: Calculated lifetimes (in 10^{-11} s) of the 10 lowest excited levels belonging to the configuration [Kr]$4d^{10}4f^{3}5p$. The notations w mean positions of a level among the levels with the same total angular momentum quantum number J and $J\ \pi$ stands for the total angular momentum quantum number J and parity π (classification of the levels in $jj-$coupling).

Levels			τ (in 10^{-11}s)	
Configuration and coupling scheme	$J\ \pi$	w	τ_C	τ_B
$4d_-^4 4d^6 4f_-^3 (J=\frac{9}{2})\ 5p_-$	5 +	15	5.843	5.851
$4d_-^4 4d^6 4f_-^3 (J=\frac{9}{2})\ 5p_-$	4 +	20	5.634	5.533
$4d_-^4 4d^6 4f_-^2 (J=4)\ 4f(J_{12}=\frac{11}{2})\ 5p_-$	6 +	14	5.755	5.727
$4d_-^4 4d^6 4f_-^2 (J=4)\ 4f(J_{12}=\frac{11}{2})\ 5p_-$	5 +	16	5.698	5.582
$4d_-^4 4d^6 4f_-^3 (J=\frac{3}{2})\ 5p_-$	2 +	18	5.788	5.756
$4d_-^4 4d^6 4f_- 4f^2 (J=6)\ (J_{12}=\frac{13}{2})\ 5p_-$	7 +	8	5.730	5.679
$4d_-^4 4d^6 4f_-^3 (J=\frac{3}{2})\ 5p_-$	1 +	8	5.747	5.670
$4d_-^4 4d^6 4f_- 4f^2 (J=6)\ (J_{12}=\frac{13}{2})\ 5p_-$	6 +	15	5.654	5.512
$4d_-^4 4d^6 4f_-^2 (J=4)\ 4f(J_{12}=\frac{9}{2})\ 5p_-$	5 +	17	5.761	5.718
$4d_-^4 4d^6 4f_-^2 (J=4)\ 4f(J_{12}=\frac{9}{2})\ 5p_-$	4 +	21	5.725	5.631

4.3 Summary

The agreement between two gauges is within 2.5% for strong E1 transitions. For weak transitions the accuracy is lower. The weaknesses of a transition frequently comes out as a result of violations of selection rules, of cancellation between a number of large contributions or between different parts of the radial transition integrals. A small imbalance due to correlation effects may thus change the calculated transition probabilities dramatically. The results of Table 4.2.2 show that for every J value of the upper or lower configurations there are highly probable transitions.

The results of this work indicate that using the spin-angular integration method based on the second quantization in coupled tensorial form [124, 127] we can more efficiently study most complex electronic configurations of atoms and ions. In the particular case of W^{24+} ion it would be important to study magnetic

dipole and electric quadrupole electron transitions inside the ground configuration [Kr]$4d^{10}4f^4$, as well as the electric octopole and magnetic quadrupole electron transitions between the first excited configuration [Kr]$4d^{10}4f^3 5s$ and ground configuration [Kr]$4d^{10}4f^4$, because electric dipole transitions are strictly forbidden. Some of these transitions may be useful for the diagnostics of thermonuclear plasma.

Chapter 5

Applications of the PCFI method [A6-A8]

The PCFI method was previously applied for beryllium to calculate energies and specific mass shift parameters [128]. In sections below we will apply PCFI method for neutral lithium and neutral boron.

5.1 Lithium

The energy structure of Li-like systems make them suitable for accurate spectroscopic studies. Li-like ions are interesting for investigating the role of the correlation between the electrons. The consideration of three different properties, i.e. radiative transition probabilities, isotope shifts and hyperfine structures, makes it possible to probe the quality of the electronic wavefunctions in different parts of the configuration space. Transition probabilities and hyperfine structures have traditionally attracted a great deal of interest, and a number of accurate calculations have been performed. The isotope shifts are rather sensitive to electron correlation, and there are comparatively few calculations of high quality available in the literature.

Investigations of properties of neutral lithium provide excellent illustrations of how disagreement between theory and experiment leads to the development of new techniques that improve both theory and experiment.

5.1.1 The PCFI approach in lithium

For a deeper understanding of the ins and outs of the PCFI approach and fully appreciating its advantages, we moved to a smaller system: neutral lithium and its spectroscopic properties. For the lithium ground state, the Hartree-Fock approximation is rather good and the single reference ($m = 1$) $1s^2 2s\ ^2S$ can be taken. We apply the PCFI method using two ($p = 2$) PCFs: -i) the first one targets single and double excitations from the core ($1s$) orbital and is denoted $\Lambda_{1s-1s1s}$, - ii)

a second one, $\Lambda_{2s-1s2s}$, targets single excitations from the $2s$ valence shell and double excitations from the core ($1s$) and valence ($2s$) orbitals. The size of the PCFI matrix is small ($M = 3$). The wave-function for $1s^2 2s\ ^2S$ would be

$$|\Psi(1s^2 2s\ ^2S)\rangle = |\Psi^{\mathrm{SR}}(^2S)\rangle + \alpha_{\mathrm{CV}}\ |\Lambda_{2s-1s2s}\rangle + \alpha_{\mathrm{CC}}\ |\Lambda_{1s-1s1s}\rangle.$$

We compare the expectation values of other operators than the Hamiltonian, i.e. the specific mass shift and the hyperfine interaction parameters,evaluated by the two SD-(SR)-PCFI and SD-(SR)-MCHF methods in figure 5.1.1. The two curves illustrate the impact of the "constraint effect" on three different properties: the total energy, the specific mass shift (S_{sms}) and the contact term (a_{cont}).

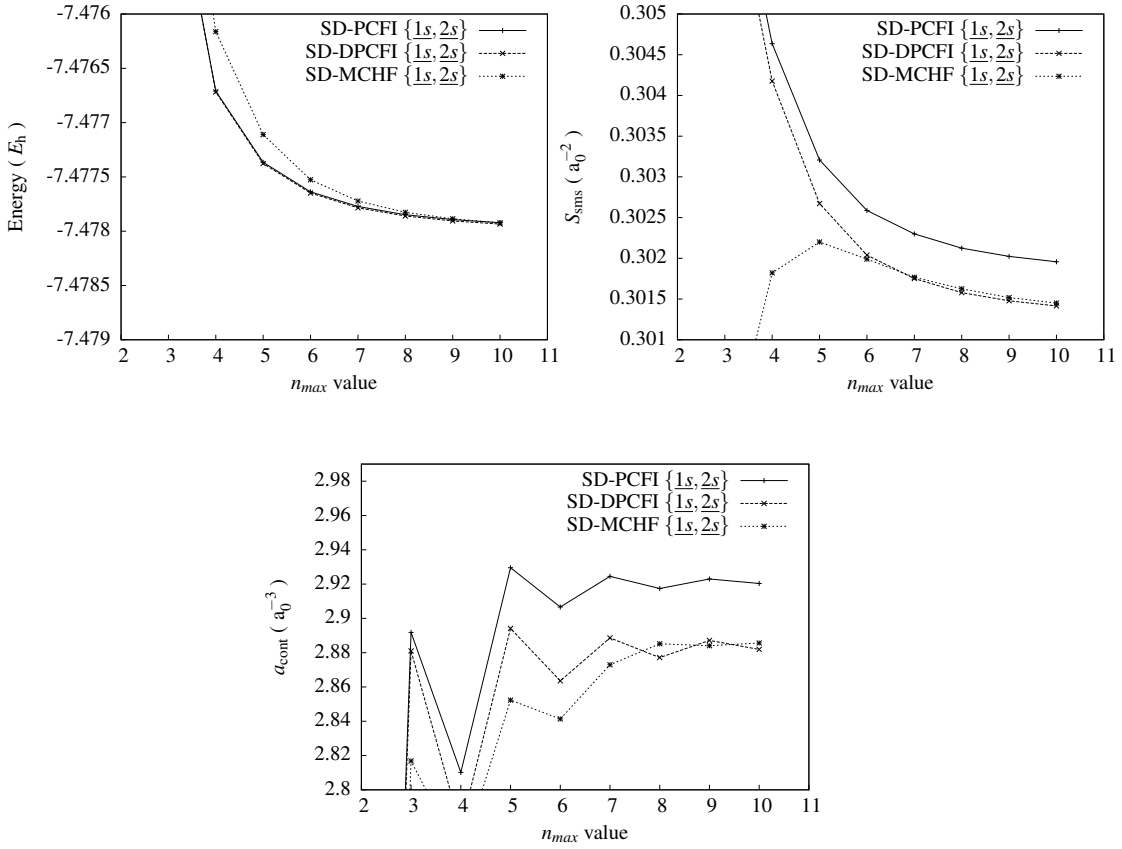

Figure 5.1.1: Convergence of the absolute total energy, the specific mass shift and the hyperfine contact parameters for the ground state of neutral lithium. The agreement found between the SD-MCHF and SD-PCFI curves for the total energy is not observed for the two other properties. We recover the consistency with the traditional method by deconstraining the wave function (SD-DPCFI).

As mentioned in the end of the section on the PCFI method 2.8 the origin of this effect is the hindrance to free variation in the expansion coefficients and in the orbitals. Even if the pre-optimized PCF orbital sets are fixed in the PCFI diagonalization step, the associated orbital constraint effect is expected to be small in comparison to the constraint on the mixing coefficients. The lack of variation in the orbitals is indeed somewhat compensated by the use of separated PCF orbital sets that makes the number of radial functions for a given active set, larger in the PCFI approach than in the MCHF method. Moreover the number of correlation layers used for a given PCF is probably large enough to reach saturation. The strongest limitation is likely to come from the fact that for each PCF, the mixing coefficients appearing in (2.8.7) are kept frozen in the interaction step that leads to the final many-electron wave function expression (2.8.4). By freezing these mixing coefficients, we inhibit the expression of any indirect effects. The relative weights of the CSFs within each PCF are indeed already fixed by the frozen coefficients $\{c_j^{\Lambda}\}$ obtained from each independent MR-PCF MCHF optimization of (2.8.3), each one targeting a specific correlation component, and no possibility is offered to these coefficients to capture the higher-order PCF-coupling effects.

5.1.2 The CAS-DPCFI approach in lithium

In this section we present results obtained for selected spectroscopic properties involving the ground state of neutral lithium, ie. $1s^2 2s\ ^2S$. The Li I ground state (D)PCFI calculations that were presented in above and figure 5.1.1 to investigate the constraint effect are limited in the sense that triple excitations are systematically omitted in a SD-single-reference calculation. In order to obtain more accurate many-electron wave functions, we adopted the complete active space list of CSFs combined with the DPCFI approach that remains manageable for a three-electron system. For illustrating the great flexibility of the DPCFI approach, we investigate two different strategies - i) treating core excitations globally and ii) separating the single and double core-excitations and dedicating a PCF to core-polarization.

A global core description

As in our first model, we use the Hartree-Fock (HF) solution as the zeroth-order wave function for the ground state of this three electron system. In this approach, we split the CF space made of single, double and triple excitations (SDT) in three different subspaces ($p = 3$) defining the following three PCFs:

- one for taking care of the inner-shell correlation between the two $1s$ electrons

$$|\Lambda_{1s-1s1s}\rangle = |1s^2 2s\ ^2S\rangle + \sum_{n'l'} |1s2s\ n'l'\ ^2S\rangle + \sum_{n'l',n''l''} |2s\ n'l'n''l''\ ^2S\rangle\ , \quad (5.1.1)$$

- a second one associated to the inter-shell correlation between the $1s$ and the $2s$

$$|\Lambda_{2s-1s2s}\rangle = |1s^2 2s\ ^2S\rangle + \sum_{n'l'} |1s^2\ n'l'\ ^2S\rangle + \sum_{n'l',n''l''} |1s\ n'l'n''l''\ ^2S\rangle\ , \quad (5.1.2)$$

- a third and last one including the pure triple excitations

$$|\Lambda_{1s1s2s}\rangle = |1s^2 2s\ ^2S\rangle + \sum_{n'l',n''l'',n'''l'''} |n'l'n''l''n'''l'''\ ^2S\rangle\ . \quad (5.1.3)$$

For the first two PCFs (5.1.1) and (5.1.2), we optimize all the correlation orbitals, freezing the $1s$ and $2s$ to the HF solution of the single-reference. This strategy is inadequate for Λ_{1s1s2s} since it only contains triple excitations that do not interact with the reference CSF. The optimization of the corresponding orbital set becomes then more tricky. In the previous paper [128], we chose to use a SD-multireference to include triple excitations. In the present work, we dedicate a specific PCF to these. We first define an "extended" SD expansion for a reference set built on the $(n = 2,3)$ shells and optimize it by allowing variations in the correlation orbitals only. This expansion opens an indirect interaction between the triple excitations and the reference CSF. For capturing these higher-order effects, we strictly optimize the $n > 3$ orbitals during the MR-PCF procedure. The $n = 4$ layer is therefore the first one that effectively represents three-electron

excitations. Figure 5.1.2 illustrates for the ground state that the DPCFI convergence is faster than the traditional CAS-MCHF approach based on the same CSF expansions. For a given orbital active set, the corresponding total energy value is indeed systematically below the CAS-MCHF result. Since the angular content of the wave function (maximum l-value for in the one-electron basis) is identical for both methods, we conclude that the DPCFI method captures more efficiently electronic correlation for a given atomic system. A similar improvement is a

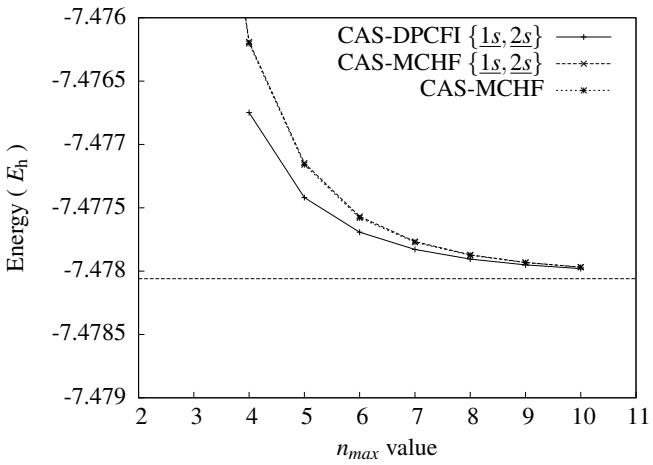

Figure 5.1.2: Convergence of the total energy with respect of the maximal principal quantum number for the ground state of lithium. The reference values (the dotted lines) correspond to the absolute energy values obtained by Yan *et al.* [129].

priori expected for any other spectroscopic property. Figure 5.1.3 presents the convergence pattern of the contact term for the ground state of neutral lithium. As it clearly appears, the hyperfine parameters are not converging as smoothly as the total energy. It is well known that the relevant expectation values are extremely sensitive to single excitations and it is worthwhile to attempt another approach for treating this excitation family independently.

A Partitioned Correlation Function dedicated to core-polarization

For describing more accurately the hyperfine interaction, we split the $\Lambda_{1s-1s1s}$ PCF in two subspaces

$$\Lambda_{1s-1s1s} \rightarrow \Lambda_{1s} + \Lambda_{1s1s} \, . \tag{5.1.4}$$

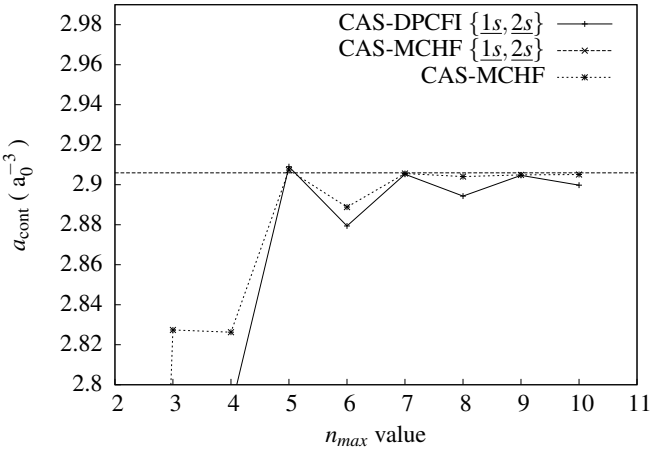

Figure 5.1.3: Convergence of the contact term of the ground state with respect of the maximal principal quantum number. The reference value for the contact term (the dotted line) corresponds to the value obtained by Yan *et al.* [130].

The Λ_{1s} PCF function focusing on the single excitations is dedicated to capture core-polarization effects. The many-electron wave function is then written as the reference function corrected by four ($p = 4$) different PCFs with their own orbital set: the two first, associated to the core-valence (5.1.2) and to the triple excitations (5.1.3), as described in the previous subsection, completed by

- a third one that takes care of the single excitations of the $1s$ shell

$$|\Lambda_{1s}\rangle \;=\; |1s^2 2s\ ^2S\rangle + \sum_{n'l'} |1s2s\ n'l'\ ^2S\rangle\ , \tag{5.1.5}$$

- a last one associated to the double excitations of the $1s$ shell

$$|\Lambda_{1s1s}\rangle \;=\; |1s^2 2s\ ^2S\rangle + \sum_{n'l',n''l''} |2s\ n'l'n''l''\ ^2S\rangle\ . \tag{5.1.6}$$

Excitations considered in (5.1.5) describe spin-polarization, for the ^2S state, since single excitations can break the singlet spin coupling between the two core electrons. It is well known that the hyperfine parameters are sensitive to these excitations and some improvement is expected in their evaluation thanks to the splitting (5.1.4). The results are presented in figures 5.1.4 and 5.1.5. By comparing figures 5.1.2 and 5.1.4, it is obvious that the decomposition (5.1.4) does not affect the total energy value. The DPCFI method still captures correlation more

efficiently than the traditional MCHF calculations. The interesting improvement appears for the hyperfine parameters. Figure 5.1.5 illustrate their progressive convergence for the ground state. The use of the orbital set tailored for capturing the spin- and orbital core-polarization enhanced beautifully the convergence pattern of all the hyperfine parameters. The resulting trends are much smoother than those of the global core approach and the ordinary MCHF (see figure 5.1.3). All oscillations disappeared and we reach reasonably well-converged values around $n = 5$. Lithium is a small atom and it is possible to enlarge an ordinary orbital basis to get converged values for all quantities. For larger atoms with more complicated shell structures it is, to set things into perspective, often not possible to extend the radial orbital basis very much due to a rapidly growing number of CSFs and here the fast convergence of the CV-DPCFI method, together with the fact that orbital sets for different shells can be optimized independently of each other, represents a *major* improvement in the general methodology.

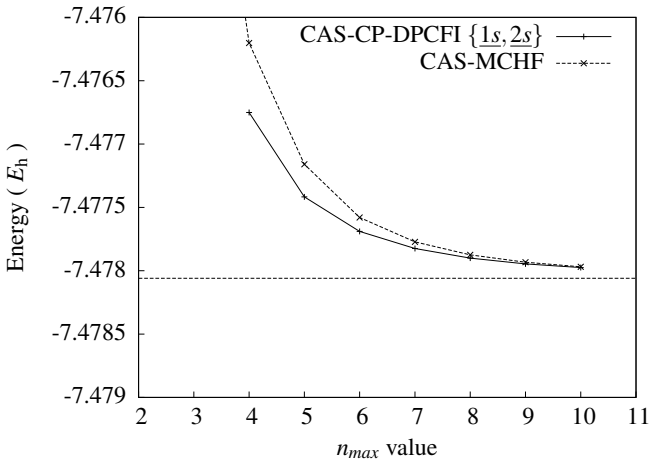

Figure 5.1.4: Convergence of the absolute energy with respect of the maximal principal quantum number for ground state. The reference values (the dotted line) correspond to the results obtained by Yan *et al.* [129].

The values of the corresponding total energies, S_{sms} and hyperfine parameters are reported in table 5.1.1. As in the figures, we compare the DPCFI values with Yan *et al.* [129, 130] results using a Hylleraas-type variational method. The remaining difference between both studies may be attributed to the slow angular

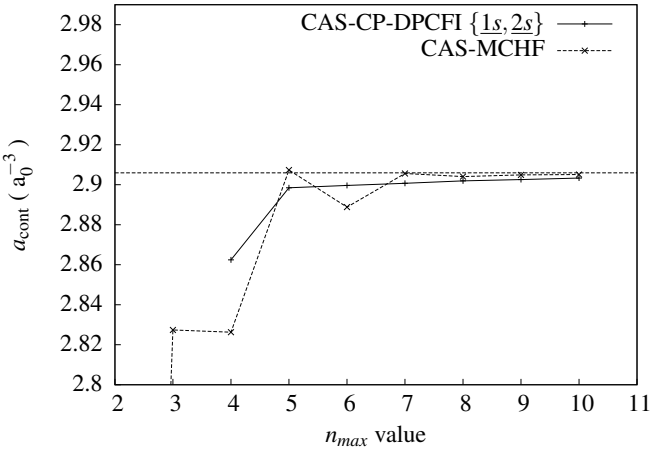

Figure 5.1.5: Convergence of the contact term of the hyperfine interaction with respect of the maximal principal quantum number for the ground state of lithium. The reference values (the dotted line) correspond to the results obtained by Yan *et al.* [130].

convergence rate ($E_l - E_{l-1} = \mathscr{O}(l+1/2)^{-4}$) of the $(1/r_{12})$ angular development.

Table 5.1.1: Energies, S_{sms} and a_{cont} for an increasing maximum principal quantum number for the ground state of Li.

CAS-CP-DPCFI $\{\underline{1s}, \underline{2s}\}$ to the HF solution			
n_{max}	Energy (a.u.)	S_{sms}	a_{cont}
HF	−7.432726927	0.000000000	2.0932317
4	−7.476750919	0.304445112	2.8624693
5	−7.477417364	0.303171470	2.8984561
6	−7.477689394	0.302588400	2.8996669
7	−7.477824739	0.302322528	2.9007289
8	−7.477900177	0.302162573	2.9019278
9	−7.477946240	0.302062836	2.9025948
10	−7.477975286	0.302006041	2.9033303
Yan *et al.* [129, 130]	−7.47806032310(31)	0.301842809(15)	2.905922(50)

5.2 Neutral Boron

Since no intercombination lines are observed in B I the position of the quartets relative to the ground state is obtained from extrapolation along the iso-electronic sequence. Edlén et al. [131] estimated the energy difference $2s^2 2p\ ^2P^o_{3/2}$ – $2s2p^2\ ^4P_{5/2}$ to be 28866 ± 15 cm^{-1}. Recently, Kramida and Ryabtsev [132], using an extended set of experimental data, revised the estimate to 28643.11 + x cm^{-1} with an uncertainty of 1.8 cm^{-1}, where x represents the error in the extrapolation. The difference in the two extrapolated values is 223 cm^{-1}. Breit-Pauli calculations for the boron-like isoelectronic sequence have been reported [133]. For B I, C II, and N III the ^4P levels were too high relative to ASD values [64] by (0.53, 0.13, 0.10) %. With the suggested revision, the error in B I would increase to 1.3 % or 277 cm^{-1}.

Boron is a relatively light atom in which the fine-structure splitting is small and the spin-orbit interaction between LS terms is negligible. The previous calculation [133] was intended as a Breit-Pauli calculation for the iso-electronic sequence, with the neutral atom not the element of prime concern. In particular, correlation in the core was omitted since its contribution to the wavefunction in the outer region of the atom decreases rapidly along the iso-electronic sequence. With current computers it is possible to estimate the value of x from non-relativistic calculations that include the efffects of correlation and the non-fine structure relativistic corrections.

In this work we report the results of calculations for the $2s^2 2p\ ^2P^o_{3/2}$ – $2s2p^2\ ^4P_{5/2}$ excitation energy, both in the MCHF+BP method tailored to the neutral atom, and results from PCFI [128]. Relativistic and finite mass corrections are included. Accuracy is estimated and validated by similar calculations for C II where experimental data are available.

5.2.1 MCHF method and results

In this work, systematic calculations were performed in which the orbital basis was increased from one calculation to the next by increasing the maximum principal quantum number n, thereby introducing a new "layer" of orbitals. This parameter n characterizes the calculation. MCHF calculations up to $n = 10$ were performed with orbital quantum numbers up to $l = 5$ (h-orbitals).

The computational model determines the CSF space for each orbital set. The

LSGEN program was used to generate all CSFs that differ by one or more electrons from a given configuration and are of the same parity and *LS* quantum number. Such substitutions are referred to as single- (S), double- (D), etc. excitations. For open-shell systems, SD excitations from a single configuration are not sufficient, as shown for the Be ground state [128]. On the other hand, a CAS expansion for which the number of excitations equals the number of electrons, soon becomes impractical as the orbital set increases. Here we have used a method, referred to as MR-SD, that starts with a MR of CSFs that includes the CSF for the state and any others that may be important. Then SD expansions are obtained by applying the process to each member of the MR set.

Ideally, the MR set should contain all the important CSFs of the final wave function. An indication of these CSFs can be obtained from a small MCHF calculation, such as an MCHF calculation for an $n = 3$ SD expansion. Those with small expansion coefficients can be omitted, but as more correlation is added, others may gain importance. In the present work, the default MR sets are:

$$\begin{aligned} {}^2P^o \;&:\; 2s^2 2p, 2p^3, 2s2p3d, 2s^2 3p, 2s3s3p, 2p^2 3p, 2p3s^2, \\ &\quad\; 2p3d^2, 2s2p3s; \\ {}^4P \;&:\; 2s2p^2, 2s2p3p, 2p^2 3d, 2s3d^2, 2s3p^2, 2p3s3p, 2p^2 3s. \end{aligned} \tag{5.2.1}$$

In the final wave function, the smallest expansion coefficient was about 0.025 in magnitude, accounting for ≈ 0.06 % of the eigenvector composition.

The present two states of interest have a common $1s^2$ core and three valence electrons. The substitution of one or two valence orbitals by other orbitals defines valence-valence (VV) correlation, substitution of a single $1s$ orbital and possibly also one valence orbital defines core-valence (CV) correlation, and substitution of the two $1s$ orbitals defines core-core (CC) correlation. Correlation in the core essentially cancels in the calculation of an energy difference, but it may be large. Therefore small differences may contribute significantly to the energy separation. In order to maintain this balance at intermediate stages, prior to convergence, the variational principle was applied to the sum of energy functionals for each state, referred to as simultaneous optimization. Since both states are lowest in their symmetry, the sum of the energies is also a minimum. In this way, the same orbitals were used in the calculation of the core of both states and the optimization process minimized the combined energy.

Table 5.2.1 shows the variation of the ${}^2P^o$ - ${}^4P$ excitation energy for two dif-

ferent computational strategies using the MCHF method in which all orbitals are optimized unless specified to the contrary.

Table 5.2.1: Comparison of the $2s^2 2p\ ^2P^o$ – $2s2p^2\ ^4P$ excitation energy, ΔE in cm^{-1} and the total energies E (in E_h) for various computational strategies (see text for details). The number of CSFs, N, corresponding to the largest active set ($10h$) wave functions for the $^2P^o$ and ^4P terms are given at the end of the table.

n	$E\ (^2P^o)$	$E\ (^4P)$	ΔE
	independent		
4	−24.639611871	−24.510683384	28296.53
5	−24.646858826	−24.517481734	28394.99
6	−24.650292338	−24.519781873	28643.74
$7h$	−24.651852635	−24.520806644	28761.27
$8h$	−24.652552770	−24.521246474	28818.40
$9h$	−24.652880597	−24.521452001	28845.24
$10h$	−24.653049725	−24.521555084	28859.74
N	101 472	68 558	
	simultaneous		
4	−24.639619089	−24.509994715	28449.26
5	−24.646817680	−24.517094023	28471.05
6	−24.650320310	−24.519604775	28688.74
$7h$	−24.651845860	−24.520717113	28779.43
$8h$	−24.652512201	−24.521187717	28822.39
$9h$	−24.652849227	−24.521400399	28849.68
$10h$	−24.653024991	−24.521518982	28862.23
N	101 472	68 558	

In the *independent* strategy the wave function for each state is calculated independently in a single orthonormal orbital basis that then describes all three types of correlation. As shown previously [128], the orbitals for VV correlation will have a maximum in the outer region of the atom, the CV orbitals are in the regions of overlap between $1s$ and $2s$ or $2p$, and CC is in the region of the $1s$ orbital. At each stage of a systematic calculation, the orbitals arrange themselves so as to minimize the energy and, in going from one layer to the next, considerable rearrangements may occur. If the rearrangements of the orbitals in the two independent calculations are not similar at an intermediate stage, an imbalance *may* occur in the difference.

In the *simultaneous* strategy the variational procedure is applied to the sum of the two energies so that the same orbitals are used to describe both wave functions. In particular, the more dynamic CC correlation is described in terms

of the same orbitals. Table 5.2.1 shows that, with the same MR-SD expansion, the simultaneous optimization method closely tracks calculation of independent strategy, although the excitation energy is somewhat larger. No large differences were found, even though the total energy of the ^4P was raised more than that of $^2P^o$, thereby increasing ΔE, but the difference decreased with n.

Table 5.2.1 also specifies the size (N) of the ($10h$) wave function expansions for each calculation. This table clearly indicates that the correct excitation energy is closer to the Edlén *et al.* value than the Kramida and Ryabtsev one.

Extending the MCHF method to higher accuracy would require a rather large set of orthonormal orbitals since orbitals with higher angular quantum numbers should also be included. An alternative is to introduce the use of non-orthogonal orbitals.

5.2.2 PCFI method and results

In PCFI method the correction to the wave function for three types of correlation is a linear combination of partitioned correlation functions (PCF's), denoted by Λ_i, so that

$$\Psi_1 = \alpha_1\Lambda_1 + \alpha_2\Lambda_2 + \alpha_3\Lambda_3. \tag{5.2.2}$$

Each Λ_i is itself a linear combination of CSF's, where the expansion coefficients and the orbitals are an MCHF solution for the wave function $\Psi_0 + \Lambda_i$, with the orbitals of Ψ_0 fixed. Because the MCHF method requires a single orthonormal basis, the new orbitals for each partition Λ_i must be orthogonal to the orbitals defining Ψ_0, but may be non-orthogonal to those from other partitions. For the present case, the partitions represent VV, CV, and CC correlation corrections, respectively. Biorthogonal methods are then used to compute the interaction matrix in a non-orthogonal basis for a wave function expanded in the CSF basis defining Ψ_0, and the partitions, $\Lambda_1, \Lambda_2, \Lambda_3$. Some variational freedom is lost by this method since the expansion coefficients for each partition can now only be scaled by a constant factor. In order to recover this freedom, a de-constraining procedure may be applied in which, when forming the PCFI configuration interaction matrix, a configuration state function is moved from a partition into the set defining Ψ_0.

Non-relativistic Calculations for Boron

The same MR sets as used for the MCHF study were adopted. Applying the SD process to each set, the resulting expansions were classified according to the occupation number of the 1s-shell. For each state, the next step was to obtain the orbitals for Ψ_0. Keeping these orbitals frozen, MCHF calculations were performed for each of their three partitions. Because the orbital basis now targets the same type of correlation, there is less rearrangement of orbitals as new layers of orbitals are added, so that convergence is better and calculations can readily be extended to $n = 10$ without any truncation of the angular quantum numbers.

Using the resulting PCFs, the configuration interaction matrix was built. Table 5.2.2 displays the total energies and excitation energy calculated with the original constrained representation of each PCF. The energies of the $n = 10$ results are significantly lower than the MCHF results of Table 5.2.1.

To check the sensitivity of the excitation energy to the constraint effect, we also report results from the DPCFI method where all the expansion coefficients are free to vary. The modified excitation energy is included in Table 5.2.2 in the last column and denoted as ΔE(D). The final total energies and excitation energy are presented as $n = 10D$ results. From these data we see that the deconstraint increases the excitation energy by 6.39 cm^{-1}. The changes are small but bring the total energy into better agreement with the "exact" non-relativistic energy [134] for the ground state.

Table 5.2.2: Non-relativistic total energies E (in E_h) and excitation energy, ΔE in cm^{-1}, of the lowest $^2P^o$ and ^4P terms of neutral boron obtained with the PCFI and DPCFI method. The total energies for a DPCFI calculation are reported as 10D and the excitation energy as $\Delta E(D)$.

n	E ($^2P^o$)	E (^4P)	ΔE	ΔE(D)
4	−24.644046909	−24.514398526	28454.53	28457.66
5	−24.650782918	−24.519740851	28760.40	28765.41
6	−24.652391314	−24.520979432	28841.57	28847.00
7	−24.652978136	−24.521441671	28868.91	28875.86
8	−24.653244882	−24.521636963	28884.59	28890.74
9	−24.653383550	−24.521735733	28893.35	28899.63
10	−24.653464335	−24.521792201	28898.69	28905.08
10D	−24.653523595	−24.521822334		28905.08
E^{exact}[134]	−24.65393			

The effect of increasing the MR set was also evaluated, using the CAS concept for a valence correlation expansion of Ψ_0 for each of the two states, namely

$$\begin{aligned} 1s^2 2s^2 2p\ ^2P^o: &\qquad 1s^2\{2s,2p,3s,3p,3d\}^3\ ^2P^o \\ 1s^2 2s 2p^2\ ^4P: &\qquad 1s^2\{2s,2p,3s,3p,3d\}^3\ ^4P\ . \end{aligned} \tag{5.2.3}$$

This notation represents an expansion over CSFs from configurations with a $1s^2$ core and three orbitals of the required symmetry and parity for the given list of orbitals. The MR expansions contain 30 and 13 CSFs for the odd and even parity, respectively. Allowing single and double excitations from these CSFs we get the CSF space that was partitioned into the three PCFs (VV, CV, and CC). The expansion size grows rapidly – 242,532 and 175,542 for $^2P^o$ and ^4P, respectively for $n = 9$ and 357,230 and 258,565 for $n = 10$. However, partitioning the expansion into three parts, the final size is computationally feasible.

Systematic calculations can be improved through extrapolation of trends to $n = \infty$ which in our procedure also implies $l = \infty$. To perform the extrapolation, we consider the change in energy (or excitation energy) $\delta E_9 = E_9 - E_8$ and $\delta E_{10} = E_{10} - E_9$ to determine the rate of convergence :

$$r = \delta E_{10}/\delta E_9\ . \tag{5.2.4}$$

If we assume that the convergence continues at the same rate for the rest of the sequence, the remainder is a geometric series that can be summed to yield

$$\sum_{i=1}^{\infty} \delta E_{10}\, r^i = \delta E_{10}\, \frac{r}{1-r} \qquad \text{if } |r| < 1\ , \tag{5.2.5}$$

In fact, the ratio increases with n because of the slow convergence of contributions from the higher angular momenta.

Relativistic and Finite Mass corrections

For a light atom, relativistic effects can be accurately estimated in the Breit-Pauli approximation. The terms of the Breit-Pauli operator can be classified into the J-dependent fine-structure (FS) and LS-dependent relativistic shift (RS) contributions. For boron, the latter are the more important corrections and were easily included in this extensive calculation.

Table 5.2.3 presents the total energies of each state as well as the excitation

energies obtained using the PCFI method with a Hamiltonian including the relativistic shift operators. For the purpose of comparison, excitation energies from the smaller calculations of Table 5.2.2 that also include the relativistic shift operators are reported in the last column and are denoted as ΔE(S). The increase in the excitation energy is 2.26 cm^{-1}. The RS contribution to the doublet-quartet excitation energy is estimated to be the difference between the $n = 10$ values of 28942.06 ($\Delta E(S)$ of Table 5.2.3) and 28898.69 (ΔE of Table 5.2.2), or 43.37 cm^{-1}.

Table 5.2.3: PCFI total energies, E in E_h, and excitation energy, ΔE in cm^{-1} including the relativistic shift operator, of the lowest $^2P^o$ and ^4P terms of neutral boron. The MR set included all CSFs of $1s^2\{2s,2p,3s,3p,3d\}^3$ of the required symmetry and parity. ΔE(S) refers to the excitation energy including the relativistic shift operator from calculations with the smaller MR of Table II. N is the size of the $n = 10$ CSF expansion.

n	E ($^2P^o$)	E (^4P)	ΔE	ΔE(S)
4	−24.650382640	−24.520438740	28519.38	28496.83
5	−24.657117561	−24.525847143	28810.52	28803.21
6	−24.658725942	−24.527084872	28891.87	28885.02
7	−24.659297417	−24.527551340	28914.92	28912.18
8	−24.659568315	−24.527751544	28930.43	28927.90
9	−24.659709842	−24.527853807	28939.05	28936.71
10	−24.659792829	−24.527912772	28944.32	28942.06
∞	−24.659910	−24.527993	28952.52	
N	357 230	258 565		

Table 5.2.4 reports the excitation energy using the complete Breit-Pauli Hamiltonian within the PCFI approach. *LS*-term mixing of different terms is omitted. Substracting the ΔE(S) values reported in Table 5.2.3 from the Breit-Pauli ΔE values of Table 5.2.4, we get an estimate of the importance of the *LS* diagonal fine structure operators, i.e. -0.74 cm^{-1}. Comparing the ΔE and $\Delta E(D)$ values in Table 5.2.4 reveals the constraint effect on the excitation energy in the BP approximation, i.e. 7.05 cm^{-1}, which differs somewhat from the earlier estimate of 6.39 cm^{-1}. The difference of 0.66 cm^{-1} is small and establishes a lower limit on the uncertainty of our computational procedure.

The finite-mass correction should also be considered. The normal mass (NMS) correction can readily be determined from the Bohr mass scaling law, using the finite-mass Rydberg constant. This reduces the excitation energy by -1.59 cm^{-1}

Table 5.2.4: Breit-Pauli total energies, E in E_h, and corresponding excitation energy, ΔE in cm^{-1}, of the lowest $^2P^o_{3/2}$ and $^4P_{5/2}$ levels of neutral boron using both the PCFI and DPCFI methods.

n	$E(^2P^o_{3/2})$	$E(^4P_{5/2})$	ΔE	ΔE(D)
4	−24.650251936	−24.520414146	28496.10	28499.14
5	−24.657033103	−24.525799428	28802.46	28807.83
6	−24.658656372	−24.527049905	28884.28	28890.09
7	−24.659251843	−24.527521599	28911.44	28918.01
8	−24.659523392	−24.527721520	28927.16	28933.87
9	−24.659666371	−24.527824368	28935.97	28942.94
10	−24.659749687	−24.527883327	28941.32	28948.37
∞			28949.56	28956.47
10D	−24.659913687	−24.528015185		28948.37

and -1.44 cm^{-1} for ^{10}B and ^{11}B, respectively. However, for the excitation energy under consideration the specific mass shift is larger than expected. Using the $n = 10$ PCFI wave functions for estimating the ΔS_{sms} difference of the specific mass shift parameters [135], the finite mass (NMS+SMS) corrections are:

^{10}B: -6.67 cm^{-1} and ^{11}B: -6.07 cm^{-1} .

The de-constraint correction on ΔS_{sms} is very small and an average over the two isotopes based on the natural isotopic composition (19.9% ^{10}B/80.1% ^{11}B) gives a final estimation of -6.20 cm^{-1}. This correction is therefore important for spectroscopic accuracy.

The C II quartet-doublet energy separation

In order to estimate the errors not accounted for, mainly the contributions from orbitals with high-angular quantum numbers, we validate our method by applying it to the calculation of the excitation energy in C II where the wavelength of the $^2P^o_{3/2}$ - $^4P_{5/2}$ transition has been measured recently by Young *et al.* [136] and ASD [64] values are available.

For maximum accuracy we start with the valence CAS expansion to determine Ψ_0 and then the PCFs for the three types of correlation. In generating the configuration interaction matrix we used the Breit-Pauli Hamiltonian but with only the relativistic shift operators, because of the size of the expansion and the small effect from the J-dependent terms.

Table 5.2.5 reports the results for C II. Because of the large expansions, de-constrained DPCFI excitation energies are not included for the higher layers, but the effects of de-constraining closely track those of Table 5.2.4 where the

Table 5.2.5: Total energies, E in E_h, and excitation energy, ΔE in cm^{-1} including the relativistic shift operator, of the lowest $^2P^o$ and ^4P terms of the singly ionized carbon atom obtained using the PCFI method as well as some DPCFI excitation energies. Observed data have been obtained from an *LS* spectrum (see text).

n	$E(^2P^o)$	$E(^4P)$	ΔE	$\Delta E(D)$
4	−37.434442461	−37.241016132	42452.17	42454.33
5	−37.441661608	−37.246648961	42800.32	42804.62
6	−37.443459176	−37.247990596	42900.39	42905.57
7	−37.444132978	−37.248491723	42938.29	42944.35
8	−37.444453444	−37.248717425	42959.09	
9	−37.444620358	−37.248830141	42970.98	
10	−37.444721702	−37.248898421	42978.24	
∞	−37.444878	−37.249003	42989.59	
De-constraint			7.05	
Finite Mass			−10.22	
Excitation Energy			42986.42	
Young *et al.* [136]			42993.0 ± 0.9	
ASD [64]			42993.5	

final difference was 7.05 cm^{-1}. The finite mass correction for an isotopically-unresolved line profile, is largely dominated by the lighest isotope (98.93% ^{12}C/1.07% ^{13}C) and is estimated to be −10.22 cm^{-1}. Correcting the extrapolated $n = 10$ results in Table 5.2.5 by these amounts we get 42986.42 cm^{-1}. Comparing this value with excitation energies derived from observed data by defining each term energy to be the statistically weighted average of the levels of the term, we get a remainder of 6.58 cm^{-1} representing residual correlation and other omitted effects that were not captured in our calculation for C II.

5.2.3 Final estimate for the $^2P^o_{3/2}$ – $^4P_{5/2}$ excitation energy in B I

The results of our investigation of the various aspects of the PCFI method as applied to the $2s^22p\ ^2P^o_{3/2}$ – $2s2p^2\ ^4P_{5/2}$ excitation energy are summarized in Table 5.2.6. Listed are the contributions to the energy starting with the non-relativistic PCFI value of Table 5.2.2 based on the small MR list. Since the corrections are small, values of contributions were obtained by expressing the $n = 10$ excitation energies of Tables 5.2.3 - 5.2.4 in terms of the PCFI value and contributions, assuming a first-order theory.

As mentioned earlier, in some instances, a contribution (such as D) could have two slightly different values, in which case it was determined from a calculation

Table 5.2.6: Summary of contributions to the $2s^2 2p\ ^2P^o_{3/2}$ – $2s2p^2\ ^4P_{5/2}$ excitation energy (in cm^{-1}) in B I

Excitation energy (PCFI(MR))	28898.69	
Relativistic shift (RS)	43.37	
Fine-structure (FS)	−0.74	
De-constraint (D)	7.05	
Extrapolation (X)	8.10	
Larger MR set (CAS)	2.26	
Finite Mass	−6.20	
Remainder (same as for C II)	6.58	
Total Excitation Energy	28959	± 5
Edlén *et al.* [131]	28866	± 15
Kramida and Ryabstev [132]	28643.1	± 1.8

that included the most corrections in a given calculation. In fact, the sum of the first five entries is the extrapolated value of Table 5.2.4 that includes the de-constraining correction. Our method of computing the correlation energy has accounted for the terms linear in Z of a Z-dependent calculation. Hence, remaining correlation in B I should be similar to that in C II. The uncertainty estimate largely represents the uncertainty of our estimate of the remainder.

Thus our prediction for the $2s^2 2p\ ^2P^o_{3/2}$ – $2s2p^2\ ^4P_{5/2}$ excitation energy is 28959 cm^{-1} ± 5 cm^{-1}, considerably larger than the Edlén *et al.* value of 28866 ± 15 cm^{-1} and the Kramida and Ryabstev value of 28643.1 cm^{-1}.

Chapter 6

The main results and conclusions

1. Energies, transition rates and lifetimes obtained for such elements of isoelectronic sequences: B-like: N III–Zn XXVI; C-like: F IV–Ni XXIII; N-like: F III–Kr XXX; O-like: F II–Kr XXIX. The computed energy levels agree very well with experimental values. The difference between our results and experiment are about few hundred cm^{-1} (less than 0.1%) for many ions of studied isoelectronic sequences.

2. The analysis of theoretical results show that experimental energy for $2s2p^4\ ^2P_{1/2}$ level of Si VIII (N-like) ion must be about 2000 cm^{-1} higher than is given in the NIST database. For the $2s2p^4\ ^2P_{3/2}$ level of Kr XXX (N-like) the experimental value, given in the NIST database, of the energy is more than 2000 cm^{-1} higher as compared to the results obtained in this study.

3. Some possible problems with experimental identification of lines in As XXVI, Se XXVII, and Br XXVIII (O-like ions) have been pointed out. The energy levels for these three spectra, presented in this study, agree much better with semi-empirical values than with results presented in the NIST database.

4. Computed lifetimes for ions of studied isoelectronic sequences agree very well with experiment within experimental uncertainty.

5. Computed transition rates for studied isoelectronic sequences, demonstrated a very good agreement between both (length and velocity) gauges for strong transitions.

6. Structure of energy spectra for W^{24+} was studied in this work for the first time. The energy levels of 4 lowest configurations were presented.

7. E1 transition rates for W^{24+} were computed. The agreement between length and velocity gauges is 2.5 % for strong transitions.

8. In this study a new PCFI aproach, based on biorthogonal orbital method, was proposed with few modifications: i) PCFI; ii) partially deconstrained; iii) DPCFI (fully deconstrained).

9. The expressions of the matrix elements of the Breit-Pauli hamiltonian for the biorthogonal orbital method was modified in the study.

10. Our prediction for the $2s^2 2p\ ^2P^o_{3/2}$–$2s2p^2\ ^4P_{5/2}$ excitation energy is 28959 $cm^{-1} \pm 5\ cm^{-1}$, that is considerably larger than the Edlén *et al.* value of $28866 \pm 15\ cm^{-1}$ and the Kramida and Ryabstev value of $28643.11\ cm^{-1}$.

11. The MCHF method and PCFI, based on biorthogonal orbital method, have been combined to extend the accuracy of variational methods.

12. PCFI method, developed in this study, can be effectively applied for energy calculations. To achieve high accuracy results using PCFI method for specific mass shift parameter and hyperfine structure constants we should use deconstrain option (DPCFI).

Bibliography

[1] H.-K. Chung, P. Jönsson and A. Kramida, *Notes on critical assessment of theoretical calculations of atomic structure and transition probabilities*, Atoms **1**, 14 (2013).

[2] M. Godefroid, P. Jönsson, and C. Froese Fischer, *Atomic structure variational calculations in spectroscopy*, Phys. Scr. **T78**, 33 (1998).

[3] W. R. Johnson, *Atomic structure theory: Lectures on atomic physics*, (Springer-Verlag Berlin Heidelberg, 2007).

[4] I. Lindgren, *Relativistic many-body theory: A new field-theoretical approach*, (Springer-Verlag, Berlin, 2011).

[5] V. A. Dzuba and V. V. Flambaum, *Core-valence correlations for atoms with open shells*, Phys. Rev. A **75**, 052504 (2007).

[6] W. R. Johnson, U. I. Safronova, A. Derevianko, and M. S. Safronova, *Relativistic many-body calculation of energies, lifetimes, hyperfine constants, and polarizabilities in ^7Li*, Phys. Rev. A **77**, 022510 (2008).

[7] M. S. Safronova, M. G. Kozlov, W. R. Johnson, and D. Jiang, *Development of a configuration-interaction plus all-order method for atomic calculations*, Phys. Rev. A **80**, 012516 (2009).

[8] P. Knowles, M. Schütz, and H.-J. Werner, *Ab initio methods for electron correlation in molecules*, In J. Grotendorst, editor, Modern Methods and Algorithms of Quantum Chemistry, Proceedings, volume 3, pages 97–179. John von Neumann Institute for Computing, NIC Series, Jülich, 2000.

[9] R. J. Bartlett, *The coupled-cluster revolution*, Molecular Physics **108**, 2905 (2010).

[10] M. Das, M. Das, R. K. Chaudhuri, and S. Chattopadhyay, *Application of relativistic Fock-space coupled-cluster theory to study Li and Li-like ions in plasma*, Phys. Rev. A **85**, 042506 (2012).

[11] E. A. Hylleraas, *The Schrödinger two-electron atomic problem*, volume 1 of Advances in Quantum Chemistry, pages 1 – 33, Academic Press, 1964.

[12] J. S. Sims and S. A. Hagstrom, *Hylleraas-configuration-interaction study of the $2\,^2S$ ground state of neutral lithium and the first five excited ^2S states*, Phys. Rev. A **80**, 052507 (2009).

[13] J. Komasa, W. Cencek, and J. Rychlewski, *Explicitly correlated Gaussian functions in variational calculations: The ground state of the beryllium atom*, Phys. Rev. A **52**, 4500 (1995).

[14] F. W. King, D. Quicker, and J. Langer, *Compact wave functions for the beryllium isoelectronic series, Li^- to Ne^{6+}: A standard Hylleraas approach*, J. Chem. Phys **134**, 124114 (2011).

[15] B. O. Roos, *The complete active space self-consistent field method and its applications in electronic structure calculations*, In K. P. Lawley, editor, Advances in Chemical Physics; Ab Initio Methods in Quantum Chemistry - II, chapter 69, pages 399–445, John Wiley& Sons, Chichester, England, 1987.

[16] M. J. Vilkas, Y. Ishikawa, and E. Träbert, *Relativistic many-body Møller-Plesset perturbation theory calculations of the energy levels and transition rates in Na-like to P-like Xe ions*, At. Data Nucl. Data Tables **94**, 650 (2008).

[17] Y. Ishikawa, J. A Santana, and E. Träbert, *Relativistic multireference many-body perturbation theory for open-shell ions with multiple valence shell electrons: the transition rates and lifetimes of the excited levels in chlorinelike Fe X*, J. Phys. B: At. Mol. and Opt. Phys. **43**, 074022 (2010).

[18] P.-Å . Malmqvist, *Calculation of transition density matrices by nonunitary orbital transformations*, Int. J. Quantum Chem. **30** 479 (1986).

[19] J. Olsen, M. Godefroid, P. Jönsson, P.-Å. Malmqvist, and C. Froese Fischer, *Transition probability calculations for atoms using non-orthogonal orbitals*, Phys. Rev. E **52**, 4499 (1995).

[20] C. Froese Fischer, T. Brage and P. Jönsson, *Computational atomic structure: An MCHF approach*, (Bristol: Institute of Physics Publishing, 1997).

[21] B. J. McKenzie, I. P. Grant, and P. H. Norrington, *A program to calculate transverse Breit and QED corrections to energy levels in a multiconfiguration Dirac-Fock environment*, Comput. Phys. Commun. **21**, 233 (1980).

[22] I. P. Grant, *Gauge invariance and relativistic radiative transitions*, J. Phys. B **7**, 1458 (1974).

[23] C. Froese Fischer, *Evaluating the accuracy of theoretical transition data*, Phys. Scr. **T134**, 014019 (2009).

[24] C. Froese Fischer, G. Tachiev, G. Gaigalas, and M. Godefroid, *An MCHF atomic-structure package for large-scale calculations*, Comput. Phys. Commun. **176**, 559 (2007).

[25] P. Jönsson, X. He, C. Froese Fischer, and I. P. Grant, *The grasp2K relativistic atomic structure package*, Comput. Phys. Commun. **177**, 597 (2007).

[26] P. Jönsson, G. Gaigalas, J. Bieroń, C. Froese Fischer, and I. P. Grant, *New version: GRASP2K relativistic atomic structure package*, Comput. Phys. Commun. **184**, 2197 (2013).

[27] M. Moshinsky and T. H. Seligman, *Group theory and second quantization for nonorthogonal orbitals*, Ann. Phys. **66**, 311 (1971).

[28] A. P. Jucys and A. J. Savukynas, *Mathematical foundations of the atomic theory*, (Mintis, Vilnius, 1973).

[29] R. Glass, *Reduced matrix elements of tensor operators*, Comput. Phys. Commun. **16**, 11 (1978).

[30] G. V. Merkelis, J. Kaniauskas, and Z.B. Rudzikas, *Formal methods of the stationary perturbation theory for atoms*, Lithuanian Journal of Physics **25** (no.5), 21 (1985).

[31] G. Gaigalas, Z. Rudzikas and Ch. Froese Fischer, *An effcient approach for spin-angular integrations in atomic structure calculations*, J. Phys. B: Atomic, Molecular and Optical Physics **30**, 3747 (1997).

[32] G. Racah, *Theory of complex spectra. I*, Phys. Rev. **61**, 186 (1942).

[33] G. Racah, *Theory of complex spectra. II*, Phys. Rev. **62**, 438 (1942).

[34] G. Racah, *Theory of complex spectra. III*, Phys. Rev. **63**, 367 (1943).

[35] G. Racah, *Theory of complex spectra. IV*, Phys. Rev. **76**, 1352 (1949).

[36] G. Gaigalas, *Integration over spin-angular variables in atomic physics*, Lithuanian Journal of Physics **39**, 79 (1999).

[37] G. Gaigalas, *The library of subroutines for calculation of matrix elements of two-particle operators for many-electron atoms*, Lithuanian Journal of Physics **42**, 73 (2002).

[38] G. Gaigalas and Z. Rudzikas, *Secondly quantized multi-configurational approach for atomic databases*, NIST Special publication **926**, 128 (1998).

[39] R. Glass and A. Hibbert, *Relativistic effects in many electron atoms,* Comput. Phys. Commun. **16**, 19 (1978).

[40] G. Gaigalas, A. Bernotas, Z. Rudzikas, and Ch. Froese Fischer, *Spin–other–orbit operator in the tensorial form of second quantization*, Phys. Scr. **57**, 207 (1998).

[41] G. Gaigalas, S. Fritzsche, and I. P. Grant, *Program to calculate pure angular momentum coefficients in jj-coupling*, Comput. Phys. Commun. **139**, 263 (2001).

[42] M. J. Vilkas, Y. Ishikawa, and E. Träbert, *Relativistic many-body perturbation calculations of boron-like silicon, Si X*, Phys. Scr. **72**, 181 (2005).

[43] V. Jonauskas, P. Bogdanovich, F. P. Keenan, R. Kisielius, M. E. Roord, R. F. Heeter, S. J. Rose, G. J. Ferland, and P. H. Norrington, *Energy levels and transition probabilities for boron-like Fe XXII*, A&A **455**, 1157 (2006).

[44] A. K. Bhatia and G. A. Doschek, *Atomic data and spectral line intensities for C-like Ne V*, At. Data Nucl. Data Tables **55**, 315 (1993).

[45] K. G. Dyall, I. P. Grant, C. T. Johnson, F. A. Parpia, and E. P. Plummer, *GRASP: A general-purpose relativistic atomic structure program*, Comput. Phys. Commun. **55**, 425 (1989).

[46] L. Sturesson, P. Jönsson, and C. Froese Fischer, *JJGEN: A flexible program for generating lists of jj-coupled configuration state functions*, Comput. Phys. Commun. **177**, 539 (2007).

[47] M. Godefroid, J. Olsen, P. Jönsson, and C. Froese Fischer, *Accurate MCHF calculations of oscillator strengths in light atoms: the B II line at 1362 Å*, ApJ. **450**, 473 (1995).

[48] P. Jönsson and J. Bieroń, *Relativistic configuration interaction calculations of energy levels, isotope shifts, hyperfine structures, and transition rates in the $2s^2 2p^2$-$2s2p^3$ transition array for the carbon-like sequence*, J. Phys. B: At. Mol. Phys. **43**, 074023 (2010).

[49] K. T. Cheng, Y.-K. Kim, and J. P. Desclaux, *Electric dipole, quadrupole, and magnetic dipole transition probabilities of ions isoelectronic to the first-row atoms, Li through F*, At. Data Nucl. Data Tables **24**, 111 (1979).

[50] U. I. Safronova, W. R. Johnson, and M. S. Safronova, *Relativistic many-body calculations of energies of n=3 states for the boron isoelectronic sequence, Z=6-30*, At. Data Nucl. Data Tables **69**, 183 (1998).

[51] U. I. Safronova, W. R. Johnson, and A. E. Livingston, *Relativistic many-body calculations of electric-dipole transitions between n=2 states in B-like ions*, Phys. Rev. A **60**, 996 (1999).

[52] C. Froese Fischer and G. Tachiev, *Breit-Pauli energy levels, lifetimes, and transition probabilities for the beryllium-like to neon-like sequences*, At. Data and Nucl. Data Tables **87**, 1 (2004).

[53] G. Tachiev and C. Froese Fischer, *Breit-Pauli energy levels, lifetimes and transition data: boron-like spectra*, J. Phys. B: At. Mol. Opt. Phys. **33**, 2419 (2000).

[54] C. Froese Fischer and G. Tachiev, MCHF/MCDHF Collection, Version 2, Ref. No., Available online at http://physics.nist.gov/mchf. (2012). National Institute of Standards and Technology.

[55] K. Koc, *Ab initio calculation of $1s^2 2l3l' 4l''$ energy levels and E1 transition probabilities for O^{3+}*, J. Phys. B: At. Mol. Opt. Phys. **37**, 3821 (2004).

[56] K. Koc, *Multireference relativistic configuration interaction calculations for $2s^2 2p\ ^2P_{3/2} - ^2P_{1/2}$ M1 and E2 transitions in boron isoelectronic sequence*, J. Phys. B: At. Mol. Opt. Phys. **36**, L93 (2003).

[57] K. Koc, *Relativistic MR RCI calculation of energy levels and transition probabilities of boron isoelectronic sequence*, Phys. Scr. **67**, 491 (2003).

[58] G. Corrégé and A. Hibbert, *Transitions in C II, N III, and O IV*, At. Data and Nucl. Data Tables **86**, 19 (2004).

[59] G. Merkelis, M. J. Vilkas, G. Gaigalas, and R. Kisielius, *MBPT calculation of energy spectra and E1 transition probabilities for boron isoelectronic sequence*, Phys. Scr. **51**, 233 (1995).

[60] P. Bogdanovich, R. Karpuškienė, and O. Rancova, *Influence of the two-electron transitions on the radiative lifetimes of excited levels in the boron isoelectronic sequence*, Phys. Scr. **75**, 669 (2007).

[61] P. Jönsson, J. Li, G. Gaigalas, and C. Dong, *Hyperfine structures, isotope shifts, and transition rates of C II, N III, and O IV from relativistic configuration interaction calculations*, At. Data and Nucl. Data Tables **96**, 271 (2010).

[62] J. Li, P. Jönsson, C. Dong, and G. Gaigalas, *Two-electron–one-photon M1 and E2 transitions between the states of the $2p^3$ and $2s^2 2p$ odd configurations for B-like ions with $18 \leq Z \leq 92$*, J. Phys. B: At. Mol. Opt. Phys. **43**, 035005 (2010).

[63] L. Hao and G. Jiang, *Energy levels, transition rates, and line strengths of B-like ions*, Phys. Rev. A **83**, 012511 (2011).

[64] Yu. Ralchenko, A. E. Kramida, J. Reader, and NIST ASD Team (2012). NIST Atomic Spectra Database (ver. 4.1.0), [Online]. Available: http://physics.nist.gov/asd [2012, January 13]. National Institute of Standards and Technology, Gaithersburg, MD.

[65] P. Bengtsson, L. J. Curtis, M. Henderson, R. E. Irving and S. T. Maniak, *Lifetime measurements in N III using the beam-foil technique and cascade corrections*, Phys. Scr. **52**, 506 (1995).

[66] E. Träbert and P. H. Heckmann, *EUV spectrum and lifetimes of foil-excited phosphorus*, Phys. Scr. **21**, 35 (1980).

[67] B. C. Fawcett, *Calculated wavelengths, oscillator strengths, and energy levels for allowed 2-2 and 2-3 transitions for ions in the C-like isoelectronic sequence between F IV and Ni XXIII*, At. Data Nucl. Data Tables **37**, 367 (1987).

[68] R. D. Cowan, *The theory of atomic structure and spectra*, (Univ. of California Press, 1981).

[69] K. M. Aggarwal, A. Hibbert, and F. P. Keenan, *Oscillator strengths for transitions in O III*, Astrophys. J. Suppl. Ser. **108**, 393 (1997).

[70] K. M. Aggarwal, *Oscillator strengths for transitions in C-like Ne, Mg, Si, and S Ions*, Astrophys. J. Suppl. Ser. **118**, 589 (1998).

[71] K. M. Aggarwal, F. P. Keenan, and A. Z. Msezane, *Oscillator strengths for transitions in C-like Ions between F IV and Ar XIII*, Astrophys. J. Suppl. Ser. **136**, 763 (2001).

[72] H. L. Zhang and D. H. Sampson, *Relativistic distorted-wave collision strengths and oscillator strengths for the Δ n=0 transitions with n=2 in C-like ions with $9 \leq Z \leq 54$*, At. Data Nucl. Data Tables **63**, 275 (1996).

[73] H. L. Zhang and D. H. Sampson, *Relativistic distorted-wave collision strengths and oscillator strengths for all possible n=2-n=3 transitions in C-like ions*, At. Data Nucl. Data Tables **65**, 183 (1997).

[74] U. Feldman, G. A. Doschek, J. T. Mariska, A. K. Bhatia, and H. E. Mason, *Electron densities in the solar corona from density-sensitive line ratios in the N I isoelectronic sequence*, ApJ **226**, 674 (1978).

[75] U. Feldman, *The use of spectral emission lines in the diagnostics of hot solar plasmas*, Phys. Scr. **24**, 681 (1981).

[76] A. K. Bhatia and E. Landi, *Atomic data and spectral line intensities for Si VIII*, At. Data Nucl. Data Tables **85**, 317 (2003).

[77] A. Mohan, E. Landi, and B. N. Dwivedi, *On the extreme-ultraviolet/ultraviolet plasma diagnostics for nitrogen-like ions from spectra obtained by SOHO/SUMER*, ApJ **582**, 1162 (2003).

[78] A. Wouters, J. L. Schwob, S. Suckewer, J. F. Seely, U. Feldman, and J. H. Davé, *Spectra in the 60-45 Å wavelength region of the elements Fe, Ni, Zn, Ge, Se, and Mo injected into the Princeton Large Torus tokamak*, J. Opt. Soc. Am. B **5**, 1520 (1988).

[79] A. K. Bhatia, J. F. Seely, and U. Feldman, *Atomic data and spectral line intensities for the nitrogen isoelectronic sequence (Ar XII through Kr XXX)*, At. Data Nucl. Data Tables **43**, 99 (1989).

[80] V. Kaufman, J. Sugar, and D. Cooper, *N I isoelectronic sequence: observations of* $2s^m2p^n - 2s^{m-1}2p^{n+1}$ *intersystem transitions and improved measurements for CI XI, K XIII, Ca XIV, Sc XV, Ti XVI, and V XVII*, Phys. Scr. **26**, 163 (1982).

[81] B. Edlén, *Comparison of theoretical and experimental level values of the n=2 configurations in the nitrogen isoelectronic sequence*, Phys. Scr. **30**, 135 (1984).

[82] J. Clementson, P. Beiersdorfer, G. V. Brown, M. F. Gu, H. Lundberg, Y. Podpaly, and E. Träbert, *Tungsten spectroscopy at the Livermore electron beam ion trap facility*, Can. J. Phys. **89**, 571 (2011).

[83] E. Träbert, A. G. Calamai, J. D. Gillaspy, G. Gwinner, X. Tordoir, and A. Wolf, *Intercombination and forbidden transition rates in C- and N-like ions (*O^{2+}*,* F^{3+}*, and* S^{9+}*) measured at a heavy-ion storage ring*, Phys. Rev. **62**, 022507 (2000).

[84] E. Träbert, P. H. Heckmann, W. Schlagheck and H. v. Buttlar, *Beam-foil lifetime studies of highly ionized silicon*, Phys. Scr. **21**, 27 (1980).

[85] M. Godefroid and C. Froese Fischer, *MCHF-BP fine-structure splittings and transition rates for the ground configuration in the nitrogen sequence*, J. Phys. B: At. Mol. Phys. **17**, 681 (1984).

[86] S. R. Becker, K. Butler, and C. J. Zeippen, *Improved M1 and E2 transition probabilities for forbidden lines in ions of the nitrogen isoelectronic sequence*, A&A **221**, 375 (1989).

[87] W. Eissner, M. Jones, H. Nussbaumer, *Techniques for the calculation of atomic structures and radiative data including relativistic corrections*, Comput. Phys. Commun. **8**, 270 (1974).

[88] G. Merkelis, M. J. Vilkas, R. Kisielius, G. Gaigalas, and I. Martinson, *Electric dipole transitions in ions of the N I isoelectronic sequence*, Phys. Scr. **56**, 41 (1997).

[89] G. Merkelis, I. Martinson, R. Kisielius and M. J. Vilkas, *Ab initio calculation of electric quadrupole and magnetic dipole transitions in ions of the N I isoelectronic sequence*, Phys. Scr. **59**, 122 (1999).

[90] R. V. Orloski and A. G. Trigueiros, *Weighted oscillator strengths and lifetimes for the Si VIII spectrum*, Journal of Quantitative Spectroscopy and Radiative Transfer **69**, 13 (2001).

[91] M. J. Vilkas and Y. Ishikawa, *Relativistic multireference Möller-Plesset perturbation theory calculations for the term energies and transition probabilities of ions in the nitrogen isoelectronic sequence*, Advances in Quantum Chemistry **39**, 261 (2001).

[92] G. I. Tachiev and C. Froese Fischer, *Breit-Pauli energy levels and transition rates for nitrogen-like and oxygen-like sequences*, A&A **385**, 716 (2002).

[93] S. N. Nahar, *Atomic data from the Iron Project*, A&A **413**, 779 (2004).

[94] V. Jonauskas, P. Bogdanovich, F. P. Keenan, M. E. Foord, R. F. Heeter, S. J. Rose, G. J. Ferland, R. Kisielius, P. A. M. van Hoof, and P. H. Norrington, *Energy levels and transition probabilities for nitrogen-like Fe XX* A&A **433**, 745 (2005).

[95] E. Landi, A. K. Bhatia, *Atomic data and spectral line intensities for Mg VI*, At. Data Nucl. Data Tables **93**, 1 (2007).

[96] X.-L. Wang, S.-H. Chen, X.-Y. Han, J.-M. Li, *Fine-structure splittings of nitrogen isoelectronic sequence: Competitions among spin-orbit interactions, breit interactions and electron correlations*, Chin.Phys.Lett. 25 (2008) 903.

[97] K. L. Baluja and C. J. Zeippen, *M1 and E2 transition probabilities for states within the* $2p^4$ *configuration of the O I isoelectronic sequence*, J. Phys. B: At. Mol. Opt. Phys. **21**, 1455 (1988).

[98] A. K. Bhatia, R. J. Thomas, and E. Landi, *Atomic data and spectral line intensities for Ne III* At. Data Nucl. Data Tables **83**, 113 (2003).

[99] E. Landi and A. K. Bhatia, *Atomic data and spectral line intensities for Ca XIII*, A&A **444**, 305 (2005).

[100] E. Landi, *Radiative transition probabilities in the O-like sequence*, A&A **434**, 365 (2005).

[101] N. C. Deb, A. Hibbert, *Breit-Pauli energy levels belonging to* $2p^4$, $2s^2p^5$, $2p^6$, $2p^3 3l$ *configurations and all E1 transitions among these levels in Mg V*, At. Data Nucl. Data Tables **93**, 585 (2007).

[102] G. Gaigalas, J. Kaniauskas, R. Kisielius, G. Merkelis and M. J. Vilkas, *Second-order MBPT results for the oxygen isoelectronic sequence*, Phys. Scr. **49**, 135 (1994).

[103] M. J. Vilkas, G. Merkelis, R. Kisielius, G. Gaigalas, A. Bernotas and Z. Rudzikas, *Ab initio calculation of E1 transitions in the oxygen isoelectronic sequence*, Phys. Scr. **49**, 592 (1994).

[104] C. Froese Fischer, X. He, and P. Jönsson, *The* $2p^4\ ^3P_{1,2}$–$2p^3 3s\ ^5S^o_2$ *and* $2p^4\ ^3P_{1,2}$–$2s2p^5\ ^3P^o_2$ *transitions in the oxygen isoelectronic sequence*, Eur. Phys. J. D. **4**, 285 (1998).

[105] M. J. Vilkas, K. Koc, Y. Ishikawa, *Relativistic multireference Möller-Plesset perturbation theory based on multiconfigurational Dirac-Fock reference functions*, Chemical Physics Letters **296**, 68 (1998).

[106] M. J. Vilkas, Y. Ishikawa, K. Koc, *Relativistic multireference many-body perturbation theory for quasidegenerate systems: Energy levels of ions of the oxygen isoelectronic sequence*, Phys. Rev. A **60**, 2808 (1999).

[107] U. I. Safronova and A. S. Shlyaptseva, *Inner-shell excitation energies and autoionization rates for C-, N-, O-, and F-like ions with Z = 654*, Phys. Scr. **60**, 36 (1999).

[108] P. Bogdanovich, R. Karpuškienė, A. Momkauskaitė, and A. Udris, *Theoretical calculation of wavelengths and oscillator strengths of 2p-3l transitions in Mg V, Si VII, and S IX ions*, Lithuanian Journal of Physics, **39**, 11 (1999).

[109] P. Bogdanovich, R. Karpuškienė, and I. Martinson, *Theoretical lifetimes for all states of five Cl X configurations*, Nucl. Instr. and Meth. in Phys. Res. B: Beam Interactions with Materials and Atoms, **205**, 70 (2005).

[110] P. Bogdanovich and R. Karpuškienė, *Ab initio oscillator strengths and transition probabilities in oxygen-like Cr XVII*, At. Data Nucl. Data Tables **94**, 623 (2008).

[111] V. Jonauskas, F. P. Keenan, M. E. Foord, R. F. Heeter, S. J. Rose, G. J. Ferland, R. Kisielius, P. A. M. van Hoof, and P. H. Norrington, *Dirac-Fock energy levels and transition probabilities for oxygen-like Fe XIX*, A&A **424**, 363 (2004).

[112] E. Landi and M. F. Gu, *Atomic data for high-energy configurations in Fe XVII-XXIII*, ApJ **640**, 1171 (2006).

[113] S. N. Nahar, *Oscillator strengths and transition probabilities for allowed and forbidden transitions in Fe XIX*, At. Data Nucl. Data Tables **97**, 403 (2011).

[114] M. F. Gu, *Indirect X-ray line-formation processes in iron L-shell ions*, ApJ **582**, 1241 (2003).

[115] R. L. Kelly, *Atomic and ionic spectrum lines below 2000 Angstroms: hydrogen through krypton*, J. Phys. Chem. Ref. Data **16**, Suppl. 1, 1, (1987).

[116] B. Edlén, *Comparison of theoretical and experimental level values of the n=2 complex in ions isoelectronic with Li, Be, O and F*, Phys. Scr. **28**, 51 (1983).

[117] A. G. Calamai, G. Gwinner, X. Tordoir, E. Träbert, and A. Wolf, *Electric quadrupole and magnetic dipole transition probabilities within the ground configuration of F^+*, Phys. Rev. A **61**, 062508 (2000).

[118] A. Daw, W. H. Parkinson, P. L. Smith, and A. G. Calamai, *Transition probabilities for the 1815 and 3344 Åforbidden lines of Ne III*, Astrophys. J. Lett. **533**, 179 (2000).

[119] E. Träbert, A. Wolf, X. Tordoir, E. H. Pinnington, E. J. Knystautas, G. Gwinner, A. G. Calamai, and R. L. Brooks, *Lifetime of metastable Ne^{2+} ions measured at a heavy-ion storage ring*, Can. J. Phys. **79**, 145 (2001).

[120] E. Träbert, A. Wolf, E. H. Pinnington, J. Linkemann, E. J. Knystautas, A. Curtis, N. Bhattacharya, and H. G. Berry, *Heavy-ion storage ring measurement of forbidden transition rates between ground-configuration levels in Si^{6+} and Si^{8+} ions*, Can. J. Phys. **76**, 899 (1998).

[121] E. Träbert, M. Grieser, J. Hoffmann, C. Krantz, R. Repnow, and A. Wolf, *Heavy-ion storage-ring-lifetime measurement of metastable levels in the C-, N-, and O-like ions of Si, P, and S*, Phys. Rev. A **85**, 042508 (2012).

[122] L. Yang, D. A. Church, S. Tu, and J. Jin, *Measured lifetimes of selected metastable levels of Ar^{q+} ions (q=2, 3, 9, and 10) stored in an electrostatic ion trap*, Phys. Rev. A **50**, 177 (1994).

[123] M. Loulergue, H. E. Mason, H. Nussbaumer, and P. J. Storey, *Fe XIX transitions within the N=2 complex*, A&A **150**, 246 (1985).

[124] Z. Rudzikas, *Theoretical Atomic Spectroscopy*, (Cambridge university press, (1997), second edition 2007).

[125] Z. B. Rudzikas and J. V. Čiplys, *Structure and spectra of complex atoms and ions*, Physica Scripta **T26**, 21 (1989).

[126] T. Žalandauskas, G. Gaigalas, and Z. Rudzikas, *Optimization of coupling scheme in $2p^N 3l$ (N=2, 3, 4 and l= s, p, d) isoelectronic sequences*, Nuclear Instruments and Methods in Physics Research B **235**, 149 (2005).

[127] G. Gaigalas, Z. Rudzikas, and C. Froese Fischer, *An efficient approach for spin - angular integrations in atomic structure calculations*, J. Phys. B: At. Mol. Opt. Phys. **30**, 3747 (1997).

[128] S. Verdebout, P. Jönsson, G. Gaigalas, M. Godefroid, and C. Froese Fischer, *Exploring biorthonormal transformations of pair-correlation functions in atomic structure variational calculations*, J. Phys. B: At. Mol. Phys. **43**, 074017 (2010).

[129] Z.-C. Yan and G. W. F. Drake, *Theoretical lithium $2^2S - 2^2P$ and $2^2P - 3^2D$ oscillator strengths*, Phys. Rev. A **52**, R4316 (1995).

[130] Z.-C. Yan, D. K. McKenzie, and G. W. F. Drake, *Variational calculations of the Fermi contact term for the 2^2S, 2^2P, and 3^2S states of Li and the 2^2S state of Be^+*, Phys. Rev. A **54**, 1322 (1996).

[131] B. Edlén, H. Palenius, K. Bockasten, R. Hallin, and J. Bromander, *Spin-forbidden resonance multiplets in light elements*, Sol. Phys. **9**, 432 (1969).

[132] A. E. Kramida and A. N. Ryabtsev, *A critical compilation of energy levels and spectral lines of neutral boron*, Phys. Scr. **76**, 544 (2007)

[133] G. Tachiev and C. Froese Fischer, *Breit-Pauli energy levels, lifetimes and transition data: boron-like spectra*, J. Phys. B: At. Mol. Opt. Phys. **33**, 2419 (2000).

[134] E. R. Davidson, S. A. Hagstrom, S. J. Chakravorty, V. Umar, and C. Froese Fischer, *Ground-state correlation energies for two- to ten-electron atomic ions*, Phys. Rev. A **44**, 7071 (1991)

[135] M. Godefroid, C. Froese Fischer, and P. Jönsson, *Non-relativistic variational calculations of atomic properties in Li-like ions: Li I to O VI*, J. Phys. B: At. Mol. Opt. Phys. **34**, 1079 (2001).

[136] P. R. Young, U. Feldman, and A. Lobel, *Forbidden and intercombination lines of RR TelescopII: wavelength measurements and energy levels*, Astrophys. J. Suppl. Ser. **196**, 23 (2011).